Visualization of metastatic melanoma cells by fluorescence microscopy and MRI using a novel glycogen nanoprobe

Synnøve Nymark Aasen

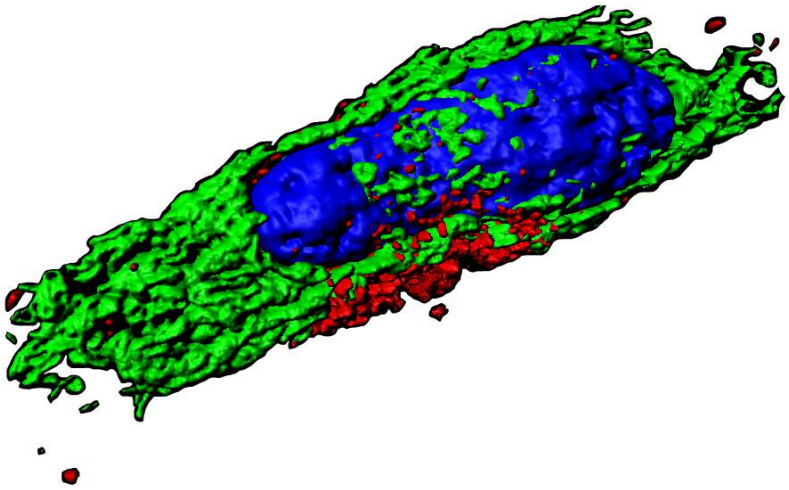

This thesis is submitted in partial fulfilment of the requirements for the degree of Master in Medical Biology – Biomedical Image Sciences

Department of Biomedicine

University of Bergen

June 2014

Acknowledgements

First of all, I am very grateful to Professor Frits Thorsen at the Translational Cancer Research Group, for excellent supervision during the work of this thesis and for introducing me to a very exciting field of research. Thank you for all your time and help in your busy days, I would recommend any new Master student to chose you as a supervisor. Also, thanks to my former co-supervisor Kai Ove Skaftnesmo, for sharing some of your outstanding lab skills with me.

I also give my greatest gratitude to Aneta Pospisilova and the others at the Institute of Macromolecular Chemistry in Prague for providing us with the glycogen nanoprobe.

Great thanks go to Tilo Eichler for all your support and interest in this project during the last year and for useful input on confocal experiments.

Thanks to Endy Spriet and Hege Dale for all your help on the microscopes and Anne Karin Nyhaug for sectioning and staining of tumor samples. Thanks to Hrvoje Miletic for interpreting our histology samples. Thanks to Ingrid, Tove and Halala for your help in the lab.

Great thanks to all hard-working PhD students and postdocs on the sixth floor, who lucky for me, has been around on late evenings or weekends and helped me with occasional challenges: Eskil, Hilde-Elise and Lina. And thanks to Jonathan for clearing up some confusing statistical numbers for me.

I would also like to thank my visually challenged family for all your support and for being test subjects on whether or not all the figures in the thesis were possible to see. Great thanks to Steffen for all your support, help and encouragement. Finally, thanks to Ronja, Line, Ragnhild and Elah for being excellent reading room buddies!

Synnøve, May 2014

Abstract

The incidence of malignant melanoma has increased steadily during the last decades. Large portions of individuals with this particular skin cancer develop multiple brain metastases, which is associated with a particular poor prognosis, and thus new therapeutic approaches are needed. Increased attention has been given lately in literature to the establishment of functional nano-scaled materials for applications in combined cancer therapy and diagnostics, a field termed «theranostics» or «theragnosis» (*thera*py + diag*nostics*).

Recently, a collaborator at the Institute of Macromolecular Chemistry (Academy of Sciences, Prague) developed a multimodal nanoprobe, consisting of a backbone of glycogen. Two different contrast agents were encompassed in this, namely Dyomics-615-NHS ester, a fluorescent marker and Gd-DOTA, a well-known magnetic resonance imaging contrast agent. The nanoprobe can also be loaded with positron emission tomography tracers and therapeutic substances, and targeting may be achieved by loading the probe with antibodies. The nanoprobe has a great potential for being a theranostic probe, as the backbone consists of glycogen, which is regarded nontoxic to human cells. Further, magnetic resonance imaging and positron emission tomography may be used to evaluate drug uptake and treatment effects.

Since this nanoprobe is completely new, it has not been tested previosly on human cell lines *in vitro* and *in vivo*. The main aim of the current Master thesis was thus to perform toxicity and viability studies *in vitro*, to determine the usefulness of the nanoprobe. The usability of the nanoprobe was evaluated on three different metastatic melanoma cell lines *in vitro*. Fluorescence microscopy and high throughput imaging revealed a high cell labeling efficacy with an optimal uptake period at 24 hours incubation time. Reduced cell viability was not found after labeling with the nanoprobe. *In vitro* magnetic resonance imaging studies of labeled cells casted in agar phantoms revealed that the nanoprobe also can be used as a contrast agent by this modality. The preliminary *in vivo* data indicated that tumor contrast uptake could be achieved in a subcutaneous tumor model. The promising results reported in this thesis may indicate that this nanoprobe can be used also for other cancer cell lines. Potentially, the nanoprobe can offer further benefits over established contrast agents used in magnetic resonance imaging, as pharmaceuticals attached to the probe can be traced simultaneously as the progression of disease and treatment are monitored.

Abbreviations

Abbreviation	Full name
BBB	Blood-brain barrier
BLI	Bioluminescent imaging
BP	Bandpass
CA	Contrast agent
CCD	Charged-couple device
CNS	Central nervous system
CT	Computer tomography
DLS	Dynamic light scattering
DMEM	Dulbeccos Modified Eagles Medium
DMSO	Dimethyl sulphoxide
DNA	Deoxyribonucleic acid
DOTA	1,4,7,10-tetraazacyclododecane-1,4,7,10-tetraacetic acid
Dyo-615	Dyomics-615-NHS ester
ECM	Extracellular matrix
EMT	Epithelial-to-mesenchymal transition
EPR	Enhanced permeation and retention
FA	Flip angle
FACS	Fluorescence activated cell sorting
FCS	Fetal calf serum
FDA	Food and Drug Administration
FOV	Field of view
G1P	Glucose-1-phosphate
G6P	Glucose-6-phosphate
Gd	Gadolinium
GFP	Green fluorescent protein
HTI	High throughput imaging
HTS	High content screening
ISA	Image sequence analysis
LD_{50}	Lethal dose 50 %

Abbreviation	Full name
LP	Longpass
LUT	Look-up table
Melanoma	Malignant melanoma of the skin
MMP	Matrix metalloproteinases
MRI	Magnetic resonance imaging
msec/ms	Millisecond
NaCl	Sodium chloride
NC	Negative control
NEX	Number of Excitations
Nod/scid	Nonobese-diabetic/severe combined immunodeficient mouse
NS	Not significant
PBS	Dulbeccos phosphate-buffered saline
PET	Positron emission tomography
PFA	Paraformaldehyde
PMT	Photomultiplier tube
R_H	Dynamic radius
Resazurin	7-Hydroxy-3H-phenoxazin-3-one 10-oxide
RF	Radiofrequency
ROI	Region of interest
RPM	Rotations per minute
SD	Standard deviation
T	Tesla
T_1	Relaxation time of longitudinal magnetisation
T_2	Relaxation time of transverse magnetisation
TE	Echo time
TR	Repetition time
TSP-1	Thrombospondin-1
VEGF	Vascular endothelial growth factor
wt%	Weight percent

List of figures

Table of contents

1. Introduction

1.1 Malignant melanoma: Incidence and biological aspects

Malignant melanoma of the skin, hereafter referred to as melanoma, is an aggressive type of cancer, which originates from melanocytes located in the epidermis of the skin (1). During the past 50 years, a steadily increasing occurance has been detected globally and in 2008, the annual incidence was estimated to be 200 000 individuals worldwide (2). A considerable portion of these cases is manifested in fair-skinned populations in developed countries where USA, Australia and the Nordic countries present with the highest rates. In developed countries, melanoma is the sixth most frequent type of cancer, and 46 000 deaths are registered as a consequence of the disease every year (3). Although melanoma only accounts for 5 % of all skin cancers, it is responsible for 80 % of skin cancer related deaths (4, 5). The growing occurrence has been attributed to more frequent exposure to sun radiation, however this environmental risk factor is accompanied by skin phenotype and family history of certain inherited mutations (6).

In general it often appears that the incidence of cancer occurs more frequently with increasing age (7). In Norway, individuals within the age group 50–70+ are most often afflicted (8). This is in orchestra with the statement above, conceivably due to an accumulation of somatic mutations and immune system regression with growing age (9, 10). In the case of melanoma however, the incidence in Norway unveils a peak at the age 15–49 for women and 25–49 for men (8). This suggests that a younger population is affected, which is in disagreement with the traditional idea of cancer mainly influencing the elderly.

As in general carcinogenesis, melanoma is also presumed to develope in a stepwise pattern from a focal origin such as a precursor neoplasm. It has been suggested that the onset of malignancy is dependent on multiple mutations in several cell signaling pathways (Figure 1.1) (11). In melanoma development, it is often distinguished between radial and vertical growth phases as illustrated in Figure 1.1 (12). Radial growth is characterized by an *in situ* lesion with melanocytic growth occuring by cell proliferation horizontally in the basal layer of the skin (4). At this stage the cells have not transformed, and therefore do not have any cancer cell-related properties such as angiogenesis or ability to metastasize. Provided enough time, this phase may be substituted by vertical growth (Figure 1.1). During this juncture, the

neoplasm grows downward and penetrates dermis and a nodular or palpable lesion on the skin often occurs (4, 13). Accompanied with the vertical growth phase is an accumulation of multiple mutations (14), which challenges the prognostic power of genetic expression (15). The prognosis of melanoma is therefore dependent on clinical manifestation at the primary site, histological findings as well as the number, size and placement of secondary tumors (15).

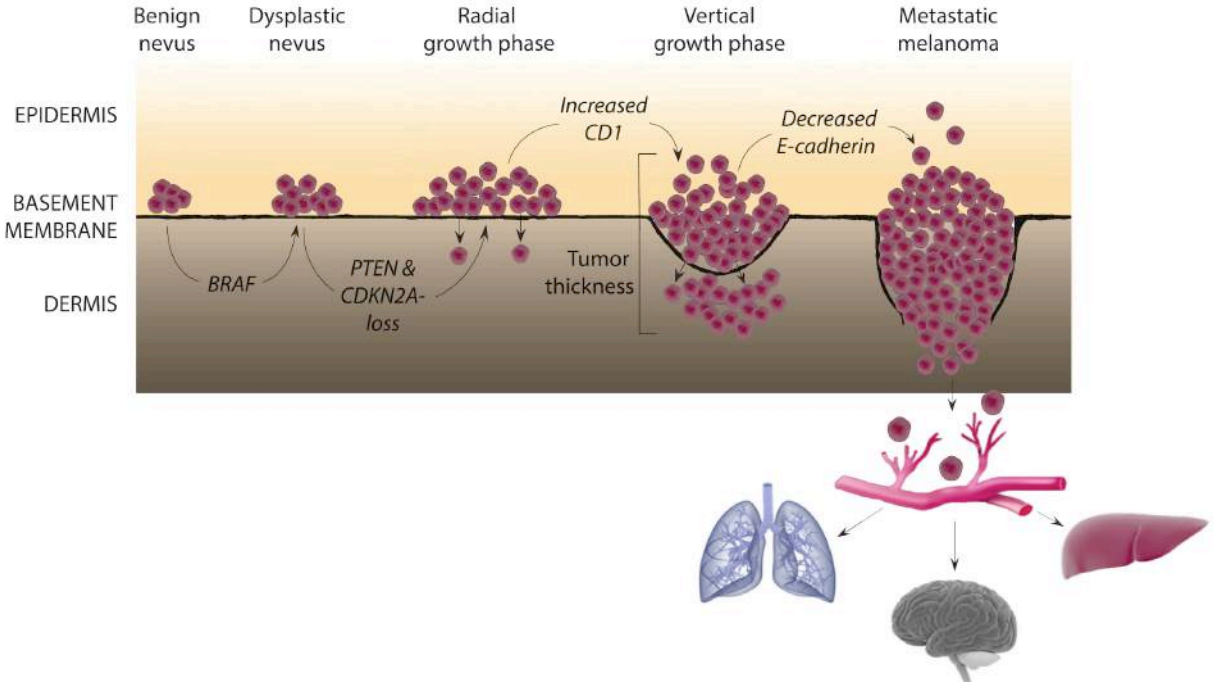

Figure 1.1: Melanoma progression. Subsequent of melanocytic proliferation, atypical nevus may form in the epidermis layer. This is an abnormal growth of melanocytes, which can result in a pre-malignant lesion. Melanocyte proliferation will then take place horizontally in the skin, characterized as a radial growth phase, where tumor growth rarely occurs deep into dermis. After several possible cellular mutations, a vertical growth phase may take place, in which malignant melanoma cells invade the basement membrane while proliferating vertically. Subsequently, the melanoma cells can acquire further malignant properties enabling them to spread to distant organs such as lungs, brain and liver. Figure created with items from Somersault (16) and American Association for Cancer Research (17).

Tumor thickness, as illustrated in Figure 1.1, was introduced by Alexander Breslow in 1970 and measures the depth of the melanoma lesion in mm (18). In this system, the expected prognosis is reduced with increasing tumor thickness or depth. This is still used in the clinic today, as it is a reliable predictor of tumor invasiveness, metastatic potential and prognosis (4).

1.2 The metastatic process with emphasis on brain metastases

Metastasis can be described as a series of linked sequential steps in which cancer cells disseminate from their origin to a secondary site. A very frequently reported outcome for melanoma patients (75 %) is the formation of multiple brain metastasis (19-21), displaying

the highest tendency of any cancer to disseminate to the central nervous system (22). With a median survival estimated to a few months, secondary tumors to the brain consequently correlate with a low prognosis (19, 23).

As melanoma neoplasms grow beyond ~1 mm^3, they depend on vascularization to receive oxygen and nutrients (24). At this point, hypoxia often occurs as a result of tumor growth, which triggers angiogenesis. Vascularization can be obtained by several mechanisms of which vascular co-option through pre-existing blood vessels and angiogenic sprouting from pre-existing vessels are two examples (25-28). The initiation of tumor vascularization is a balance between proangiogenic and inhibiting factors, where vascular endothelial growth factor (VEGF) and thrombospondin-1 (TSP-1), respectively, are representative examples. Further vessel development depends on yet other proangiogenic factors, such as angiopoietin and Tie-R (29). In addition to further tumor growth, angiogenesis also provides access to the vasculature which subsequently allows tumor cell dissemination (24). Prior to local invasion into dermis, migrating melanoma cells often acquire an epithelial-mesenchymal transition (EMT)-like phenotype characterised by altered cell-cell interaction properties (1). Normally, E-cadherins mediate melanocyte contact with five to eight surrounding keratinocytes. However, during melanoma progression this contact is lost by downregulation of E-cadherin (1, 30). In addition to this detachment of melanoma cells from its surroundings, altered cellular adhesive features are obtained, which enable them to attach to new sites (30). Local invasion includes the employment of different proteases to degrade extracellular matrix (ECM), such as matrix metalloproteinases (MMPs). Several components are involved in the simultaneous movement of melanoma cells, such as interacting integrins, components of the actin cytoskeleton and focal adhesion complexes (31). During degradation of ECM, cell motility and cell morphology is constantly altered (32). Melanoma cells often intravasate to the lymphatic or hematogenous circulatory system (33), in which they are subjected to immunological and mechanical barriers during transport to distant organs.

Although melanoma cell dissemination can occur through lymphatogenous and hematogenous paths, the cells have to gain access to the blood circulatory system in order to extravasate into brain tissue. Once a subset of a migrating cell population reach a secondary organ, such as the brain, they may be trapped in for instance vascular branch points due to size restrictions or reduced flow in capillaries (Figure 1.2 A) (28).

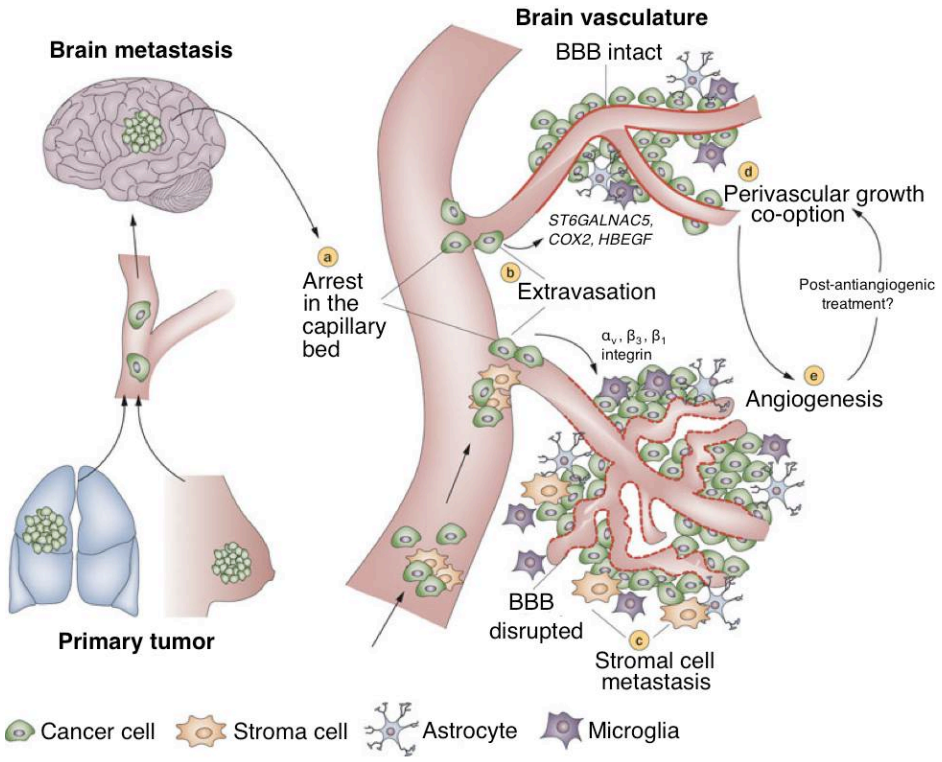

Figure 1.2: Formation of brain metastases. Once a subset of the primary tumor manages to approach the brain, they are caught in vascular beds (a). Following extravasation (b), secondary tumors may grow further by preexisting blood vessels (c) or by employing angiogenesis (d). Adapted from Eichler, A.F. et al., 2011 (28), modified with larger fonts.

Subsequent passage across the blood-brain barrier (BBB) depends on cellular adhesion to local endothelium before extravasation into the brain parenchyma is possible (33). The BBB is situated at the level of cerebral capillaries, and separates circulating blood from cerebrospinal fluid surrounding neuronal tissue. Movement of solutes and cellular elements are thus restricted from entering the brain parenchyma by this protective impediment. Despite this, certain types of cancer cells, such as from melanoma, manage to extravasate and subsequently create secondary tumors within the brain (34). After attaching to endothelial cells in the brain microvasculature, a remodeling of the capillary network occurs, and the tumor cells transmigrate through BBB and thus extravasate into the brain parenchyma (24, 35). The exact mechanism for this is not known (36), but it has been suggested that the BBB might have a sustaining function in the formation of brain metastases (34). Previously, it has been reported that migrating melanoma cells located in capillaries often express the Ig family cell adhesion molecule *L1CAM* (37), mainly expressed in neuronal and cancerous tissue (38). Additionally, the sialyltransferase *ST6GalNaC5* (39) has also been identified as a mediator of tumor cell transmigration through BBB (37, 40). Other proteins targeting specific organs might also be expressed by the tumor cells (36). Additionally, activation of integrins has been

proposed to influence endothelial tumor cell adhesion (28). Thus, extravasation of migrating melanoma cells through blood vessels may occur. Subsequent extravasation, secondary macrotumors may begin to form (Figure 1.2 B), termed colonization (24).

Colonization in the new milieu is dependent on paracrine or autocrine signaling of the tumor cells to stimulate further proliferation, in which the «seed and soil theory» postulated by Paget is relevant. This theory proposes that the occurrence of brain metastases is not random, but instead certain tumor cells, «the seed», have an attraction or affinity to the new environment, «the soil». If the host tissue allows for tumor growth and cell proliferation continues, angiogenesis is induced by the same mechanisms as for primary site tumors (Figures 1.2 D and E) and the lesion grows further (41). For brain metastasis, secondary tumors either employ angiogenesis or grow along pre-existing blood vessels by co-option (28). In addition to secondary tumors to the central nervous system (CNS), other common sites secondary to melanoma are subcutaneous tissue, lymph nodes, lungs, liver and bones (42).

1.3 Model systems to study cancer

In order to study cancer cell dissemination and solid tumor growth, suitable model systems are necessary. Such systems should represent tumor growth seen in patients as close as possible. Several *in vitro* and *in vivo* culture systems have been developed in the past, and a few of these are described in this chapter.

1.3.1 *In vitro* cell culture

The current understanding of cancer has partly been derived from tumor cell lines developed from primary and secondary tumors (43). Such cultured cells have been extensively used within the field of biomedicine for a number of reasons: Essential cancer cell features such as proliferation and an abnormal karyotype are maintained, and the method can easily be implemented in different research layouts with varying purposes (22). By growing cells in a monolayer in cultured conditions, a controlled growth environment is provided, which enables regular observation of the sample (Figure 1.3 left). Despite these advantages, and the fact that the technique is easy to use and repeat, certain limitations of this *in vitro* assay should be emphasised. Because cell behaviour to a great extent depends on interactions within a 3D environment, this aspect is compromised when growing cells in monolayer on flat dishes (44-47). Still, cancer research is excessively reliant on monolayer or 2D cell culture (43, 48),

and it can be considered a good starting point for cell based research as well as standardized methods for drug screening. To address some of the limitations associated with monolayer culture such as altered protein expression (47), cell proliferation (45) and metabolism (44, 46), 3D cell cultures or spheroid models can be implemented in experiment designs. These have been described as superior compared to monolayer cultures (43). Instead of adhesion and migration occuring in only 2D, cells cultured in 3D layouts have the ability to adhere, proliferate and migrate in an additional dimension (Figure 1.3 right) (48).

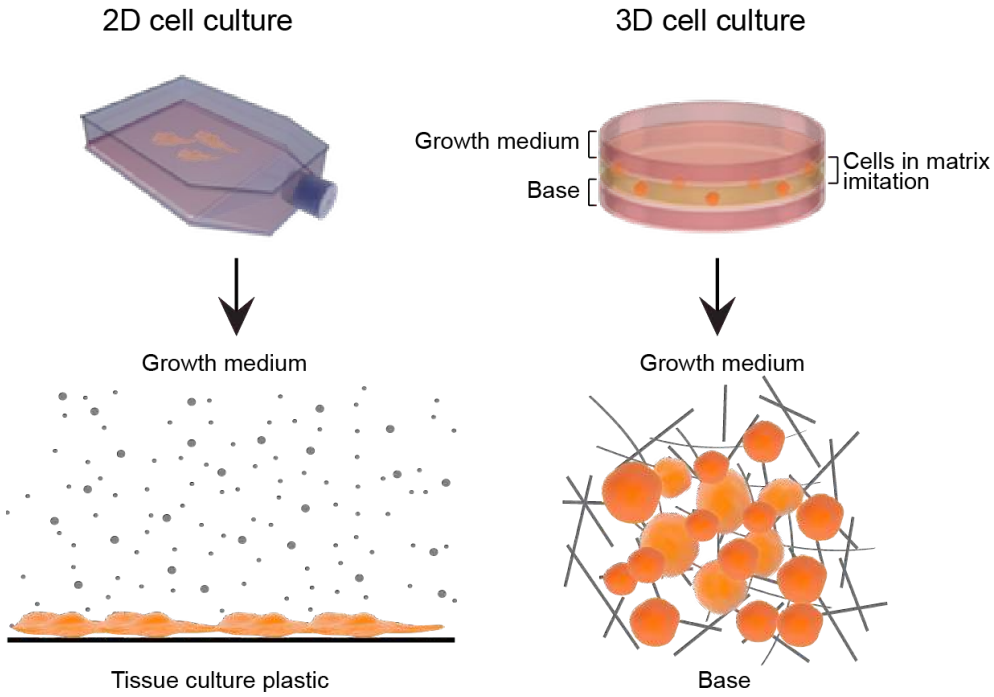

Figure 1.3: Cell culture illustration. The left column illustrates how cellular growth in media occurs flat on a plastic dish, constricted to the x-y plane of a culture flask. The right column shows how cells seeded in for instance a two-layered agar layout are provided a 3D environment, which results in altered cell shape and growth pattern. Figure created with symbols from Somersault (16).

Various 3D cell culture experiment designs exist (43), where the additional dimension is accompanied by an improved modeling of the real *in vivo* situation. It has been shown that cell signaling, cellular stiffness and shape differs between the two layouts, and it can be stated that 3D cultures offer more physiological conditions, more similar to an *in vivo* situation, for cell lines compared to monolayer cultures. For continous cancer cell lines, this implies that true tumor cell characteristics are mimicked for cellular spheroids with impaired access to oxygen and nutrients centrally, surrounded by adhered aggregates or clusters of additional cells (49). Several issues related to *how* the additional dimension in 3D cultures provide altered conditions, still remain to be properly explained. Still, it is known that

microenvironmental factors promote cell function, and these are modulated by different means in 2D and 3D cultures (48).

1.3.2 Animal tumor models

To study tumor development and predict therapeutic efficiency of novel pharmaceuticals in cancer research, several pre-clinical animal tumor models have been developed, mostly based on the use of small rodents. To grow tumors in mice for instance, extractions of tumor material such as continous cell lines are regularly injected into animals, either subcutaneously, into the organ of which the cells originated from (orthotopic) or into the blood stream (ectopic). Also, genetically engineered mice holding a particular genotype are often used as model systems (50). The discovery of T- and B-cell-deficient mice, nonobese diabetic severe combined immunodeficiency (nod/scid) (51), permits the transplantation of established *in vitro* cell lines or tumor biopsy material into immuno-deficient model mice, to efficiently reassemble solid tumors after a lagtime of a few weeks (50). Although such preclinical models mimic a real situation more closely than *in vitro* cell cultures (52), there are several factors that retain such techniques from being ideal. For instance, tumors often form more rapidly in animal models with a smaller latency period compared to a cancer patient in a clinical setting. Also, the use of nod/scid mice in itself can be a disadvantage, as tumor development after xenograft in immunedeficient organisms differs from cancer patients (52). Nevertheless, the combined knowledge of studies on animal tumor models have added increased understanding of the cancerous progression, given that the most suitable model system for the specific scientific problem is chosen (24).

1.4 *In vitro* cell viability assays

A variety of methods to assess viability of cultured cells and cytotoxity of certain compounds of interest exist (53). These should be sensitive, rapid and inexpensive (53-55), and are often subdivided into four groups depending on the method of measurement: Colonogenic, radioactive, colorometric and fluorometric (53, 56). Resazurin, which has been used since the 1950s (55), has the advantage of being non-toxic (57), and it can be used both as a colorometric and fluorometric assay, of which it has been indicated that the latter gives more precise measurements (55). Resazurin holds a major change in perceived hue when used as an indicator on oxidation–reduction in human cells. Resazurin is intrinsically a weak fluorescent of purple color, but is reduced to the highly fluorescent pink resorufin. This transformation only occurs in metabolically active and thus viable and proliferating cells. Dead cells do not

have the same ability to perform this activity, and on this basis, the colored product correlates with viable cells in culture. It is therefore possible to use this assay to predict cytotoxicity of any compound of interest by reading off the results at wavelength 530-560 nm excitation and 590 nm emission (54, 55, 57, 58).

1.5 Preclinical cancer imaging

The field of image sciences has proven to be incredibly valuable in cancer research, and has together with clinical observations contributed greatly to our comprehension of the development and treatment of malignancies (59-61). A large amount of preclinical imaging techniques to visualize cancer cells and tumors exist, ranging from *in vitro* methods at cellular levels, to sub-millimeter *in vivo* approaches. Each modality has its benefits and disadvantages, and a single technique alone does not posess all the required capabilities for complete detection. Therefore, the possibility of dual or multimodal signal reading from one common probe enables visualization of samples with more than one modality (62, 63). In the following, the imaging modalities used in this project will be discussed briefly.

1.5.1 Light and fluorescence microscopy

Varying microscopic approaches are widely used in cell biological research. The non-invasive nature of light microscopy together with the feasibility to introduce fluorochromes makes it the technique of choice for live-cell imaging (64). Light microscopes can be used to determine cell viability as well as depicting pathological cell conditions.

In all its simplicity, light microscopes consist of a light source, magnifying lenses and often also an image acquisition unit (64). In addition, mercury lamps are often incorporated in widefield microscopes for excitation of fluorochromes and subsequent induction of emission. A bandpassfilter located between the light source and the cell sample efficiently restricts the range of excitation light. Because the emitted light has a longer wavelength than the excited, an emission filter (bandpass or longpass) is necessary between the detector and the cell sample. The excitation light is thus blocked, and the final image is prevented from distortions. The images are often detected by a charged couple device (CCD), and displayed on a computer screen (64).

Fluorescence is a molecular characteristic of certain substances where light of a given

wavelength is absorbed, which transfers electrons to an orbital of higher energy, introducing an excited state. As electrons fall back into original energy states, excess energy is released by means of light at a longer wavelength and thus lower energy (Figure 1.4). The emitted light can be detected with the aid of optical filters in customized microscopes (64).

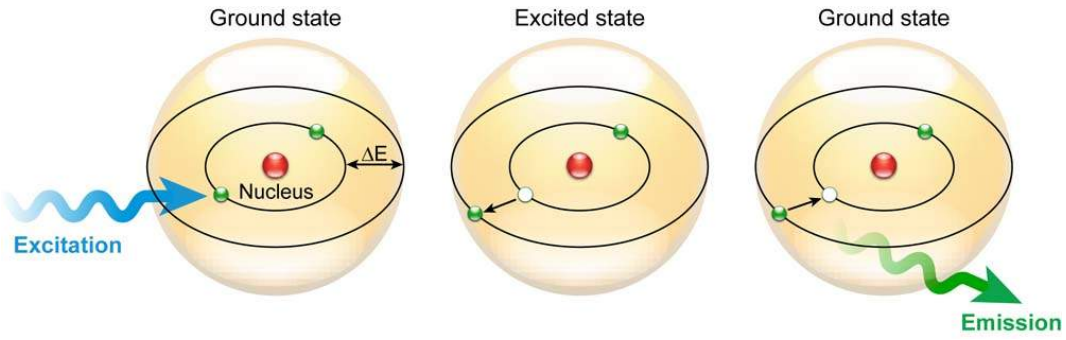

Figure 1.4: The principle of fluorescence. When light of a given wavelength is absorbed, an atomic electron is transferred to an orbit of higher energy. After the lifetime of the fluorescence agent, this excited state is substituted by the original state as the electron falls back into its previous energy level. As this happens, excess energy is given off by means of a light photon at a different wavelength. Adapted form Ishikawa-Ankerhold, 2012 (64).

Fundamentally, fluorescent agents or fluorochromes are used as potent contrast enhancers in microscopic imaging (64). Multi-fluorescent imaging is considered a significant tool to analyse cellular and biological events, which is further amplified by the expanding range of available fluorochromes (65). As emitted fluorescent light can be amplified to the microscopy detector, cellular structures can be visualized more easily than without fluorochromes. This relies on the effectivity of the system to pass light to either a CCD or photomultiplier tube (PMT), and simultaneously block excited light. Examples of fluorescent substances are green fluorescence protein (GFP), a reporter molecule that is intrinsically fluorescent, and Hoechst 33342, often used to analyse DNA.

Visualization of fluorescent agents can also be enabled with confocal microscopy. Laser scanning techniques are commonly used, in which a laser beam is focused onto the sample and scanning in the x-y plane occurs line-by-line. What sets confocal techniques aside from conventional fluorescence microscopes is a pinhole used to eliminate scattered light. Ultimately this provides high-resolution micrographs with the entire sample in focus (66).

1.5.2 High throughput imaging (HTI)

HTI, sometimes also referred to as high content screening (HTS), was introduced in the late

1990s, and established a potential for live-cell microscopy of large quantities of cell samples (e.g. in 96-well plates), implemented in automatic image acquisition sequences (65). HTI has the capability to acquire data on multi-parametric samples, such as several fluorescent markers, and also enables repeated image acquisitions over a defined time-span. Large-scale drug-screening research is often based on high throughput approaches, thereby improving the productivity dramatically (67). HTI techniques can thus acquire data on large numbers of samples in a less time-consuming process compared to conventional fluorescence microscopic methods, without losing valuable information at the level of single cells.

1.5.3 Magnetic Resonance Imaging (MRI)

MRI can be regarded a superior imaging modality, due to excellent soft tissue contrast. It is also considered a risk-free procedure for the patient, as MRI does not use ionizing radiation.

The essential source of the MRI signal is based on the hydrogen nuclei or protons, which are abundantly present in tissue. Each proton is positively charged, and is also constantly spinning around its own axis. According to physics theory, a moving electrical charge of this kind generates a current, which in turn creates a magnetic field. Stated in other words, each proton generates its own magnetic field, and can be considered a small magnet. This magnetic field is also referred to as a magnetic moment. The orientations of all these protons in tissue are usually randomly directed, creating a net magnetic moment, which is zero. However, when an object such as a patient or animal is placed within the main magnet of an MRI system, the protons will align either parallell or anti-parallell with the main magnet field, B_0, inside the scanner. The majority of protons will align parallell, as this requires the least energy. The difference between the number of protons aligned parallell and the number of protons aligned anti-parallell is usually very small. However, this difference increases with elevated magnetic field strength, and is the source for generating a signal which in the end is reconstructed to become part of the MR image (68).

When the protons are put inside the strong magnetic field B_0, they will move in a way called precession. This movement is similar to what is seen in a spinning top, as the protons wobble but do not fall over during spinning. Thus the sum magnetic field from these protons, which is now regarded a single vector M_0, rotates around B_0 with a precession frequency determined by the magnetic field, termed the Larmor frequency (69).

In order to detect a signal from the precessing protons, the protons need to be manipulated. Radiofrequency (RF) pulses are then switched on and off, with the purpose of forcing the protons to fall out of the alignment with B_0. The disturbance occurs when energy with the same frequency as the precession frequency is applied to the tissue, a phenomenon called resonance. The net magnetic moment will as a consequence move out of alignment with B_0, and the protons are moved into the transverse plane, or the x-y plane (Figure 1.5 B) (68).

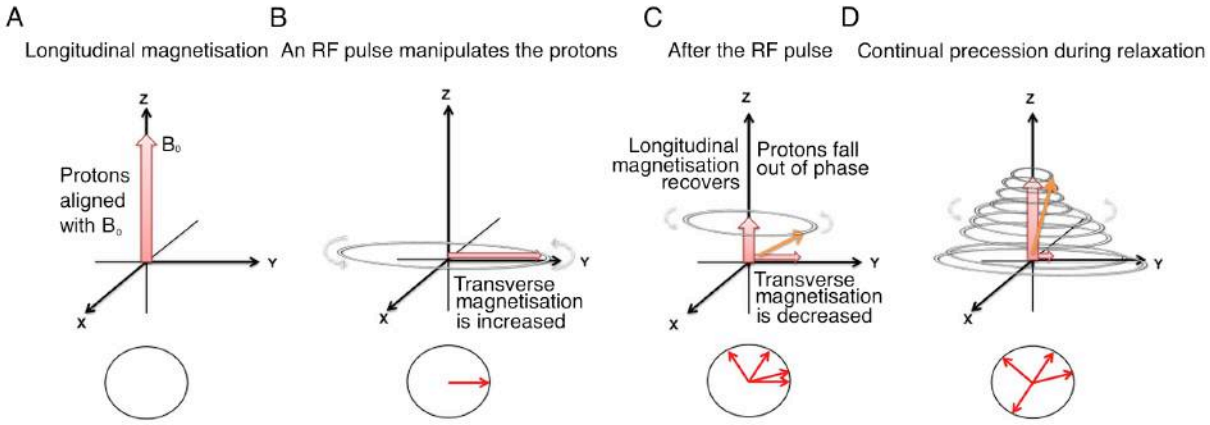

Figure 1.5: Relaxation after an RF pulse. The hydrogen protons are initially aligned with the main magnetic field, B_0 (A). After the introduction of an RF pulse which manipulates the protons, the longitudinal magnetism will decrease and transverse magnetism (in x-y plane) is increased (B). When the RF puse is switched off, the protons will start to fall out of phase, and as the transverse magnetisation decreases, longitudinal magnetisation increases (C). The precession continues throughout recovery of longitudinal magnetisation (D). Regain of longitudinal magnetism is called T_1 recovery, and loss of transverse magnetism is called T_2 decay. Adapted from Currie, 2013 (68), modified with figure text.

The use of an RF pulse will move some of the protons from the parallell to the anti-parallell state, resulting in a reduction in overall longitudinal magnetism. Also the RF pulse makes the protons move in the same direction, or phase. The result is that a magnetisation occurs in the transverse plane, moves at the Larmor frequency and thus generates an alternating voltage that can be detected in antennas or RF coils placed within close proximity. This results in the formation of an MRI signal. When the RF pulse is deactivated (Figures 1.5 C and D), the protons will start to move out of phase and lose energy, termed «proton relaxation». This takes place in two ways; transverse magnetism is referred to as T_2 or spin-spin relaxation, and longitudinal magnetism returns to the initial situation called T_1 or spin-lattice relaxation. The speed at which T_1 relaxation occurs is dependent on the properties of the surroundings. Therefore, different tissues or arrangements with hydrogen to other substances will produce different T_1 relaxation times. The time constant T_1 is the time it takes until longitudinal magnetism is regained to 63 % of its final value. T_2 relaxation describes loss of in-phase

protons due to inhomogeneities within the local tissue and within B_0. The time constant T_2 describes the time it takes before transverse magnetism is reduced to 37 % (68).

Varying combinations of RF pulses and imaging parameters constitute different imaging sequences, broadly categorized into spin-echo and gradient-echo sequences. In this way, tissues can be weighted by different means, dependent on the purpose of the image sequence. The images are constructed with the aid of gradients in three dimensions: The slice-selection gradient, G_{SS}, is applied in a short bandwidth of frequencies matching the larmor frequency. A slice within the biological object is then excited, the thickness of which is dependent on the steepness of the gradient. For spatial signal encoding, phase (G_{PH}) and frequency (G_{FR}) gradients are employed. The application of these enables the detection of signal in phase and frequency for location within the selected slice. This is repeated in several steps for the entire slice, with the G_{PH} altered for each step. Thus, multiple signal echoes are acquired and stored in a raw data matrix termed K space, before this is Fourier-transformed to the spatial content of MR images (68). The image reconstruction process for MRI signal is a complex matter (70), of which a further description is beyond the scope of this thesis.

1.5.4 MRI phantoms

MRI phantoms can be used to evaluate the application of novel contrast agents (71). Favourable features of such phantoms include comparable relaxation times to biological tissue, temporal stability, low costs and that they are easily available and simple to handle (71). A range of different materials for this purpose exists, and water, agar and agarose, which is a purified form of agar, remain the most common (71, 72). Phantoms mimicking biological relaxation times can according to Yoshimura (2003) be obtained using concentrations of agar and agarose at 1.5-3 % and 0.8-4 %, respectively (73). Based on acquired image series of such phantoms, it is possible to calculate the MRI signal through signal equations, as well as T_1 and T_2 relaxation constants (71).

1.6 Nanomedicine

Normally, single image modalities such as for instance MRI or computer tomography (CT) with Gd or iodine-based contrast agents, respectively, are used to diagnose and study tumor progression. Nanomedicine, on the other hand, is the application of materials of nano-scale size, either for therapeutic or diagnostic purposes (74-76). Depending on the particular

nanomaterial used, several advantages may be obtained compared to conventional approaches in diagnostics and therapy: Multiple contrast agents or optical tracers can be integrated into one common probe, thereby featuring detectable agents during their biological paths when injected into model animals or patients. Also, by modifying such nanoprobes with for instance antibodies, they can be targeted to specific locations. It is also possible to use nanoprobes for enhanced therapeutic delivery. Therapeutic agents such as doxorubicin might be packed onto nanoprobes constructed to respond to certain stimuli, exemplified by acidic pH, to release drugs (74, 77). Thus, drug-delivery may be optimized, while undesirable effects of the treatment, such as toxicity, are minimized (63, 64).

Recently, the term «theranostics» or «theragnosis» has been implemented to describe the combination of therapy and diagnostics using common nanomaterials, thereby introducing a new dimension in cancer research (62, 63, 74, 77). Combining signal detection by means of biomedical imaging with localized drug delivery is unique for nanomaterials (62). Varying substances are used to construct such probes, ranging from organic to non-organic materials (62, 74). Targeted nanomaterials are modified with surface peptides or antibodies specific for the target-cell, whereas passive nanomaterials are constructed so that their size does not contradict the enhanced permeation and retention (EPR) effect, which is often the targeting mechanism for passive nanomaterials (74). EPR is the result of the irregular vascularization and morphology of tumors, and thus abnormal transport dynamics. This often results in molecules of nano-scale size accumulation inside tumors (78).

1.6.1 Novel glycogen nanoprobe

In 2012, Filippov and colleagues at the Institute for Experimental Medicine in Prague developed a nanoprobe that consists of biodegradable glycogen (63). The present glycogen material originates from oyster and the nanoprobe is through dynamic light scattering (DLS) experiments found to have a dynamic radius (R_H) of 54.4 nm. After initial construction of the probe, it was subsequently modified to encompass 3.19 weight percent (wt%) of the MRI contrast agent Gadolinium-DOTA (Gd) in addition to 0.33 wt% of the fluorescent marker Dyomics-615-NHS ester (Dyo-615). Gd is a paramagnetic contrast agent and the governing type used in clinical MRI (79). It has seven unpaired electrons, and because electrons have a great charge-to-mass ratio, Gd produces a major magnetic moment. It is a T_1 agent, which means it produces bright areas of contrast enhancement in T_1 image sequences. Gd is useful in

diagnostics of brain tumors, as the blood-brain barrier (BBB) often is compromised in the tumors and T_1 agent thus leaks into the lesions (80). To reduce the toxic nature of Gd, it is chelated to different ligands, such as for instance DOTA used in our glycogen nanoprobe. Gd will affect the T_1 value according to Figure 1.6 A.

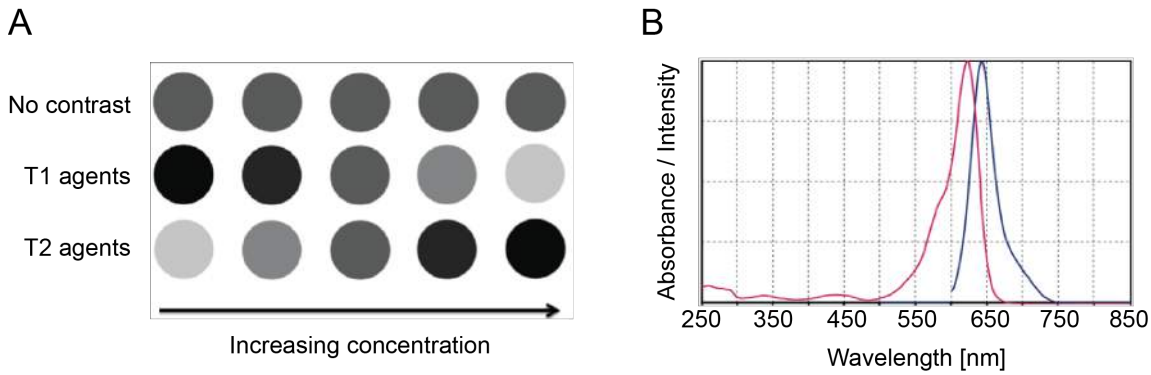

Figure 1.6: Illustrations of the contrast agents encompassed in the glycogen nanoprobe. A: MR image contrast expected to be found with the glycogen nanoprobe (T_1 agent). Adapted from Chen, 2013 (77). Modified with ”no contrast” and larger fonts. B: Emission and excitation spectrum of Dyo-615. Adapted from Czerney, 2011 (81). Modified with larger fonts.

The second segment of the probe, Dyo-615 is an indirect fluorochrome that emits light at wavelength 643 nm when excited by light with a shorter wavelength, and therefore higher energy, in accordance with Stokes shift (Figure 1.6 B). Thus, the probe can be used in a multimodal setting due to compatibility between MRI and fluorescence microscopy imaging.

Furthermore, it is possible to attach therapeutic agents to the nanoprobe, which gives it potential as a theranostic unit. Although biodegradable, glycogen is not affected by amylases in the bloodstream, and the probe can thus be used as a passive nanomaterial via intravenous injection routes.

2. Aims

Melanoma can be regarded a global and contemporaneously a national source of difficulty among relatively young individuals often awaiting a poor prognosis. It can thus be argued that further attention should be paid to the investigation of tumor spread and therapeutic efficiency. For this purpose the Translational Cancer Research Group at Department of Biomedicine, University of Bergen have developed animal models where cell lines derived from human melanoma metastases are injected into immunodeficient mice. This system closely mimics the dissemination observed in patients. Appropriate contrast agents are essential in this context, either to visualize single cancer cells or tumors within model animals. The superior goal of this Master thesis will thus be to describe applications of the theranostic glycogen nanoprobe presented in Chapter 1.6.1 for use in a metastatic melanoma model, which has not been done previously. Several imaging modalities will be used for this purpose, such as fluorescent light microscopy, high throughput imaging and MRI. If successful, this nanoprobe can offer additional advantages over established contrast agents in MRI, as it is possible to use it in a theranostic setting. Thus, by tracing the glycogen nanoprobe within a model animal or patient by MRI, it is possible to visualize where therapeutic agents attached to the probe are localized and also to monitor the progression of therapy.

Four subaims have been defined within the work with this thesis:

1. Use microscopy to demonstrate cellular internalization of the considered nanoprobe and subsequently conclude with an optimal dose for *in vitro* use
2. Investigate cell viability after labeling cells with the nanoprobe, and study nanoprobe clearance from intracellular sites
3. Verify the selected nanoprobe dose by scanning MRI phantoms with prelabeled cells to demonstrate reduced T_1 relaxation times
4. If time permits, test the nanoprobe on immunodeficient mice with tumors as part of a pilot *in vivo* experiment with nanoprobe doses matching Gd agents commonly used in a clinical setting

3. Materials and methods

3.1 General cell culture work

Three different metastatic melanoma cell lines were used in this project: Melmet 1 pGF1 originates from a subcutaneous tissue extraction of a 36 year old female. Melmet 5 pGF1 is derived from a lymph node metastasis in a female at 56 years of age (82) and H1_DL2 is derived from a secondary tumor in the brain of a 38 year old female (52). All three cell lines were transduced with the genes for green fluorescent protein (GFP), whereas H1_DL2 also was transduced with the Luciferase Firefly gene. For confocal imaging as described in Chapter 3.2.4, H1 cells without GFP and Luciferase were used (52). Solutions and disposables frequently used for cell culture are listed in Table 1.

Table 1: Equipment used for cell culture

NAME	SUPPLIER
ALT DMEM:	
450 mL Dulbeccos Modified Eagles Medium	Sigma-Aldrich Inc., MO, USA
50 mL Heat inactivated fetal calf serum (FCS)	Fischer Scientific, MA, USA
10 mL L-Glutamine, 200 nM	BioWhittaker, Verviers, Belgium
10 mL Penicillin/Streptomycin (PEN-STREP), 100 µL/mL	BioWhittaker
16 mL Non essential amino acids 100X	BioWhittaker
0,1 mL Plasmocin 25 mg/mL	Invivogen, CA, USA
Dulbeccos phosphate-buffered saline (PBS)	Sigma-Aldrich Inc.
Trypsin EDTA, 0.25 %	BioWhittaker
Freezing solution 1:	
9 mL ALT DMEM + 1 mL FCS	
Freezing solution 2:	
8 mL 1xPBS + 2 mL 100 % dimethyl sulphoxide (DMSO)	Sigma-Aldrich Inc.
Disposable pipettes: *5, 10 and 25 mL*	Sigma-Aldrich Inc.

The cell lines were cultured in monolayer with ALT DMEM growth medium and kept in an incubator at 5 % CO_2 and 100 % humidity at 37° C. During experiment periods, the cells were regularly trypsinated and subcultured when almost confluent: After removing the old growth medium, the cells were washed with 0.03 mL/cm^2 PBS followed by trypsination with 0.03 mL/cm^2 trypsin for approximately three minutes. Equal amounts of ALT DMEM were then added to inhibit further trypsin effects. For subculturing, approximately a third of the suspension was transferred to new culture flasks with blue filtered caps (25, 75 or 175 cm^2, Nunc AS, Roskilde, Denmark) containing a total cell suspension/growth medium volume at 0.2 mL/cm^2. For storage over longer periods, the cells were cryopreserved and kept in liquid nitrogen at -196° C: After trypsination, 0.03 mL/cm^2 ALT DMEM was added and the solution was resuspended before transferred to a 15 mL tube (Sigma-Aldrich Inc.). The cells were then

centrifuged at 900 rpm for four minutes. The supernatant was removed, and freezing solution 1+2 described in Table 1 were added and the cell pellet resuspended. The cell solution was evenly divided between several 1 mL cryotubes (Thermo Scientific Inc., MA, USA). The tubes were kept at -80° C before they were placed in the nitrogen tank after 24 hours. For cell thawing, the cryotubes were retrieved from the nitrogen tank, spun down, the freezing solution was removed and the cells were placed in 25 cm^2 culture flasks with 10 mL fresh growth medium. All work with cultured cells was done in sterile conditions, in a laminar flow cabinet bench.

3.2 *In vitro* imaging experiments

Despite the seeming multimodal advantage of the nanoprobe, it had not been tested previously on cancer cell lines. Different methods were thus developed for cell labeling with the nanoprobe prior to varying imaging experiments with microscopy and MRI. For all *in vitro* experiments, the glycogen nanoprobe was mixed 1:1 with autoclaved water (milliQ) to yield a stock solution of 1 mg/mL. All imaging experiments were performed using equipment at the Molecular Imaging Center (MIC), Department of Biomedicine, University of Bergen.

3.2.1 Pilot project: Cellular internalization of the nanoprobe

The Melmet 1 pGF1, Melmet 5 pGF1 and H1_DL2 cells were seeded in duplicate six-well plates (Nunc AS), each well with 10^5 cells in 2 mL ALT DMEM. The cell numbers were determined using a Countess Automated Cell Counter (Invitrogen, Paisley, UK), according to the manufacturers instructions. For each cell line, the cell suspension was diluted and distributed into each well of the six-well plate, and thereafter placed in a CO_2 incubator. The next day the cells were labeled with the nanoprobe at concentrations 5, 10, 20, 50 or 100 μg/mL. Cells in the remaining well in the six-well plate were not labeled and thus used as negative control (NC). After six hours of labeling in the CO_2 incubator, the labeling solution was removed, and all wells washed with 2 mL preheated ALT DMEM. The cells were then fixed by adding 2 mL 4 % paraformaldehyde (PFA, Thermo Scientific Inc.) in PBS to each well. The PFA was removed after 20 minutes, and replaced by 2 mL PBS. The same experimental setup as described above was used for the second plate after an incubation time with the nanoprobe for 24 hours.

The six-well plates were then examined using a Nikon TE2000 inverted microscope (Nikon

Instruments Inc., NY, USA). A consistent study design was provided using the same objective magnification (20X), constant halogen illumination and the same setting on the correction collar (1.6) throughout the experiment. Observation of fluorescence signal from Dyo-615 was enabled through $emission_{MAX}$ at 638 nm. The following exposure parameters were then used for the optical agents depicted: Fluorescence: Exposure time 2 000 ms and gain 1.7. Bright filter: Exposure time 2 ms and gain 1.2.

The micrographs acquired during the pilot project were processed using Photoshop CS5 (Adobe Systems Inc., CA, USA). To provide a realistic rendering of the images, the two layers were separated using NIS Elements Viewer (Nikon Instruments Inc.), which is the original software on the microscope. One image from each sample well was processed and presented in a collage created in Adobe Illustrator (Adobe Systems Inc.). Further, a method modified from Miller to study cellular fluorescence intensity was used (83). The fluorescence signal of four cells from four representative micrographs obtained in the pilot project were measured in Photoshop CS5 one by one. The bright field and fluorescence layers were opened in the software simultaneously. However, the lasso tool was used on the former layer alone to mark the region of interest, before the fluorescence layer was made visible in the same window. The histogram intensity value ranging from 0-255 for 8-bit images was then noted from the histogram overview. Cell morphology was also studied during image processing.

Further we investigated whether cellular internalization of the nanoprobe occurred for *all* or a subset of cells in each sample. The images acquired during the pilot project were therefore investigated cell-by-cell, to detect fluorescence signal. Binary images were then created to demonstrate the findings. Appropriate threshold values were sequentially found for the brightfield and fluorescence layers in Matlab (The MathWorks Inc., MA, USA) for micrographs of each cell line captured of samples labeled with 5 μg/mL incubated for six hours. The Matlab command `im2bw` was used to find usable threshold values. Further, noise was removed from fluorescence micrographs of Melmet 1 pGF1 using the command `bwareaopen`. The resulting binary layers were then superimposed in Photoshop.

3.2.2 HTI experiments: Determination of suitable nanoprobe doses

All three cell lines were grown in 175 cm^2 culture flasks until ~80 % confluence. The cells were trypsinated and counted as previously described. For each cell line, 100 μL cell solution

was distributed into each well of a 96-well plate (Nunc AS), at the following concentrations: 10^3 or $2{\cdot}10^3$ cells per well for the Melmet 1 pGF1 and Melmet 5 pGF1 cell lines, and $2{\cdot}10^3$ or $4{\cdot}10^3$ cells per well for H1_DL2 cells. The plates were incubated for 24 hours. The glycogen nanoprobe was diluted in ALT DMEM to the concentrations shown in Table 2 and preheated before the growth medium in each well was replaced with labeling solution. The incubation times were 2, 4, 6 or 24 hours.

Table 2: Overview of the 96-well plate layout used for the HTI experiments. Glycogen nanoprobe concentrations are presented in [µg/mL] and the different cell populations are indicated in the lower row. The column to the left, T (h), illustrates incubation time of the respective row with glycogen nanoprobe in hours prior to imaging. Abbreviations: NC: negative control, T: time, h: hours.

	1	2	3	4	5	6	7	8	9	10	11	12	T (h)
A	PBS	PBS	PBS	PBS	PBS	PBS	PBS	PBS	PBS	PBS	PBS	PBS	
B	PBS	100	200	300	400	NC	NC	100	200	300	400	PBS	2
C	PBS	100	200	300	400	NC	NC	100	200	300	400	PBS	4
D	PBS	100	200	300	400	NC	NC	100	200	300	400	PBS	4
E	PBS	100	200	300	400	NC	NC	100	200	300	400	PBS	6
F	PBS	100	200	300	400	NC	NC	100	200	300	400	PBS	6
G	PBS	100	200	300	400	NC	NC	100	200	300	400	PBS	24
H	PBS	PBS	PBS	PBS	PBS	PBS	PBS	PBS	PBS	PBS	PBS	PBS	
	10^3 or $2{\cdot}10^3$ cells per well						$2{\cdot}10^3$ or $4{\cdot}10^3$ cells per well						

Before starting the HTI experiments, the labeling solution was removed, and each well was washed with preheated (37° C) ALT DMEM. Cellular nuclei were labeled by adding 100 µL preheated Hoechst 33342 (10 mg/mL, Thermo Scientific Inc.) diluted 1:5000 in PBS, into each well. The cell samples contained three different fluorescent agents; GFP, Hoechst and Dyo-615. The imaging acquisition was thus adjusted to capture these channels. The 96-well plates were examined one by one using the filters and exposure parameters listed in Table 3.

Table 3: Filters and exposure parameters used during image acquisition. (Abbreviations: GFP: Green fluorescent protein, Dyo-615: Dyomics-615-NHS ester, LP: Long pass.)

	GFP	**Hoechst**	**Dyo-615**
Excitation (lamp)	488/510 (A)	360/410 (A)	560/655 (B)
Emission filter	515 LP	435 LP	645/675
Exposure time (s)	0,04	0,025	0,06
Gain	0	0	10

The image acquisition sequence on BD Pathway 855 (BD Biosciences, CA, USA) was then activated, and the utilized sections of the 96 plates including four stiched images and three channels per well was finished automatically approximately 45 minutes later. For each cell

line, 720 images were acquired in total from the BD Pathway system. To extract information from these numerous images, a pipeline in CellProfiler (Whitehead Institute for Biomedical Research, MA, USA) was created to automatically interpret the data. After creating an overview image with all wells, mean cellular fluorescence intensity was measured in the following way: The pixel values in all images were scaled from zero to one, by dividing all the pixels in the red image channel by the maximum possible intensity value. Further, all intensity measurements were computed from the aggregate of all the pixels of interest using these scaled values. The mean value presented in the chapter of results is therefore the average intensity value of all pixels in the red image channel.

3.2.3 *In vitro* MRI: Verification of nanoprobe doses from HTI experiments

Prior to *in vitro* MRI scanning, the three cell lines were embedded in 2 % Difco Agar Noble (BD Biosciences) in 2 mL Eppendorf tubes (Eppendorf AG, Hamburg, Germany). For each cell line, two sets of phantoms were created: One set contained cells prelabeled in monolayer with the nanoprobe, using the doses used for the HTI experiments. The second set contained unlabeled cells.

$2.2 \cdot 10^6$ cells were seeded into 175 cm^2 culture flasks, and incubated for 24 hours. Each flask was then labeled with 200 μg/mL glycogen nanoprobe in 20 mL ALT DMEM, and incubated for another 24 hours.

2.0 g Difco Agar Noble was mixed with milliQ in a glass bottle to a total volume of 100 mL (2 % solution), and heated in a microwave oven until boiling. The agar was then transferred to a preheated waterbath (50° C). Meanwhile, six different cell concentrations were prepared for each cell line, labeled and unlabeled cells, as listed in Table 4.

The cell solutions were kept in 15 mL tubes in the CO_2 incubator for ten minutes together with empty eppendorf tubes and disposable pipette tips. The tubes with cell suspension were then retrieved from the incubator one at a time, and carefully resuspended before 1 mL agar solution and 1 mL cell solution sequentially was added to an eppendorf tube. Immediately after, this mix was carefully resuspended to disperse the cells evenly, without introducing air pockets into the tubes. The tubes were then placed directly on ice for approximately ten minutes to allow the mix to congeal, before refrigerated prior to MRI scans.

Table 4: Overview of the MRI phantoms with varying cell concentrations. Each row in this table correspond with *two* eppendorf tubes with agar-casted cells per cell line; one tube containing labeled cells, and one tube containing unlabeled cells. The latter group was used as NCs for the associated test tubes.

Cells in total per eppendorf tube	Cell concentration
$6 \cdot 10^6$	3 000 cells/µL
$3 \cdot 10^6$	1 500 cells/µL
$1{,}5 \cdot 10^6$	750 cells/µL
$0{,}5 \cdot 10^6$	250 cells/µL
$0{,}1 \cdot 10^6$	50 cells/µL
$0{,}05 \cdot 10^6$	25 cells/µL

Five additional tubes were included as control phantoms: One with 2 % stock agar solution (I), one with 1:1 2 % agar and ALT DMEM (II), one with 1:1 glycogen nanoprobe stock solution with 2 % agar (III), one with 1:1 water and 2 % agar (IV), and one containing only water (V).

The phantoms were examined five at a time, using a 7 T small animal MRI scanner (Bruker Biospin MRI GmbH, Ettlingen, Germany). These were fixed inside a 40 mm quadrature volume coil and adjusted to align with the isocenter of the bore. An overview scan (TriPilot) was first completed, which provided an overview in sagittal, coronal and axial planes, to verify placement of the eppendorf tubes in the center of the magnet. This was followed by a turbo spin echo scan (TurboRARE_T2), which provided axial slices through the sample (TR: 4000 msec, TE: 48 msec, FOV: 2.0 cm, Matrix: 256x256, Slice thickness: 1 mm, Number of slices: 15, Number of Excitations (NEX): 4 and Flip Angle (FA): 180°, scan time: 4 minutes). After visually inspecting the image series to decide on the superior image with respect to homogeneity of the scanned material, this image was chosen for further investigations by means of T_1 and T_2 mapping (TR: 5000, 3000, 1500, 800, 400 and 200 msec TE: 11, 33, 55, 77 and 99 msec, FOV: 3.5 cm, Matrix: 256x256, Slice thickness: 1 mm, Number of slices: 1, NEX: 1, FA: 180°, scan time: 17 minutes). A region of interest (ROI) was defined around each phantom within the selected axial slice using image sequence analysis (ISA), each approximately covering 75 % of each tube.

3.2.4 Confocal imaging: Intracellular location of the nanoprobe

$1.5 \cdot 10^5$ H1 cells were distributed into a 14 mm glass bottom in a 35 mm microwell dish (MatTek Corporation, MA, USA) and kept in CO_2 incubator until cellular attachment to the coverglass had occured. The growth medium was then replaced by 1.5 mL glycogen nanoprobe in ALT DMEM at a concentration 200 µg/mL. The next day, the cells were stained

with preheated 150 nM MitoTracker® Green FM (Invitrogen) and incubated for 30 minutes. After removing the staining solution, 1.5 mL preheated Hoechst 33342 diluted 1:5000 in PBS was added to each well. After 20 minutes, the Hoechst solution was removed and replaced by preheated ALT DMEM in all wells. The live cells were then examined using Leica TCS SP5 (Leica Microsystems, Wetzlar, Germany) with a 63X 1.4 oil lens and laser powers: Hoehcst 33342 39 % 405 nm, Dyo-615 31 % 633 nm and MitoTracker 40 % 488 nm.

3.2.5 Monolayer wound healing assay: Cellular migration

A wound-healing assay was carried out to observe cell migration while exposed to the glycogen nanoprobe. A silicone culture insert (Ibidi GmbH, Martinsried, Germany) was inserted in each well in a 15 µ-slide 4 well chamber (Ibidi GmbH) so that they aligned with one another. A cell concentration at $4 \cdot 10^5$/mL was prepared for Melmet 1 pGF1 cells and 70 µL of this cell solution was added to each bilateral gap of the culture insert. The plate was then incubated for 24 hours. The next day, the culture insert was carefully pulled away using sterile tweezers, to reveal a 500 µm (±50 µm) wound in the bottom of the cell monolayer dish. All chambers were then washed with preheated ALT DMEM. The test chambers were filled with 500 µL glycogen nanoprobe in growth medium corresponding to 200 µg/mL, and NC chambers filled with 500 µL ALT DMEM. Immediately after, cell migration into the wound was studied by time-lapse microscopy for 20 hours, using a Nikon TE2000 inverted microscope equipped with an incubator holding 37 ^{0}C, 100 % humidity and 5 % CO_2. Several wound edge locations were selected for focus in x, y and z directions before the experiment was initiated. Micrographs of each well were captured every 15 minutes.

All micrographs captured of labeled and unlabeled cells at every second hour until confluency were then quantified using FIJI (84). An erosion morphology filter was first added to the micrographs, before edges were found and the entire image sharpened. Black and white threshold was then applied, before the edges were detected again, and the look-up table (LUT) was inverted. By using the analysis function it was possible to outline the edges of the created mask and measure the wound size.

3.2.6 Duration of cellular fluorescence: Nanoprobe clearance

We then studied how long the cells kept their fluorescence after being stained and simultaneously monitored cell proliferation of labeled and unlabeled cells. All three cell lines

were thus studied in two separated layouts: The Melmet 1 pGF1, Melmet 5 pGF1 and H1_DL2 cells were seeded into two wells each per six-well plate at a concentration of $1 \cdot 10^5$ cells/2 mL ALT DMEM. Five six-well plates were prepared in this manner. 24 hours later, cells were labeled with 200 μg/mL glycogen nanoprobe, whereas unlabeled cells were used as negative controls. The next day, the contrast agent added the day before was removed and exchanged with 2 mL preheated ALT DMEM in each well. Cellular fluorescence intensity was then captured using Nikon TE2000 at 0, 24, 48, 72 and 96 hours after removal of the nanoprobe. The same exposure parameters as described for the pilot project were used (Chapter 3.2.1). Cellular fluorescence intensity was measured as described in the pilot project.

The same layout of six-well plates was used for monitoring cell proliferation under constant exposure to 200 μg/mL glycogen nanoprobe. All cells were then trypsinated and live and dead cells were counted for labeled and unlabeled cells at the same time points as for imaging experiments. The proliferation assay was done in triplicate.

3.2.7 Soft agar assay: Investigation of the cells in a 3D environment

A two-layered soft agar assay was used to study the cells in a 3D environment. The base agar layer was prepared first: Difco Agar Noble (BD Biosciences) was mixed with milliQ water to a 2.4 % solution and microwaved until dissolved. Further it was placed in a preheated waterbath at 50° C together with 30 mL ALT DMEM. When the temperature had stabilized at 50° C (after approximately 10 minutes), agar and medium were mixed together 1:3 and 1.5 mL of the solution was then pipetted onto each chamber in a six-well plate and cooled.

The soft agarose overlay was subsequently assembled: 2.4 % low-melting-point agarose (Sigma-Aldrich) was made with milliQ and microwaved until dissolved. The mix was then kept in 50° C waterbath together with 30 mL ALT DMEM for 10 minutes. The agarose solution was then mixed 1:3 with growth medium, placed back into the waterbath and the temperature was decreased to 40° C.

Meanwhile, cell solutions were prepared at a concentration of $8 \cdot 10^4$ cells/mL in growth medium. These cells were 24 hours in advance labeled with glycogen nanoprobe in monolayer, as described for *in vitro* MRI experiments. After trypsination and dilution, the cells were kept in 15 mL tubes in the CO_2 incubator for ten minutes together with disposable pipette tips. For each cell line, the cell suspension was mixed 1:1 with low melting point

agarose before 1.5 mL was administered over the base agar in the six-well plates, and put into a refrigerator for 30 minutes. 2 mL ALT DMEM was then overlayed the low melting point agarose, and the six-well plates were incubated for 14 days before the cells were scored for colony formation. The soft agar assay was repeated three times.

3.3 Resazurin assay: Cell viability

A resazurin assay was used to study cell viability during exposure to the nanoprobe, in which measured metabolism of labeled cells was compared to unlabeled. Four 96-well plates (Nunc) per cell line were prepared with $5 \cdot 10^3$ cells/well. An additional plate with ALT DMEM without cells was also prepared. After 24 hours of incubation, nanoprobe was added to the wells in concentrations of 100, 200, 300 or 400 μg/mL. Unlabeled wells were used as NCs. After another 24 hours of incubation, *one* column of each dose and cell line was used for viability sampling: Resazurin solution (0.1 mg/mL, Sigma-Aldrich) was added at a volume corresponding to 10 % of the volume of medium within each well. This was followed by signal read-out using a multilabel counter platereader (Perkin Elmer, Turku, Finland) after 4 hours. The next day, a new row was added resazurin and measurements sampled in the same manner. This was repeated for five days in total to study cell viability after elevated incubation times with the nanoprobe. After each step of measurements, cell viability was visually confirmed well by well using an in-lab light microscope. The obtained measurements were in relative fluorescence units (RFUs) and based on six parallels.

3.4 Pilot *in vivo* experiments

We performed a pilot animal experiment to determine the suitability of the nanoprobe *in vivo.* The National Animal Research Authority approved all animal procedures. 12 weeks old female nod/scid mice were injected subcutaneously with $1 \cdot 10^6$ H1_DL2 cells in the left upper thigh (two animals), or the neck region and the left upper thigh (three animals) as illustrated in Figure 8. The animals were then kept in the animal facility under standard conditions; being fed a standard pellet diet and provided water *ad libitum*.

After two and four weeks, bioluminescence imaging (BLI) was performed to assess tumor development and growth. Briefly, anaesthetized mice were injected intraperitoneally with D-luciferin (150 mg/kg) 10 min prior to whole body imaging, performed with an Optix® MX2 Small Animal Molecular Imager (ART Inc., Saint-Laurent, QC, Canada). Bioluminescent

images were acquired with Optix® OptiviewTM (ART Inc.) acquisition software (version 2.00) and analysed using Optix® OptiviewTM (version 2.00.01, ART Inc.). ROIs were defined over each injection site and the emitted signal was detected at 560 nm. The pseudocolor intensity format was then calibrated for all images.

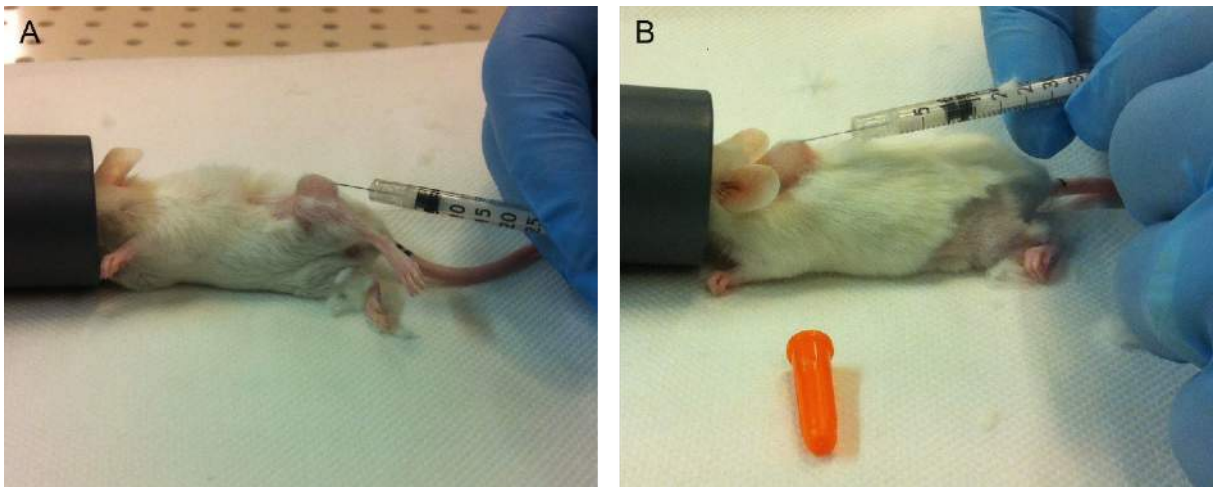

Figure 3.1: Subcutaneous tumor cell injections into five nod/scid mice. All mice received one injection into their left flank; over the upper thigh and apart from the back and abdomen (A), whereas two of these additionally received one injection administered to their necks as well (B).

For *in vivo* use, 15.7 mg of the glycogen nanoprobe was mixed with 1 mL physiological NaCl (0.9 %) to yield a solution containing 0.1 mmol Gd, corresponding to the concentrations of the T_1 reducing contrast agent Omniscan (GE Healthcare, Fairfield, CT, USA). Each animal was first studied with one of the contrast agents, and after 24 hours the same animal was studied using the other contrast agent. A 40 mm quadrature volume coil was mounted onto the table together with a bed tip. Followed by a Tripilot, T_2 scans were performed in axial and coronal orientations (TR: 4300 msec, TE: 36 msec, FOV: 4 cm, Matrix: 256x256, Slice thickness: 1.5 mm, Number of slices: 25, NEX: 3, Scan time: 7 minutes). T_1 scans were then performed before and immediately after contrast agent administration (TR: 600/1000/1200 msec, TE: 9 msec, FOV: 4 cm, Matrix: 256x256, Slice thickness: 1.5 mm, Number of slices: 11, NEX: 6, Scan time: 4 minutes). Signal intensities within tumor ROIs were then compared on the T_1 weighted MR images obtained after contrast injections.

4. Results

4.1 Pilot project: Cellular internalization of the nanoprobe

The pilot project was primarily done to demonstrate cellular internalization of the glycogen nanoprobe. In addition, cellular fluorescence intensity as a function of incubation time and dose was also discerned. The micrographs obtained using Nikon TE2000 in the pilot project, clearly demonstrated that the nanoprobe was internalized in the three cell lines used. This was manifested by fluorescence signal observed from the cytoplasmic segments of cells, through light emission detected at wavelength 643 nm. The results are presented in Figures 4.1-4.3. All images were captured with a 20X objective.

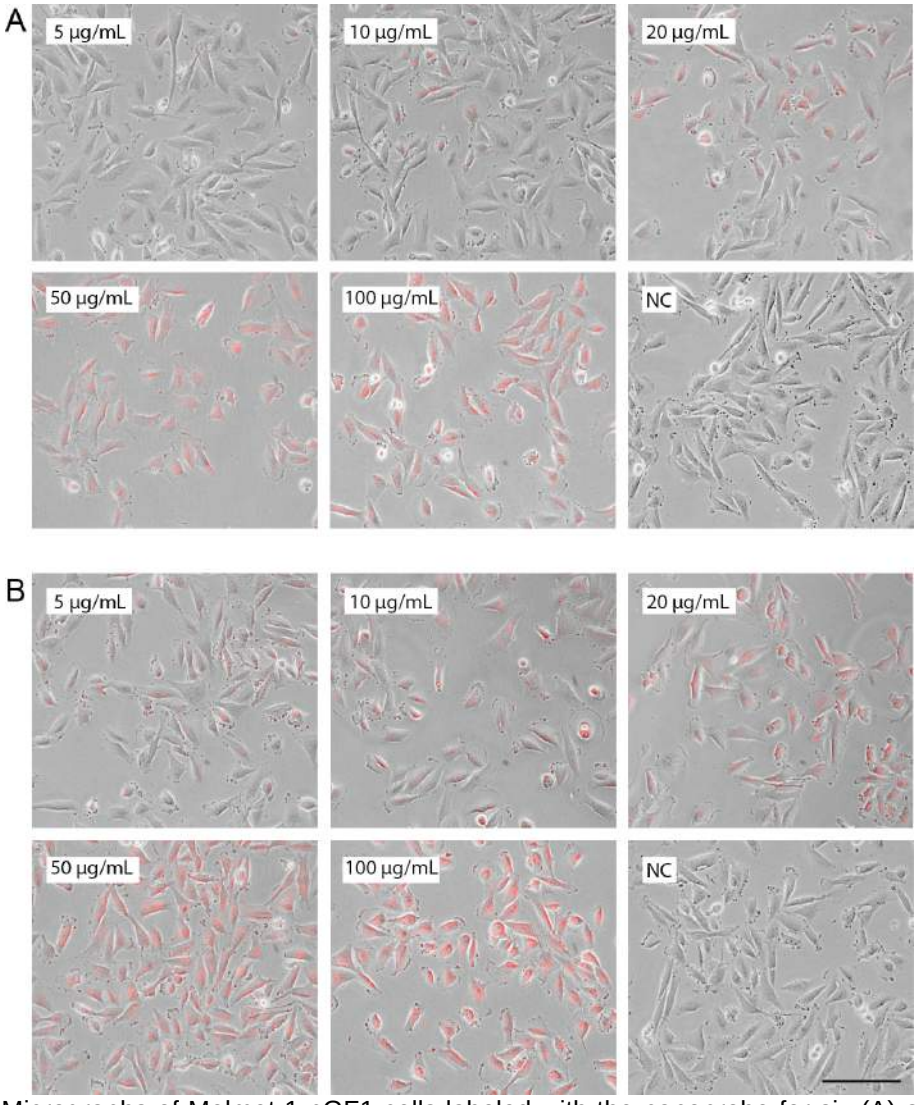

Figure 4.1: Micrographs of Melmet 1 pGF1 cells labeled with the nanoprobe for six (A) and 24 hours (B). The different nanoprobe concentrations are presented on each image (ranging from 5 to 100 µg/mL). A negative control (NC) is included to the lower right. Scalebar: 100 µm.

Melmet 1 pGF1 cells displayed a broad lamellipodium and an independent growth pattern for labeled and unlabeled single cells. It was observed that the degree of fluorescence increased with elevated dye concentration administered to the Melmet 1 pGF1 cells (Figure 4.1). The fluorescence intensity also increased with longer incubation times, which can be seen when comparing the corresponding samples in Figure 4.1 A and B. This was in particular true for the highest dose (100 µg/mL).

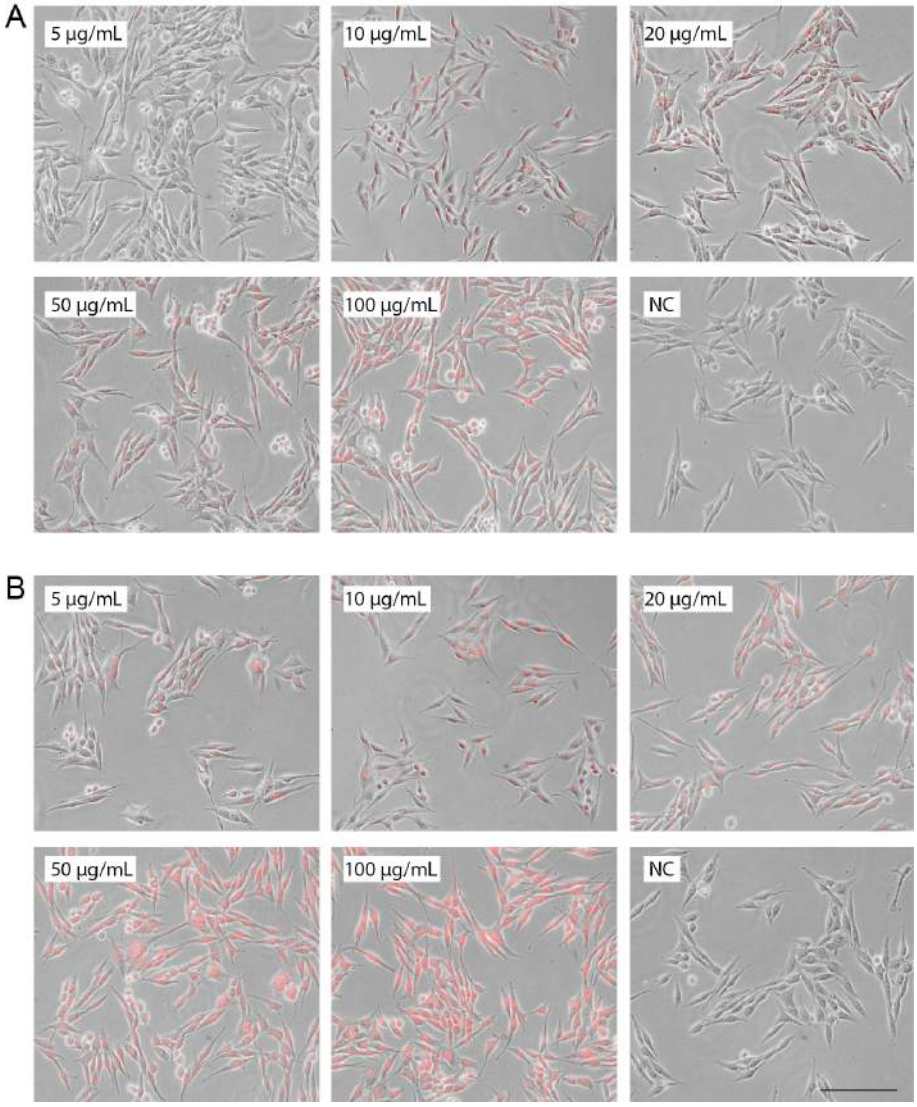

Figure 4.2: Micrographs of Melmet 5 pGF1 cells labeled with the glycogen nanoprobe for six (A) and 24 hours (B). The different nanoprobe concentrations are presented on each image (ranging from 5 to 100 µg/mL). A negative control (NC) is included to the lower right. Scalebar: 100 µm.

The Melmet 5 pGF1 cells held a star-like morphology with elongated filopodia and presented with a growth pattern in patches. Similar to the Melmet 1 pGF1 cells, it was noted that the cellular fluorescence intensity increased with higher nanoprobe doses and extended incubation times for Melmet 5 pGF1 as well (Figure 4.2).

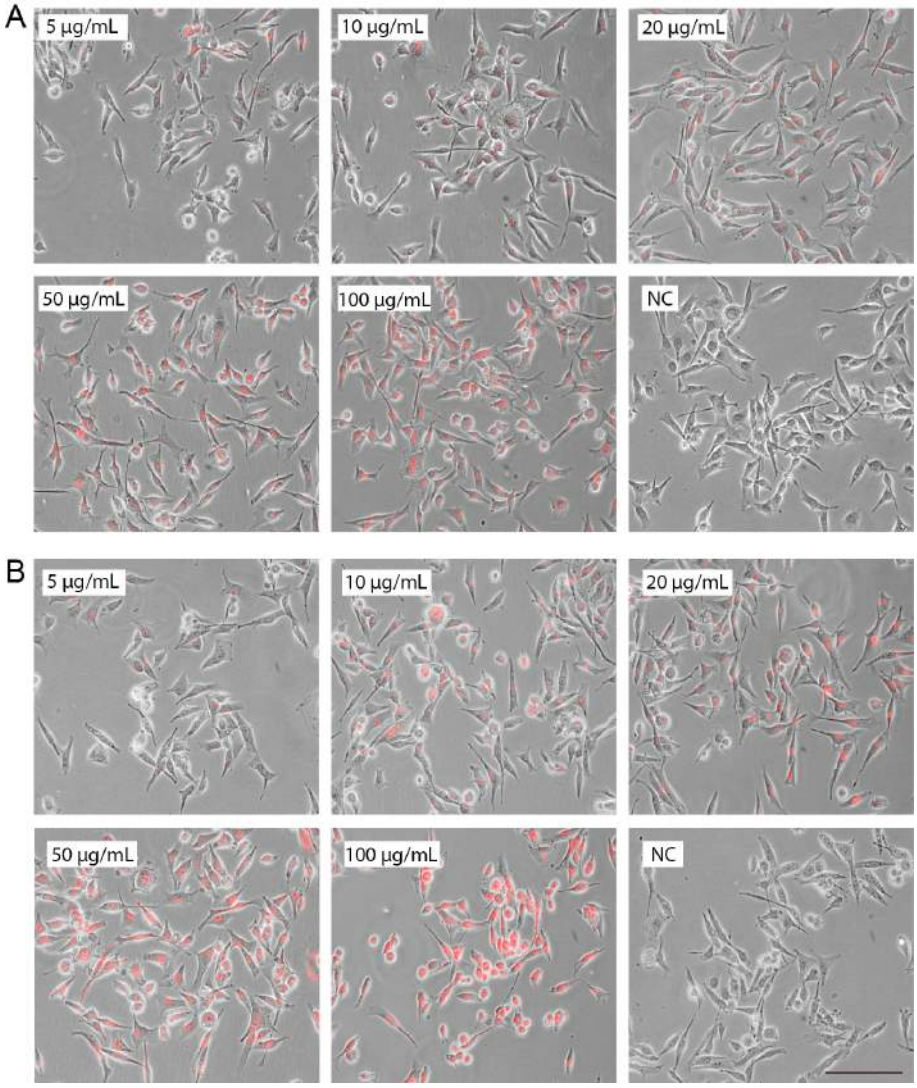

Figure 4.3: Micrographs of H1_DL2 cells labeled with the glycogen nanoprobe for six (A) and 24 hours (B). The different nanoprobe concentrations are presented on each image (ranging from 5 to 100 µg/mL). A negative control (NC) is included to the lower right. Scalebar: 100 µm.

The micrographs of the third cell line, H1_DL2 (Figure 4.3), revealed cell morphology similar to Melmet 5 pGF1 cells. Increased fluorescence intensity was manifested with higher doses and elevated incubation times. Compared to Melmet 1 pGF1 and Melmet 5 pGF1, it seemed to be a stronger fluorescence signal from the H1_DL2 samples at the highest doses; 50 and 100 µg/mL glycogen nanoprobe (Figure 4.3).

In general, it was observed that increased incubation times had great impact on cellular fluorescence intensity for all three cell lines investigated. This was particularly the case for doses above 50 µg/mL, whereas the lower doses did not result in distinctly increased intensities. To verify the visually observed increase in fluorescence intensity as well as the individual tendencies and differences for the three cell lines studied, all micrographs acquired

during the pilot project were quantified as described in Chapter 3.2.1. The average value from all measurements is presented in Figure 4.4, where intensities found in micrographs acquired after six and 24 hours incubation time with the glycogen nanoprobe are displayed. Corresponding cell lines and nanoprobe doses at the two time points were compared statistically using a two-tailed Students *t*-test and presented over the graphs in Figure 4.4 B.

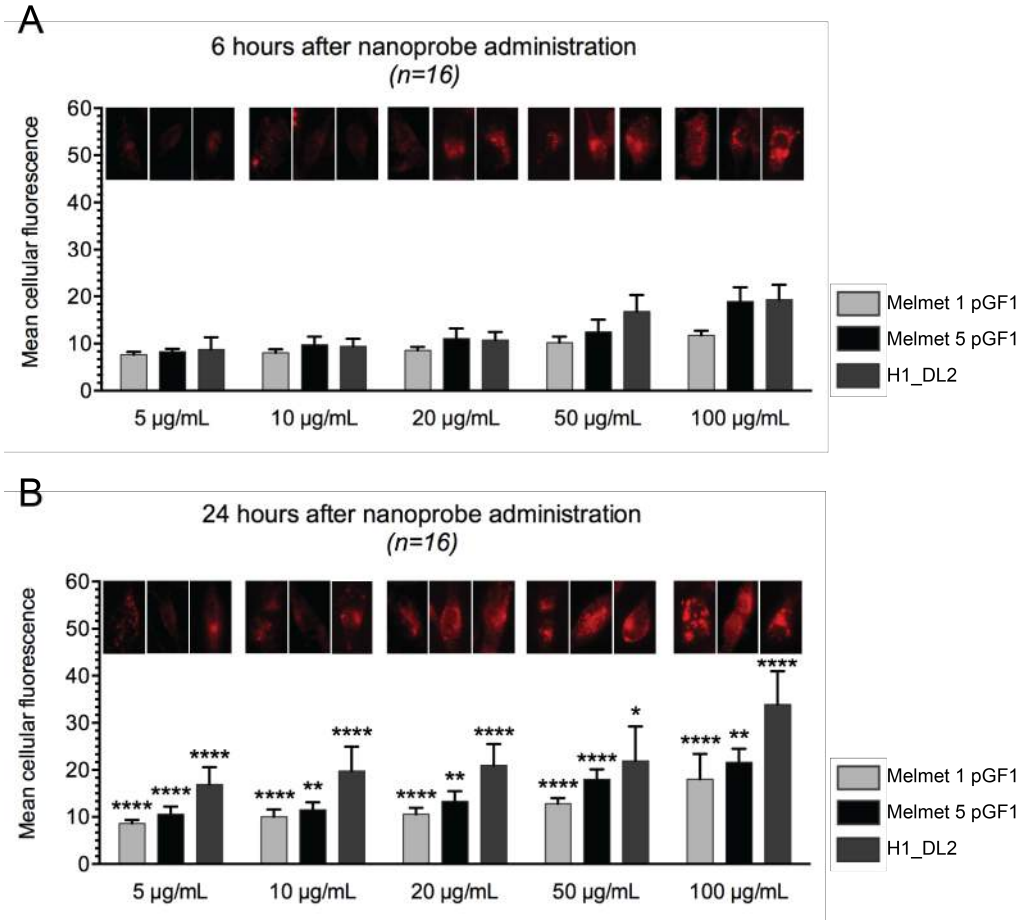

Figure 4.4: Fluorescence intensity graphs of Melmet 1 pGF1, Melmet 5 pGF1 and H1_DL2. The measurements were done in four representative images corresponding to Figures 4.1-4.3. Cells were incubated with glycogen nanoprobe for six hours (A), and 24 hours (B). The fluorescence level shown on the y-axis ranges from 0-255. A random single cell from each set of images is placed above each graph. Abbreviations: *: <0,05, **: <0,01 and ****: <0,0001. Mean ± standard deviation (SD).

From Figure 4.4 it is noted that all measurements at 24 hours incubation time were significantly higher than the corresponding measurements at six hours. No major difference between cell lines was according to Figure 4.4 A registered beneath a nanoprobe dose at 20 µg/mL. For all other measurements, a pattern is manifested in which Melmet 1 pGF1 cells display the lowest fluorescence intensity, Melmet 5 pGF1 cells in between and H1_DL2 cells the highest, suggesting that this cell line is easier to label than the other two. Two-way ANOVA for 4.7 A and B gave p-values <0.0001 and =0.0002, respectively.

As a final study in the pilot project, we investigated whether all or only a subset of the cells within each sample had internalized the nanoprobe. For nanoprobe doses below 10 μg/mL at six hours incubation time, we estimated a labelling efficiency at 99.865 % for Melmet 1 pGF1, 99.932 % for Melmet 5 pGF1 and 100 % for H1_DL2. All samples above this dose, and all doses at incubation time 24 hours, showed a 100 % labeling efficiency. To display the findings, binary images of the samples containing the lowest nanoprobe doses (5 μg/mL) for the shortest incubation time period (6 hours) were created using Matlab as shown in Figure 4.5.

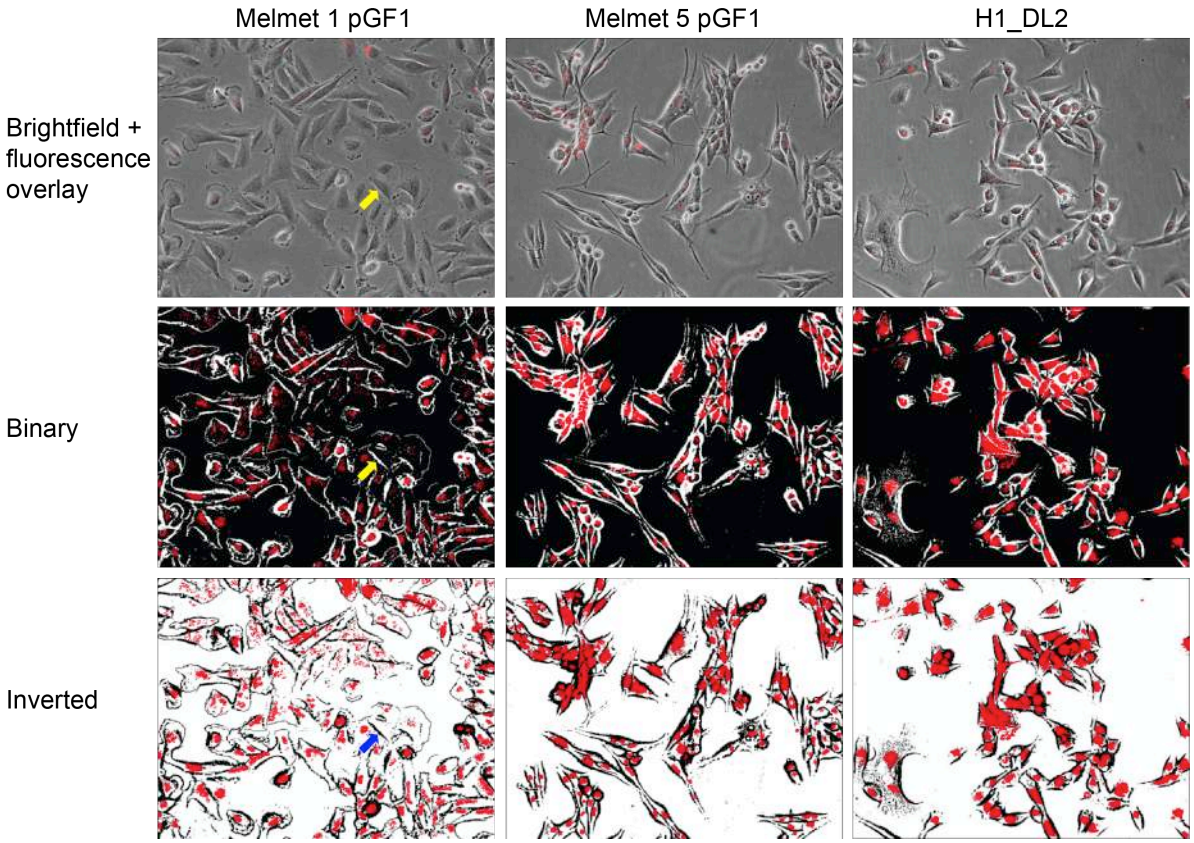

Figure 4.5: Binary images of Melmet 1 pGF1, Melmet 5 pGF1 and H1_DL2. The top row demonstrates the starting point for processing of binary images; brightfield microscope images with fluorescence layers superimposed. The middle row displays the corresponding binary images with black backgrounds, whereas the lower row an inverted version of the same image. Yellow or blue arrows demonstrate a single Melmet 1 pGF1 cell without fluorescence signal (Threshold values: Melmet 1 pGF1: Brightfield: 0.37, fluorescence: 0.067, Melmet 5 pGF1: Brightfield: 0.075, fluorescence: 0.08, H1_DL2: Brightfield: 0.45, fluorescence: 0.07).

Figure 4.5 demonstrates 100 % labeling efficiency for all Melmet 5 pGF1 and H1_DL2 cells, whereas one Melmet 1 pGF1 cell does not display any fluorescence signal (yellow/blue arrow). The fluorescence signal within cytoplasm of Melmet 1 pGF1 cells was in general more dispersed compared to the other two cell lines. A sporadic appearance of multinucleated Melmet 5 pGF1 and H1_DL2 cells was registered, both for labeled and unlabeled cells.

4.2 HTI experiments: Determination of suitable nanoprobe doses

As cellular internalization of the nanoprobe was confirmed, the next goal was to decide a suitable dose for use in further experiments. The results in Chapter 4.1 showed a relatively weak staining for the Dyo-615 segment of the nanoprobe for the given concentrations. Thus all images had to be adjusted for exposure time, gain and contrast in order to detect the fluorescence labeling. In the following experiment we therefore decided to increase the concentrations of the nanoprobe.

It had already been observed that extended incubation times strongly affected cellular fluorescence intensity, and further titrations of this aspect were therefore introduced after elevating the nanoprobe doses; two and four hours of incubation with the nanoprobe.

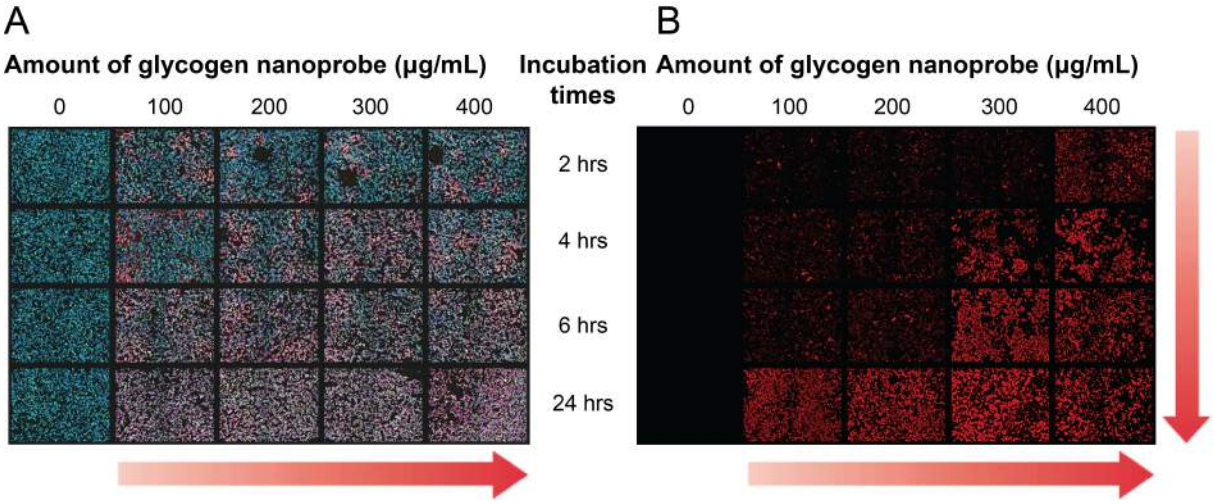

Figure 4.6: Representative overview of part of the 96-well plate layout used for the HTI experiments of Melmet 5 pGF1 (A) and the red image channel for H1_DL2 (B). In 4.6 A, three channels are superimposed on each other, Hoechst 33342 (blue), GFP (green) and Dyo-615 (red). Thick red arrows illustrate how the red fluorescence increased in a gradient-fashion due to increasing nanoprobe doses and incubation times. Images were acquired with a 10X objective. Collages were created in CellProfiler.

Figure 4.6 shows that a gradient of increasing red fluorescence was induced with increasing nanoprobe doses and incubation times, as illustrated with the red arrows. Figure 4.6 B better visualizes the fluorescence from the red image channel due to superimposition of three channels in Figure 4.6 A (GFP, Hoechst 33342 and Dyo-615). All representative images acquired during HTI experiments were thereafter quantified to easier demonstrate cellular fluorescence intensities within the three cell lines studied. In the following Figures 4.7-4.9, all measurements at 24 hours incubation time are compared statistically using a two-tailed Students *t*-test.

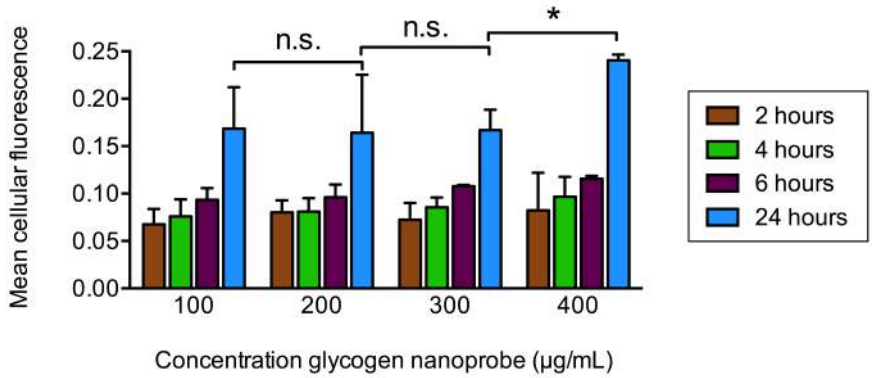

Figure 4.7: Intensity graphs on Dyo-615 fluorescence for Melmet 1 pGF1. The numbers on the x-axis correspond to concentration nanoprobe given to the cells in units µg/mL. The y-axis shows the relative pixel intensities represented by the different samples. Abbreviations: n.s.: not significant, *: p<0,05. Mean ± SD, n=2.

When comparing Melmet 1 pGF1 cells labeled with 100 and 200 µg/mL, and 200 with 300 µg/mL for 24 hours, respectively, none of the measurements displayed significantly different fluorescence intensities. Cells labeled with 400 µg/mL contrast agent showed the highest cellular fluorescence intensity. A two-way ANOVA, in which different time points were compared, resulted in a p-value of 0.22.

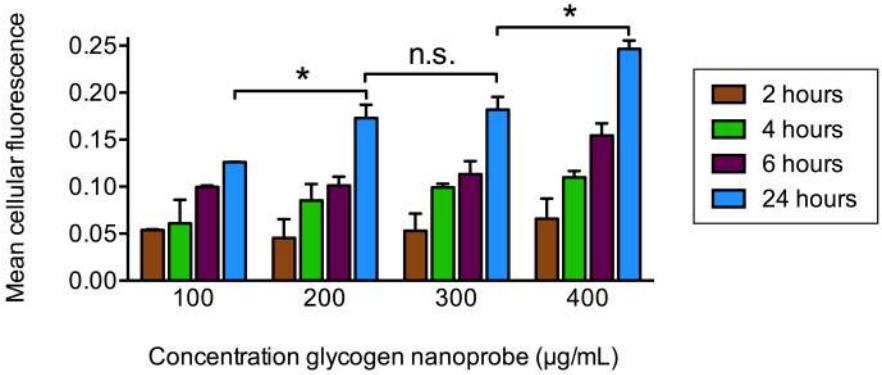

Figure 4.8: Intensity graphs on Dyo-615 fluorescence for Melmet 5 pGF1. The numbers on the x-axis correspond to concentration nanoprobe given to the cells in units µg/mL. The y-axis shows the relative pixel intensities represented by the different samples. Abbreviations: n.s.: not significant, *: p<0,05. Mean ± SD, n=2.

Melmet 5 pGF1 cells showed significantly higher fluorescence intensity when comparing 100 with 200 µg/mL and 300 with 400 µg/mL, but not between 200 and 300 µg/mL. The highest intensities were equally as for Melmet 1 pGF1 cells found for contrast agent labeling with 400 µg/mL. Two-way ANOVA test resulted in a p-value of 0.008.

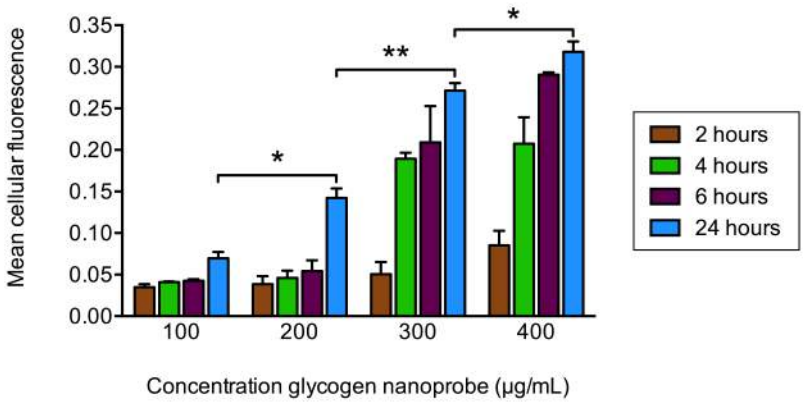

Figure 4.9: Intensity graphs on Dyo-615 fluorescence for H1_DL2. The numbers on the x-axis correspond to concentration nanoprobe given to the cells in units µg/mL. The y-axis shows the relative pixel intensities represented by the different samples. Abbreviations: n.s.: not significant, *: p<0,05, **: <0,01. Mean ± SD, n=2.

H1_DL2 on the other hand, showed a larger increase with elevated nanoprobe doses than the other two cell lines, for which all compared measurements at 24 hours incubation time were statistically higher with increasing nanoprobe doses. Two-way ANOVA test resulted in a p-value of <0.0001. Thus, to avoid loading the cells with too much contrast agent, and still achieve a reasonably high fluorescence signal, we chose to work further with a dose at 200 µg/mL with an incubation period at 24 hours.

4.3 Confocal imaging: Intracellular location of the nanoprobe

To better study subcellular location of the glycogen nanoprobe after labeling, single H1 cells labeled with MitoTracker and Hoechst 33342 were studied by confocal microscopy.

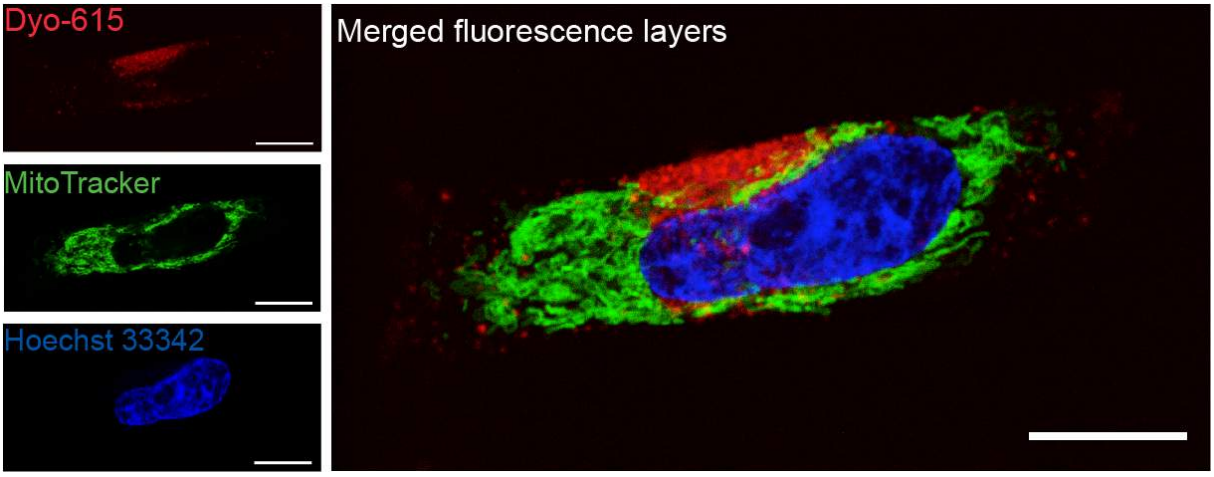

Figure 4.10: Confocal images of a single H1 cell. Red channel shows the Dyo-615 segment of the glycogen nanoprobe, the green channel MitoTracker for labeling of mitochondria and the blue channel Hoechst 33342 for DNA analysis. A merged image of all channels with several cross-sections is seen to the right. Scalebars 20 µm.

The micrographs showed no colocalization between Dyo-615 and MitoTracker. A concentrated area of signal from Dyo-615 was detected in the perinuclear region and also distributed in several small foci throughout cytoplasm as seen in Figure 4.10.

4.4 Resazurin assay: Cell viability

The viability of labeled cells was studied by using a resazurin-resorufin reduction assay as described in Chapter 3.3. All cell samples were seeded at day one, nanoprobe added after an incubation time of 24 hours before resazurin solution was added after the exposure times shown on the x-axis in all diagrams in Figures 4.11-4.13. The measurements in relative fluorescence units (RFU) indicate proliferating and thereby viable cells sampled four hours after adding resazurin to the 96-well plates with labeled cells. Unlabeled cells, "NC", were statistically compared to cells labeled with a nanoprobe dose of 200 µg/mL using a two-tailed Students *t*-test.

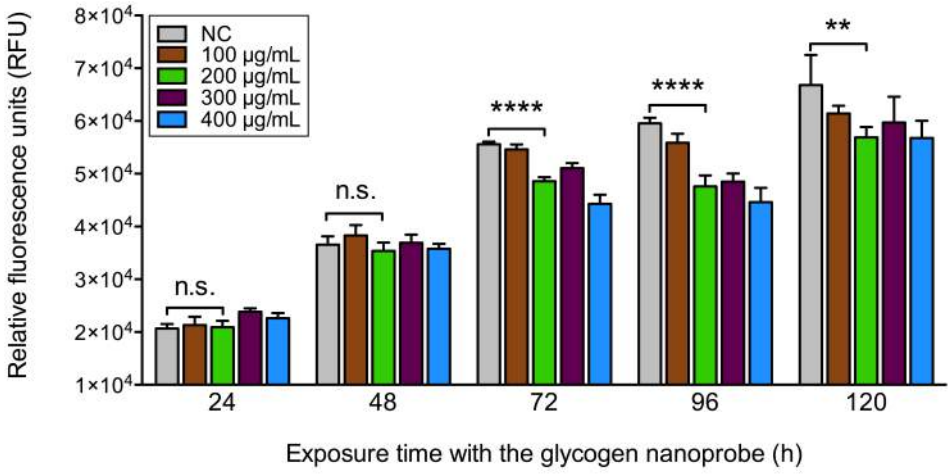

Figure 4.11: Cell metabolism graphs of Melmet 1 pGF1 with increasing exposure time with the glycogen nanoprobe in multiple 96 well plates. Abbreviations: RFU: relative fluorescence units, NC: negative control, ns.: not significant, **: p<0,01, ****: p<0,0001. Mean ± SD, n=6.

Figure 4.11 demonstrates a temporal increase in Melmet 1 pGF1 proliferation as seen by the increasing RFU numbers. It was also seen that Melmet 1 pGF1 cells were minimally affected by being labeled with the nanoprobe up to 48 hours in culture. From 72 hours, labeled cells had a lower capacity to reduce resazurin to resorufin, which indicated decreased proliferation.

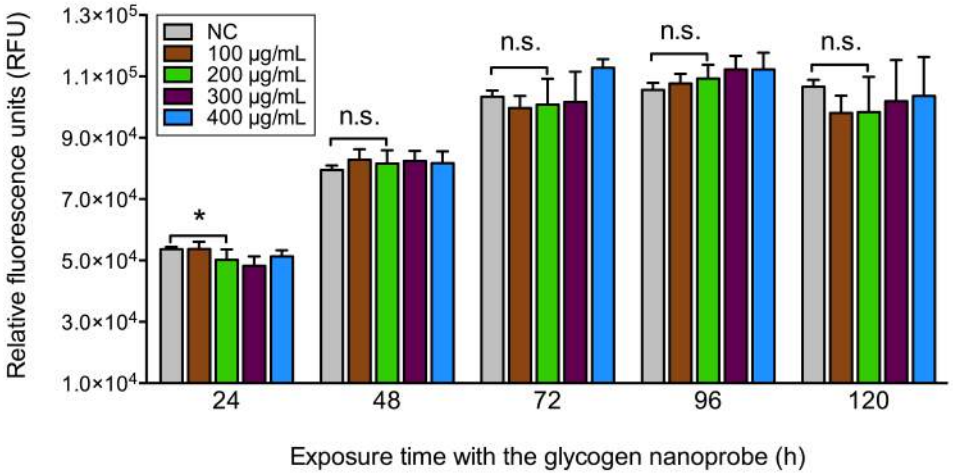

Figure 4.12: Cell metabolism graphs of Melmet 5 pGF1 with increasing exposure time with the glycogen nanoprobe in multiple 96 well plates. Abbreviations: NC: negative control, ns.: not significant; *: <0,05. Mean ± SD, n=6.

Figure 4.12 indicates that the proliferation rate of labeled as well as unlabeled Melmet 5 pGF1 cells leveled somewhat of after 72 hours in culture. At 24 hours, cells labeled with 200 µg/mL nanoprobe showed a lower proliferation than unlabeled cells. From sampling times 48 to 120 hours, no significant difference between the two populations was detected.

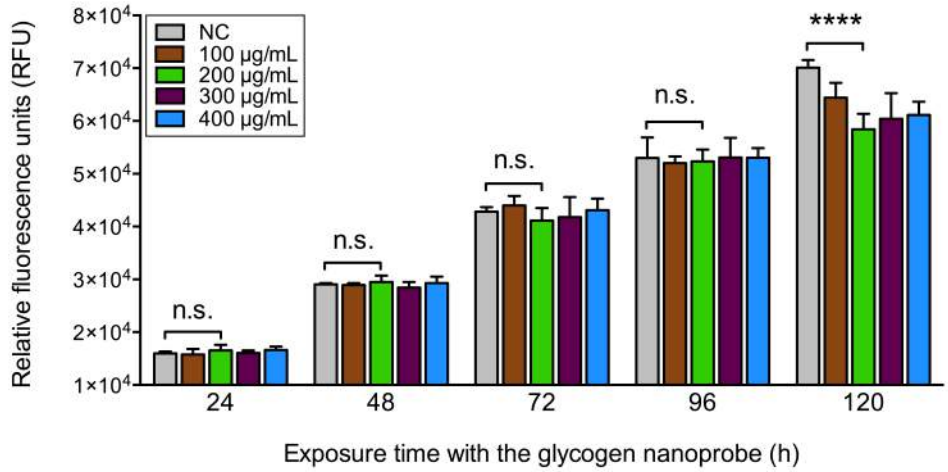

Figure 4.13: Cell metabolism graphs of H1_DL2 with increasing exposure time with the glycogen nanoprobe in multiple 96 well plates. Abbreviations: NC: negative control, ns.: not significant, ****: p<0,0001. Mean ± SD, n=6.

H1_DL2 cells showed a temporal increase in RFUs for all time points. No statistical difference was found between labeled and control H1_DL2 cells for timepoints prior to 120 hours of exposure to the nanoprobe.

4.5 Monolayer wound healing assay: Cellular migration

Melmet 1 pGF1 cells labeled with 200 µg/mL glycogen nanoprobe were studied and compared to unlabeled Melmet 1 pGF1 cells in a monolayer wound healing assay. This is based on the cells properties to close an induced wound, to reestablish intercellular contact.

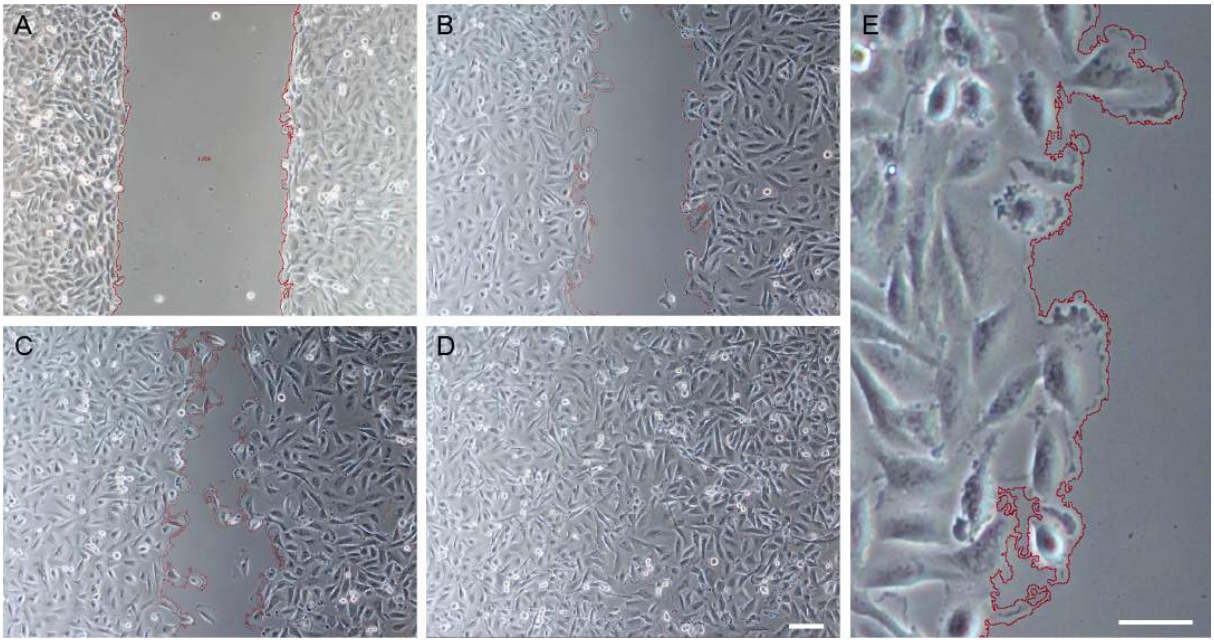

Figure 4.14: Representative monolayer wound healing micrographs of Melmet 1 pGF1 cells. The red borders around the wound illustrates wound size at 0 (A), four (B), eight (C) and 14 (D) hours after initiation of the experiment. Scalebar for A-D is 100 µm as seen in D. A zoomed area of the red border at two hours is included in E, with scalebar 50 µm. All micrographs are captured with objective 10X.

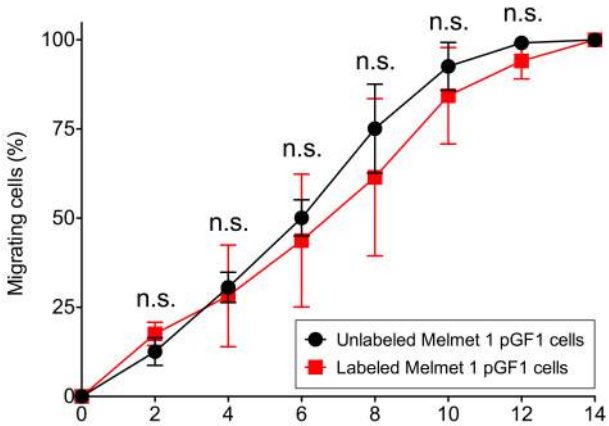

Figure 4.15: Quantification of monolayer wound healing. Four representative images from each time point as seen on the x-axis were quantified as percent migrating Melmet 1 pGF1 cells until cell confluency within the wound area. Abbreviations: n.s.: not significant. Mean ± SD, n=4.

Quantification as seen in Figure 4.15 was enabled using the red outlines created in FIJI and as shown in Figure 4.14. The resulting numbers showed that there was a tendency that labeled cells migrated more slowly than unlabeled cells, with no significant difference at either time point. Both cell samples displayed confluency 14 hours after start of the experiment.

4.6 Duration of cellular fluorescence: Nanoprobe clearance

It was expected that the cultured cells exocytosed the nanoprobe gradually over time alongside with ongoing proliferation. Thus, the duration of fluorescent signal from the Dyo-615 encompassed in the nanoprobe was used to study this. The cells were examined by light microscopy at 0, 24, 48, 72 and 96 hours after an incubation period at 24 hours with 200 µg/mL of the glycogen nanoprobe in growth medium.

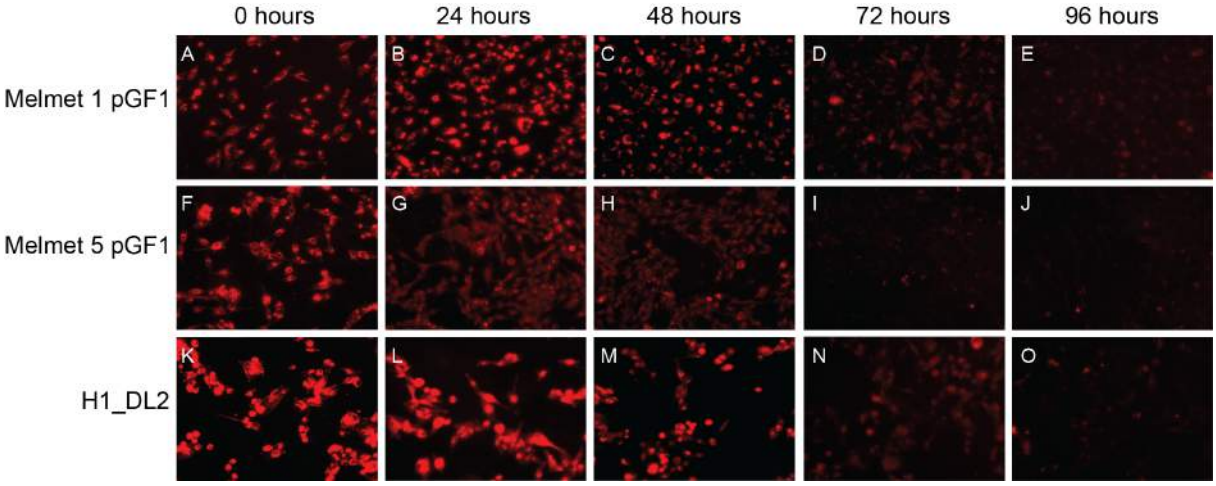

Figure 4.16: Representative microscopy images of Melmet 1 pGF1 (A-E), Melmet 5 pGF1 (F-J) and H1_DL2 (K-O) up to five days after labeling the cells with the glycogen nanoprobe. 20X objective.

Melmet 1 pGF1 cells displayed a slight increase in visual fluorescence intensity from 0 to 24 hours (Figures 4.16 A and B), before it appeared that the fluorescence intensity leveled off (Figures 4.16 C-E). Melmet 5 pGF1 cells displayed the most distinct reduction in fluorescence intensity for all time points (Figures 4.16 F-J). H1_DL2 cells demonstrated the strongest signal of all cell lines initially (Figure 4.16 K). At 48 hours and onwards, a pronounced decrease in fluorescence intensity was noted for all three cell lines. At 96 hours, only fragments of the nanoprobe were left in wells with Melmet 5 pGF1 cells (Figure 4.16 J), whereas a subset of Melmet 1 pGF1 and H1_DL2 cells displayed fluorescence signal from intracellular locations (Figures 4.16 E and O).

The fluorescence intensity of four representative images of each micrograph corresponding to Figure 4.16 were quantified in the same way as in the pilot project and presented in Figure 4.17.

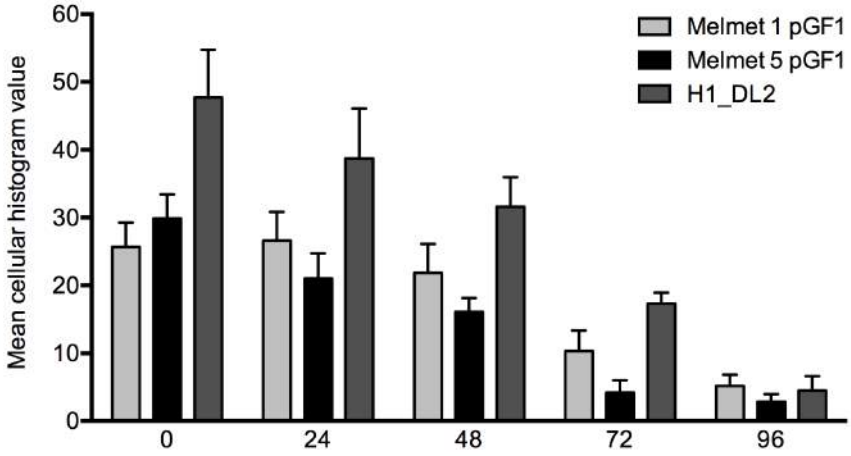

Figure 4.17: Temporal changes in mean cellular fluorescence intensity measured at the timepoints indicated on the x-axis in hours for Melmet 1 pGF1, Melmet 5 pGF1 and H1_DL2. Mean ± SD, n=64.

The numbers seen in Figure 4.17 validate the differences between cell lines observed from the micrographs in Figure 4.16, as well as a temporal decline in fluorescence intensities. Also, a slight increase in fluroescence intensity was verified for Melmet 1 pGF1 cells from 0 to 24 hours. At 96 hours, a mean value of cellular histogram intensity was registered at 3 for Melmet 5 pGF1 cells, which equaled the background noise of all fluorescence images in Photoshop. A two-way ANOVA analysis of the different time points gave $p<0.0001$.

4.6.1 Cell proliferation and death

Cell proliferation and death was monitored alongside with the imaging experiments as described in Chapter 3.2.6 and presented in Figures 4.18-4.20. The time points agree with those in the preceding Figures 4.16 and 4.17.

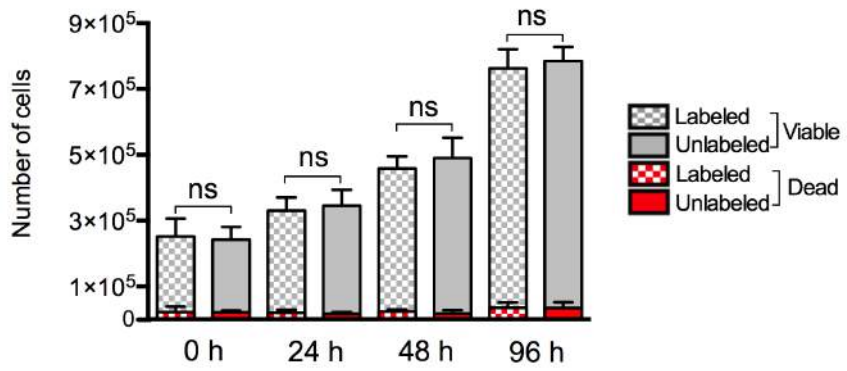

Figure 4.18: Cell proliferation and death for Melmet 1 pGF1. Labeled and unlabeled cells were cultured in six-well plates alongside with imaging experiments, in which labeled cells were constantly exposed to 200 µg/mL glycogen nanoprobe in growth medium. Abbreviations: n.s.: not significant, h: hours. Mean ± SD, n=6.

For Melmet 1 pGF1 (Figure 4.18), there was a tendency that unlabeled cells proliferated faster than labeled from 24 to 96 hours. The number of dead cells found for the two populations was quite similar throughout the sampling time. None of these observations were statistically different when analysed with a two-tailed Students *t*-test.

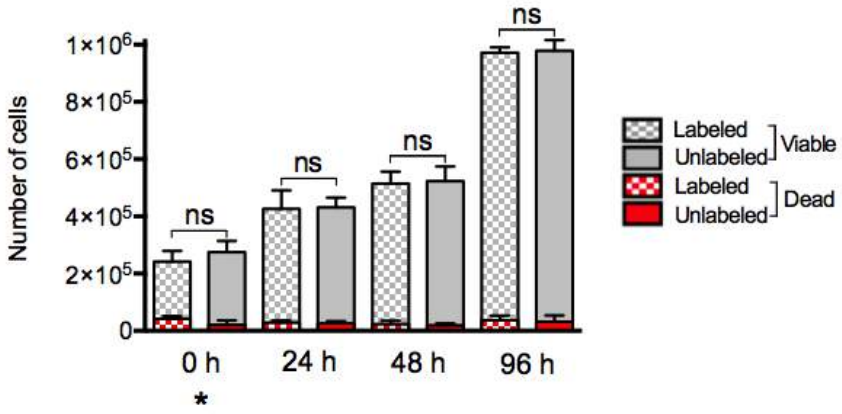

Figure 4.19: Cell proliferation and death for Melmet 5 pGF1. Labeled and unlabeled cells were cultured in six-well plates alongside with imaging experiments, in which labeled cells were constantly exposed to 200 µg/mL glycogen nanoprobe in growth medium. Abbreviations: n.s.: not significant, *: p<0,05 h: hours. Mean ± SD, n=6.

Figure 4.19 demonstrates that Melmet 5 pGF1 proliferation is minimally affected by labeling the cells with glycogen nanoprobe. A significantly higher amount of dead labeled cells compared to unlabeled was found at 0 hours when analyzed with a two-tailed Students *t*-test.

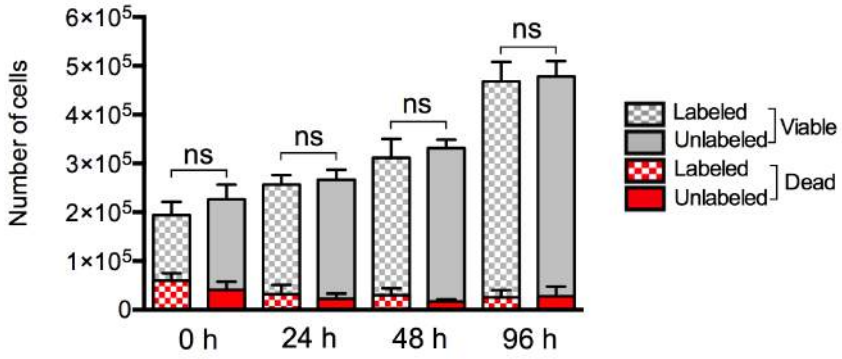

Figure 4.20: Cell proliferation and death for H1_DL2. Labeled and unlabeled cells were cultured in six-well plates alongside with imaging experiments, in which labeled cells were constantly exposed to 200 µg/mL glycogen nanoprobe in growth medium. Abbreviations: n.s.: not significant, h: hours. Mean ± SD, n=6.

Similarly to the Melmet 1 pGF1 cell line, there was a tendency that unlabeled cells proliferated more quickly as also found for the H1_DL2 cells. Also, there was a tendency that labeled cells displayed a higher number of dead cells than unlabeled. An increase in cell death was found for all three cell lines at 96 hours compared to previous time points. A high degree of cell confluency was at that time visually observed within all wells.

4.7 Soft agar assay: Investigation of the cells in a 3D environment

Melmet 1 pGF1, Melmet 5 pGF1 and H1_DL2 cells prelabeled with 200 µg/mL glycogen nanoprobe were cultured in soft agar for 14 days before they were examined for fluorescence using the Nikon TE2000 microscope.

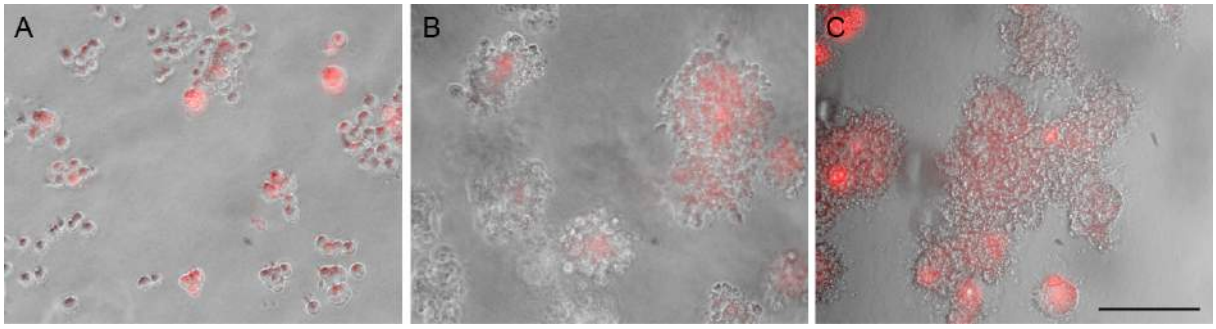

Figure 4.21: Representative images of Melmet 1 pGF1 (A), Melmet 5 pGF1 (B) and H1_DL2 (C) colonies. Scalebar 100 µm. Exposure time Dyo-615: 0.5 s, gain 6.8. n=4 experiments.

The micrographs of Melmet 1 pGF1 cells revealed scattered cells, with a small degree of cellular spheroids. A relatively strong fluorescence signal was detected from the cytoplasm of some of the cells as seen in Figure 4.21 A. Melmet 5 pGF1 cells showed a larger ability to form cellular colonies, occuring in z-direction to a larger extent than for the other two cell lines (Figure 4.21 B). The fluorescence signal was also detected from these cells, especially the central parts of colonies. Further, the H1_DL2 cells showed smaller and more planar colonies than Melmet 5 pGF1, yet with strong fluorescence signal (Figure 4.21 C).

4.8 Bioluminescent imaging (BLI): Tumor take and development

Tumor-take and progression was revealed by BLI two and four weeks after subcutaneous injection of $1 \cdot 10^6$ H1_DL2 cells into five nod/scid mice as shown in Figures 4.22 and 4.23.

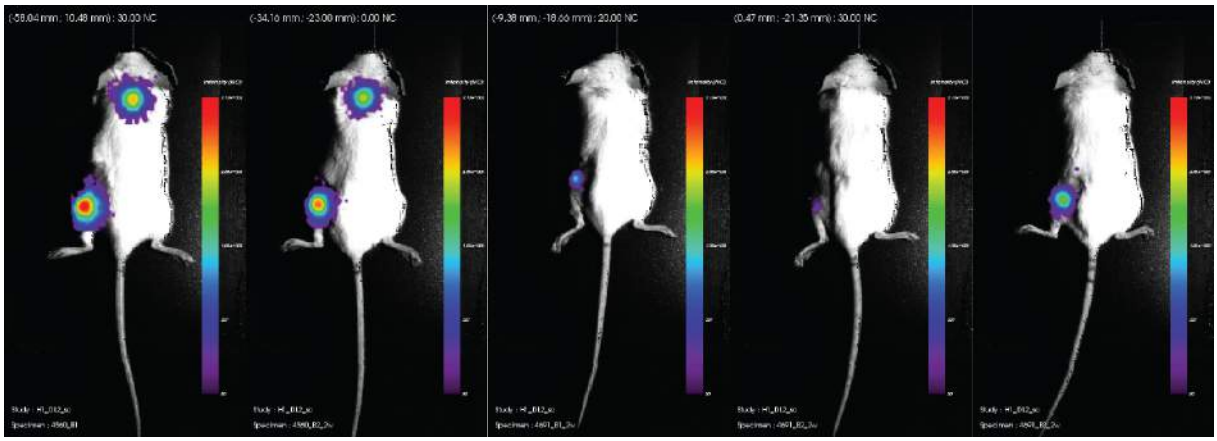

Figure 4.22: Five nod/scid mice injected with $1 \cdot 10^6$ H1_DL2 cells two weeks prior to BLI. Two mice received tumor cells in two locations, whereas the remaining achieved tumor cells into one location.

The images in Figure 4.22 demonstrate that tumors were produced in all mice two weeks after injection. Based on BLI intensity measurements, the two mice that received two injection doses developed larger tumors than those who only received one. Tumors were estimated in the scale of 0.5-2.0 mm diameter.

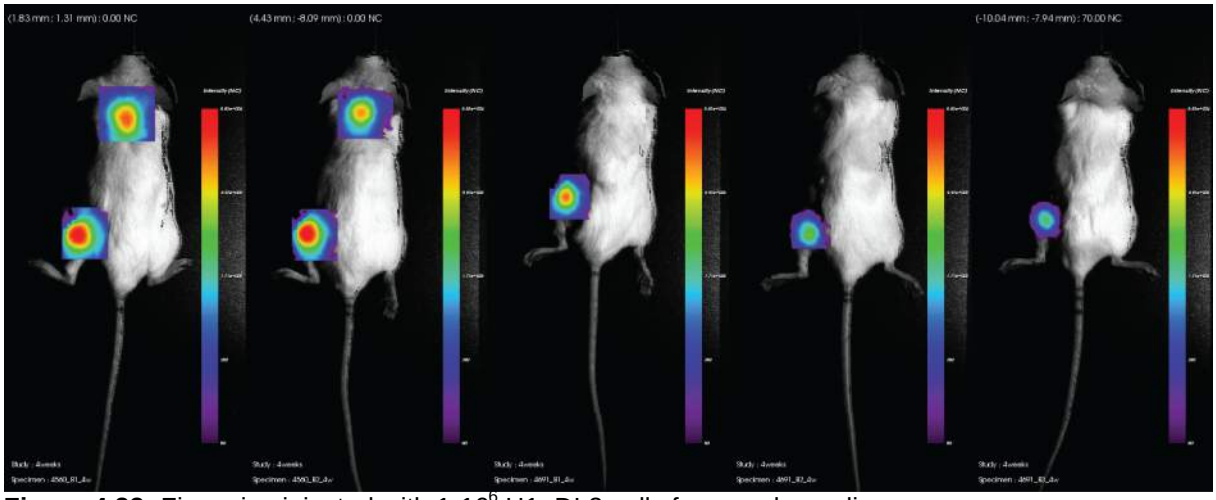

Figure 4.23: Five mice injected with $1 \cdot 10^6$ H1_DL2 cells four weeks earlier.

Figure 4.23 demonstrated further growth of subcutaneous tumors in all mice. According to the intensity scale shown to the right of each animal, none of the tumors had developed hypoxic areas central in the tumors. Approximate tumor size was in the area 3.0 to 5.0 mm in diameter.

4.9 MRI

Before the nanoprobe was tested *in vivo* on tumor-bearing nod/scid mice by MRI, we wanted to study whether the contrast agent was able to reduce the T_1 relaxation times *in vitro*. This was carried out using the phantoms described in Table 4 in Chapter 3.2.3.

4.9.1 *In vitro* MRI: Verification of nanoprobe doses from HTI experiments

A study of changes in relaxation times was performed using the preclinical MR scanner. Since Gd is a T_1 reducing contrast agent, only this parameter was studied, i.e. we did not focus on T_2 relaxation. The measured T_1 relaxation times for the tubes (comparing two and two tubes with equal numbers of labeled and unlabeled cells) were analysed using a two-tailed Students *t*-test. T_1 relaxation times for phantoms with various amounts of cells are shown for Melmet 1 pGF1, Melmet 5 pGF1 and H1_DL2 in Figures 4.24-4.26, whereas values found for control phantoms are listed in Table 5.

Table 5: T_1 constants for control phantoms on Bruker Pharmascan 7 Tesla (T)

Phantom	Content	Agar concentration	T_1 value
I	Agar stock solution	2 %	2 375 ± 66.9911 msec
II	Agar with ALT DMEM	1 %	2 520 ± 59.2117 msec
III	Agar with 1 mg/mL glycogen nanoprobe	1 %	1 132 ± 17.6081 msec
IV	Agar with water	1 %	2 502 ± 67.7428 msec
V	Pure water	0 %	2 720 ± 57.1421 msec

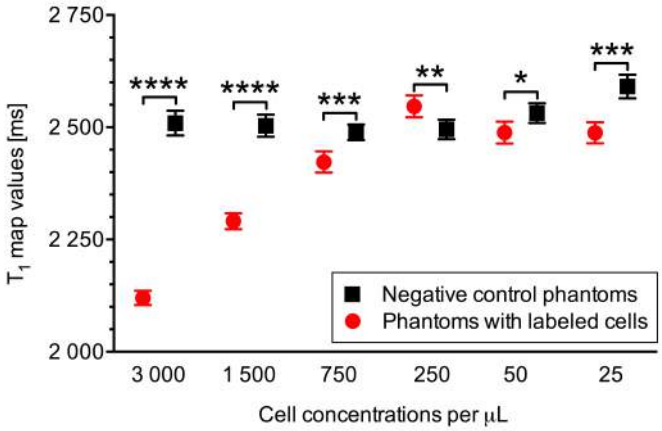

Figure 4.24: T_1 relaxation times for Melmet 1 pGF1 phantoms containing various cell concentrations as indicated on the x-axis. T_1 values were measured in milliseconds (ms). Mean ± SD, n=1.

The T_1 times found for Melmet 1 pGF1 showed a clear reduction in phantoms with labeled cells for the three highest cell concentrations. The corresponding phantoms with 250 cells/µL demonstrate that the effect of contrast enhancement is no longer present.

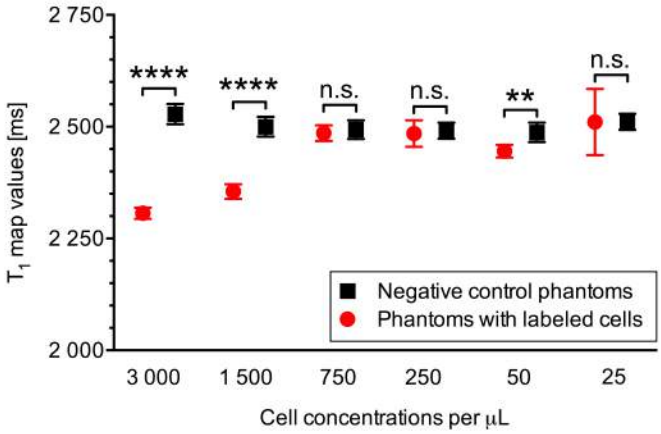

Figure 4.25: T_1 relaxation times for Melmet 5 pGF1 phantoms containing various cell concentrations as indicated on the x-axis. T_1 values measured in ms. Mean ± SD, n=1.

The T_1 relaxation times found for phantoms with labeled Melmet 5 pGF1 cells, showed a smaller reduction compared to what was seen for Melmet 1 pGF1. A significant lower T_1 value was still found for the two highest cell concentrations investigated by MRI. At 750 cells/µL and below, no significant differences between control and test phantoms were found, indicating that it is not possible to detect the T_1 contrast agent at these concentrations.

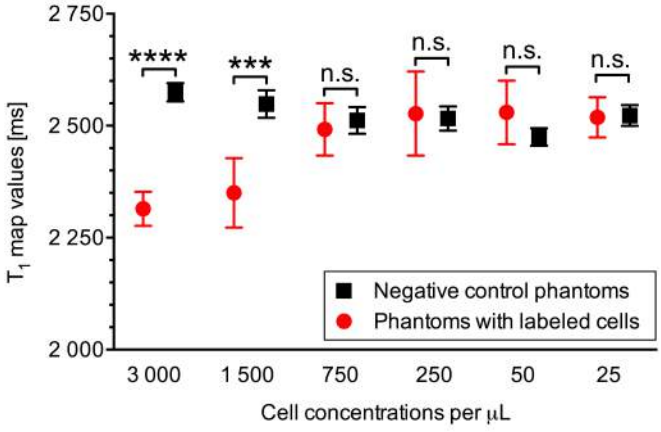

Figure 4.26: T_1 relaxation times for phantoms with labeled and unlabeled H1_DL2 cells, at the concentrations shown on the x-axis. T_1 values measured in ms. Mean ± SD, n=1.

The T_1 times found for H1_DL2 cells, showed the same trend as seen for Melmet 5 pGF1 cells, in that 1 500 cells/µL was the lowest possible concentration for detecting the nanoprobe. At cell concentrations 750 to 25 cells/µL, no significant difference was found.

In general, a quite stable T_1 value was detected for negative control phantoms with a mean value at 2 515.57 ms.

4.9.2 Pilot *in vivo* experiment

Tumor uptake of contrast agent in a nod/scid mouse was studied by MRI after administration of the nanoprobe and Omniscan in corresponding amounts of Gd, as commonly used in the clinic. The results are seen in Figures 4.27 and 4.28.

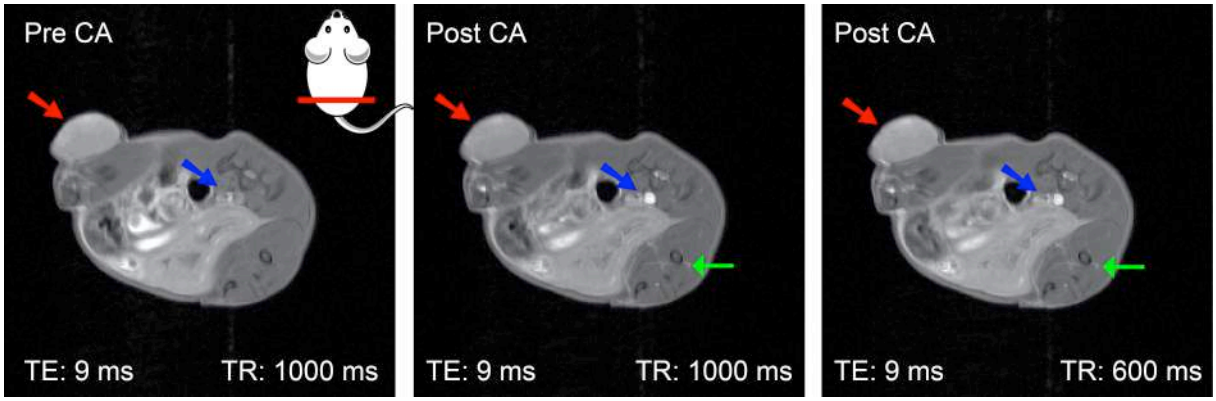

Figure 4.27: T_1 weighted MRI images before (left) and after (middle and right) administration of glycogen nanoprobe. Abbreviations: CA: contrast agent, TR: repetition time, TE: echo time.

An axial slice positioned approximately at the illustration to the left in Figure 4.27 demonstrate little nanoprobe uptake into the tumor (red arrow) regardless of repetition time (TR). It appears that a vessel is better visualized post contrast agent administration at anterior segments of the tumor. The blue arrow illustrates the position of abdominal aorta and vena cava within close proximity, in which bright contrast is detected. Signal from vessels within muscle tissue are brighter post contrast agent administration (green arrow).

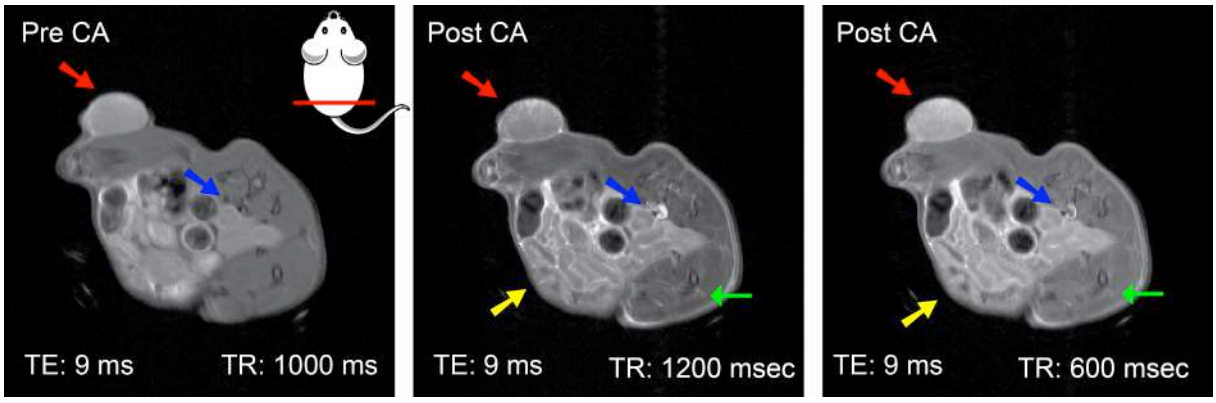

Figure 4.28: T_1 weighted MRI images before (left) and after (middle and right) administration of Omniscan. Abbreviations: CA: contrast agent, TR: repetition time, TE: echo time.

The same nod/scid mouse was 24 hours later examined for contrast agent uptake in the same tumor using Omniscan. From Figure 4.28 it is apparent that the contrast agent was loaded into the tumor (red arrow) as well as intestines (yellow arrow) and vessels within muscle tissue (green arrow).

To quantify and compare the signal intensities, ROIs were created and placed at the contours of the tumor seen in Figures 4.27 and 4.28 and the pixel intensity was found using Photoshop CS5. The results are presented in Figure 4.29.

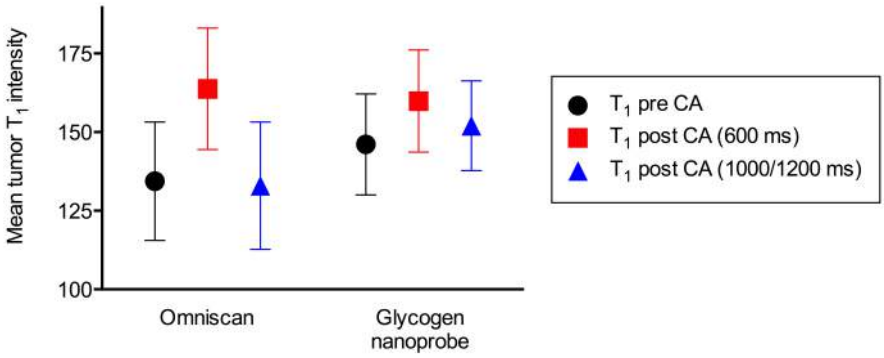

Figure 4.29: T_1 intensity measurements of the flank tumor in T_1 weighted images before and after contrast agent administration at repetition times (TR) 600 and 1 000/1 200 ms, as indicated in the legend. Abbreviations: CA: contrast agent, ms: millisecond, TR: repetition time.

A larger increase in T_1 image brightness linked to tumor uptake of contrast agent was seen for the flank lesion scanned after Omniscan administration. A smaller increase in image brightness is seen for the tumor scanned after administering the nanoprobe.

4.10 Histology

Heamotoxylin and eosin (H&E) stained histological samples of the flank tumor showed central areas of hypoxia within the tumor with mitotic activity and pleomorphic nuclei. Prominent nucleolus and angiogenesis was also seen (data not shown).

5. Discussion

In general, 20-40 % of all cancer patients develop brain metastases during the progression of malignancy, of which a fifth are diagnosed with secondary brain tumors before the primary site neoplasm is located or identified (85). To diagnose brain metastases, varying imaging modalities are used, and these are in general divided into modalities that give information on anatomy and pathology such as MRI, and modalities that produce functional information, such as the metabolism-driven image contrast acquired in nuclear medicine approaches (86). The respective modalities have varying strengths and weaknesses as briefly discussed in Chapter 1. MRI is often the modality of choice to detect CNS lesions due to the high spatial resolution and great soft-tissue contrast. It can still be problematic to detect tumors smaller than 10 mm on MRI (87), which also arises an additional challenge in melanoma patients, as they often develop multiple, small brain metastases (21). Multimodal imaging has emerged as a potent tool for improved detection (88), as this allows signal-reading from one common probe using more than one modality (63).

Recently, increased awareness has been given to the establishment of new nanomaterials for cancer therapeutic, diagnostic or combined purposes (62). The nanomedicine research has become a multi-billion industry, in which the search for new materials and applications constantly continues. Nanomaterials can be used to improve the detection of metastatic disease to the brain, and especially in the multimodal and theranostic settings, suitable probes of nano-scale sizes are needed (74). By combining the emerging potential of multimodal imaging with a promising or well-established therapeutic agent, improved treatment outcome for cancer patients might be a possible impact of such theranostic entities.

In this project a variety of *in vitro* experiments were performed to study the usability of a novel multimodal glycogen nanoprobe developed by Filippov and colleagues (63), on three metastatic melanoma cell lines. Before it is possible to study the theranostic potential of the nanoprobe in an *in vivo* model system, it was regarded imperative to address several fundamental aspects as discussed below and as described in the aims of this thesis. Multiple fluorescence microscopy experiments were thus emphasized, as this is a sensitive and functional way to study such features (89). Further, this provided robust data on cellular internalization of the nanoprobe demonstrated for more than one cell line and validated

several times in different experiments. Any applications of this particular nanoprobe on cancer cell lines have not been described in the literature yet, and the following discussion will thus form a basis for further research on the multimodal glycogen nanoprobe holding a prospective implementation in theranostic research.

5.1 Cellular fluorescence experiments

The initial experiments to study cellular fluorescence intensities were enabled through the Dyo-615 segment of the multimodal nanoprobe. The pilot project demonstrated increased fluorescence intensities as a consequence of elevated doses and incubation times (Figures 4.1-4.3). In general, cellular uptake of macromolecules is presumed to occur through a combination of several possible mechanisms: Energy-dependent endocytosis can occur mediated by cavaeola vesicles, clathrin vesicles, by phagocytosis or pinocytosis, whereas passive uptake can occur by diffusion (90-92). Non-specific uptake means that the cell does not actively request the compound to be internalized, however extraneous material is still taken up by the cell. This usually occurs by pinocytosis for eukaryotic cells (93). To study the exact mechanisms responsible for cellular internalization, other methods besides light microscopy with or without visualization of fluorescence are usually better suited (90). Taken into account the size of the considered nanoprobe, 54.4 nm, some characteristics of internalization mechanisms can still be discussed. Several papers report that nanomaterial size is one of the most important predictors of cellular internalization (93-96). Meng and colleagues reported that a nanoparticle with a diameter at 110 nm was internalized into HeLa cells and a lung cancer cell line through macropinocytosis, which was determined due to the presence of large cytoplasmic vesicles (97). Further, Yoo and colleagues describe that particles at a size of 60 nm entered a cell line derived from liver cancer through a combination of passive diffusion and non-specific endocytosis (98). Internalization of particles below a size of 30 nm is usually less dependent on particle size and a combination of several factors such as particle morpholology, charge and the cell type studied is more decisive with respect to internalization mechanism (90). Thus, it can be indicated that the size of the glycogen nanoprobe is within the limit of what might involve passive diffusion and non-specific endocytosis. This is in accordance with Glaumann and colleagues who performed *in vivo* experiments on rats. In their studies, glycogen labeled with isotopes was injected intravenously, before cellular internalization was studied by electron microscopy. Their findings also suggested non-specific endocytosis (99). On the other hand, Rejman and

colleagues demonstrated cellular uptake of microspheres at 50 nm into a melanoma cell line to occur through clathrin-mediated pathways (100). Thus, additional studies are needed to specifically investigate the exact internalization mechanism of the glycogen nanoprobe taken into account other aspects such as the charge of the probe. Nevertheless, the pilot project demonstrated that the probe was internalized into all three cell lines investigated, which was essential for further experiments with the glycogen nanoprobe.

From the pilot project we observed cellular fluorescence signal dispersed throughout cytoplasm, and that larger portions of the cells were stained the higher the nanoprobe doses used. When single H1 cells were investigated with confocal microscopy, signal from Dyo-615 was observed concentrated in the perinuclear region and scattered throughout the cell in focal areas of varying sizes (Figure 4.10). No colocalization with labeled mitochondria was detected, which excludes accumulation into this organelle. Although no fluorescent markers for these sites were used, the images might indicate that the probe was accumulated in Golgi apparatus or endoplasmic reticulum (ER) and vesicles of varying sizes. Seen in context with Glaumanns and Rejmans research (99, 100) as mentioned above, we have reason to assume that these vesicles are endosomes or matured lysosomes. Different degradation enzymes are abundantly present in lysosomes for breakdown of several biomolecules such as glycogen. This organelle varies in size dependent on activity (101), which was also observed in our confocal experiments. Nanomaterial concentration within these sites is also in consistence with Kelf and colleagues research (93). This can be studied by using customized organelle dyes and subsequent analysis for any colocalization with Dyo-615 by confocal microscopy. Glycogen was found within lysosomes by Glaumann up to 24 hours after administration, before the end products escaped back into the cytoplasma (99). Possible subsequent employment of degraded glycogen might be glycolysis, pentose phosphate pathway or production of glucose, which occurs in the cytoplasm and is often not associated with any organelle-specific site (102, 103).

A labeling efficacy at 100 % was found for 24 hours of incubation, whereas a relatively high efficacy was found for six hours of incubation as well (Figure 4.5). Rejman and colleagues also studied cellular internalization efficacy of microspheres of higher diameters; 100, 200, 500 and 1000 nm (100). By confocal microscopy and fluorescence-activated cell sorting (FACS), they demonstrated that all types of particles below a diameter of 500 nm were efficiently internalized under normal incubation conditions, and that particles above this size

were not coherently internalized. Further, they reported a reduced efficacy in uptake with increasing microsphere size, and particles around 50 nm displayed the optimal size for cellular internalization (100), which also is reported by others (93, 95). These findings are promising for the glycogen nanoprobe, and can be seen in line with our observations from fluorescence microscopy.

When comparing unlabeled cell samples with cells labeled with varying doses of the nanoprobe in Figures 4.1-4.3, no distinct morphological or behavioral alterations were observed. Single Melmet 1 pGF1 cells appeared as more independent than the other two cell lines, and a broad lamellipodium was noted for both labeled and unlabeled cells. Melmet 5 pGF1 cells displayed a star-like morphology with demarked filopodia in bright field micrographs both when labeled, and when used as negative controls. The growth pattern of this cell line occurred in patches, for labeled as well as unlabeled cells. H1_DL2 cells demonstrated elongated filopodia, similarly as what was seen for the Melmet 5 pGF1 cells. The relatively low proliferation rate for H1_DL2 cells compared to the other two cell lines remained the same for labeled as well as unlabeled cells. Multinucleated cells were occasionally observed for Melmet 5 pGF1 and H1_DL2, both for labeled and unlabeled cells. According to Weihua and colleagues, such larger, multinucleated cells are commonly found in established tumor cell lines (104). They often result from lack of cytokinesis following mitosis and provide an example of an irregular cancer cell phenotype associated with malignancy. The morphology and behavior of cultured cells thus remained the same for both labeled and unlabeled samples, indicating adequate short-term cell viability *in vitro*.

Based on HTI experiments (Figures 4.6-4.9) and the cell viability after labeling with varying amounts of the glycogen nanoprobe (Figure 4.11-4.13 and 4.18-4.20), a dose of 200 μg/mL was chosen with incubation time 24 hours. As stated in Chapter 4.2, the nanoprobe doses were increased in HTI experiments from those used in the pilot project due to the low fluorescence intensity, as we had to use high gain and exposure time for detection. When bearing in mind that 100 μg/mL as used in the pilot project was considered a too low dose, this was used for comparison of higher doses (200-400 μg/mL) in HTI.

With respect to incubation time, we established already in the pilot project that increased incubation times with the nanoprobe had major impact on cellular fluorescence intensity. To investigate this while using higher nanoprobe doses in the HTI experiment, we chose to

include further titrations of this with two and four hours as well. As expected, we did not obtain an adequate fluorescence signal, which further suggests that longer incubation times are advantageous. From Figure 4.11 we observed a decreased viability for Melmet 1 pGF1 cells incubated with the nanoprobe more than 48 hours, which indicated that incubation times longer than this were unfavourable. Despite the fact that Melmet 5 pGF1 cells displayed decreased viability after 24 hours of incubation with the nanoprobe (Figure 4.12), this was only to a small degree emphasized, as subsequent measurements contradicted this. Thus, as all fluorescence intensity measurements after 24 hours of incubation with the nanoprobe were considerable higher than two to six hours as seen in Figures 4.7-4.9, we concluded that this was sufficient and that healthy cell samples were maintained.

Regarding nanoprobe dose, it was noted that for two of the three cell lines studied, i.e. Melmet 1 pGF1 and Melmet 5 pGF1, increasing the dose from 200 μg/mL to 300 μg/mL did not result in a significant increase in fluorescence signal as seen in Figures 4.7 and 4.8. It is relatively accessible to manipulate the microscope settings to improve fluorescent contrast by adjusting exposure parameters such as gain and exposure time. On MRI on the other hand, there are less opportunities to adjust T_1 weighted image sequences to improve the T_1 effects. However, it is known from the publication by Filippov that the wt% of Gd is higher than that of Dyo-615 in the probe, at 3.19 and 0.33, respectively (63). This indicates that it should be easier to obtain contrast agent-effects on MRI compared to fluorescence microscopy using the same dose. Also, we endeavored not to overload the cells with too large amounts of the nanoprobe, exemplified by 400 μg/mL, as we considered lower doses less harmful. With this in mind, it was not regarded necessary to increase the nanoprobe dose beyond 200 μg/mL, thus a dose at 200 μg/mL for 24 hours thus seemed appropriate for *in vitro* samples for both modalities.

All three cell lines used during the project displayed a clear fluorescence signal after labeling. Still, some individual variations were observed through the pilot project (Figures 4.1-4.3), HTI experiments (Figures 4.7-4.9) and assessments of fluorescence duration after labeling (Figures 4.16-4.17). Although the fluorescence measurements from the HTI experiments are not directly comparable to measurements on micrographs captured with the Nikon TE2000 microscope, a common intercellular pattern was observed: Predominantly, H1_DL2 cells displayed the highest signal, Melmet 5 pGF1 in between and Melmet 1 pGF1 the lowest signal. This pattern, which was found through manual fluorescence measurements in the pilot

project, and through an automatic processing pipeline in CellProfiler, suggests reliable cellular fluorescence data, independent on the approach used. Rima and colleagues demonstrated diverse degrees of cellular internalization efficacy of a Gd-based nanoparticle into a larynx cancer cell line, a glioblastoma cell line and healthy T lymphocytes (90). This was attributed to varying membrane permeability for the individual cell lines. Further, Wilhelm and colleagues reported on varying internalization capacities of different cell lines, which affected the total cellular uptake (105). These aspects were not studied in detail within this project, however the tendencies between the different cell lines seen in our fluorescence experiments might be due to individual variations in permeability properties and ability for internalization, as the Melmet 1 pGF1 cell line exhibited a lower permeability and/or potential than the other two cell lines. Nevertheless, as individual cell lines have different properties as described above, such variations should to a certain degree be expected. The magnitude of this aspect was not considerable high and thus not emphasized any further.

After determining the appropriate labeling dose, the cell lines were individually studied with fluorescence microscopy to investigate nanoprobe clearance. Nanomaterial clearance is according to Naahidi and colleagues determined by a combination of size, hydrophobicity and electrical charge of the probe (94). We observed a gradual decrease in fluorescent signal in our experiments over five days (Figures 4.16-4.17). It was observed that the proliferation rates shown in Figures 4.18-4.20 could be correlated to the fluorescent signal. The H1_DL2 cells proliferated slower than the other two cell lines. This particular cell line also displayed the highest fluorescence signal. Melmet 5 pGF1 on the other hand, which has the highest proliferation rate, showed a relatively quick drop in fluorescence intensity after the first imaging (Figure 4.16 G). Ambrozek-Latecka and colleagues described how appropriate fluorescent assays can realistically indicate cell proliferation in culture, as the signal was reduced with increased cell division (106). Also, it should be stated that our experiment was not specifically customized to capture proliferating cells in culture. Ambrozek-Lateckas findings are partly in accordance with our findings, however there was an exception to this association for Melmet 1 pGF1 cells: From the first to the second time point, Melmet 1 pGF1 cells demonstrated an increase in cellular fluorescence intensity (Figures 4.16 B and 4.17). This could perhaps be due to a slower uptake, possibly as a consequence of the inferior cell membrane permeability or internalization capacity as discussed above. Further, it could result from an artefact within the experiment. As seen after 96 hours, Melmet 5 pGF1 cells showed a more or less complete clearance of fluorescence signal (Figure 4.16 J), whereas remaining

signal was detected in Melmet 1 pGF1 and H1_DL2 samples (Figure 4.16 E and O). Thus, a complete clearance would likely have been observed in these two cell lines by increasing the time aspect for the particular study. This is regarded a favorable feature of nanomaterials after the introduction into the body and completion of its intended purpose and performance (94).

The micrographs acquired of metastatic melanoma cells cultured in 3D, showed the presence of fluorescence signal within central areas of cellular clusters or colonies after 14 days in soft agar culture (Figure 4.21). Under these conditions, several micro-environmental factors changed as described in Chapter 1.3.1. Because the altered growth environment contributes to a spatially impeded cell spreading and proliferation as reported by Baker and colleagues, many cellular processes, such as proliferation, are substantially decelerated in 3D cultures. Cells in such environments are thus forced to mediate or cleave the physical scaffold they are situated in (48). Consequently, the prolonged fluorescence duration discovered in this assay is in accordance with this. The micrographs of Melmet 5 pGF1 and H1_DL2 cells demonstrated colonies rather than clusters, as seen for Melmet 1 pGF1. This suggested that Melmet 5 pGF1 and H1_DL2 proliferation had occurred and aggregated on the outside of colonies due to the observation of central areas of fluorescence signal. In general, it was a challenge to acquire adequate in-focus micrographs because cells in 3D cultures form ellipsoid morphologies, in the scale of 10 to 30 μm (107), as opposed to a few μm when cells are cultured in monolayer (108). Thus, on the microscope the exposure time was shortened and the gain increased to facilitate the acquisition of the fluorescence. Melmet 5 pGF1 was in particular difficult to image, as these cells to a larger extent migrated and proliferated in all three dimensions compared to Melmet 1 pGF1 and H1_DL2 cells. Pampaloni and colleagues acquired the micrographs of such cellular spheroids using stack methods in light, electron and multiphoton microscopy, which can be considered a better method than ours (107). Bilgin and colleagues describe a curvature-based partitioning image processing pipeline with segmentation and subsequent profiling to quantify cells in 3D culture. The purpose of their description was to study biomarkers, potential therapeutic targets and atypical signaling pathways (108). Our goal was only to examine the presence of fluorescent signal after an elevated period of prelabeled cells in 3D culture, for which reason no further analysis was done. The fact that fluorescence signal was observed within some cells of all three cell lines after 14 days in 3D culture is promising for further *in vivo* use of the nanoprobe. It is known that not all cancer cell lines have the ability to form colonies or spheroids when grown in 3D cultures (109). Prasmickaite and colleagues reported on the formation of spheroids as well as colonies for

Melmet 1 and Melmet 5 cells (82), which is in disagreement with our findings. Our experiment was repeated three times, which should suggest that our observations are reliable. On the other hand, the culture conditions differed, as Prasmickaite provided their cells with specialized stem cell growth conditions (82). Also, the disagreement can be a result of the different terms used to describe cell growth in 3D cultures, such as spheroids, colonies, aggregates and clusters (49, 109-111), as no clear or consistent definitions were found in different papers. It is however important to study cellular behavior by using a multi-layered agar gel approach of intermediate complexity, as a next step from monolayer culture. Several therapeutic agents or probes have previously lost their potential when researchers have transferred them from monolayer to 3D cell cultures. Thus, it is possible to avoid the overuse of animal models exclusively based on results from monolayer (112).

5.2 Cell viability

We have previously shown linearity between fluorescence signal and cell proliferation when using the resazurin assay with signal detection after four hours (unpublished data). The proliferation of Melmet 5 pGF1 and H1_DL2 cells was minimally affected by labeling the cells with 200 μg/mL of the nanoprobe as seen by the resazurin assay (Figures 4.12 and 4.13), however with two exceptions: The first exception is Melmet 5 pGF1 cells incubated with 200 μg/mL glycogen nanoprobe for 24 hours prior to resazurin measurements, in which lower numbers were found compared to negative control cells. This indicated reduced cell viability at this particular read-out. When seen in correlation with the proliferation study in Chapter 4.6.1, there is a consistency with the number of dead Melmet 5 pGF1 cells found at time point 0, which is the corresponding time. However successive measurements contradict with this, as this trend leveled off after elevated incubation times with the nanoprobe. Further, as seen from Figure 4.13, labeled H1_DL2 cells did in general transform an equal amount of resazurin as seen for negative control samples, until 120 hours of incubation. The proliferation study did not extend over that time period for comparison, however the resazurin measurements indicated cytotoxic effects or reduced cell proliferation at this time.

Melmet 1 pGF1 cells, showed a reduced capacity to transform resazurin to resorufin after being exposed to the nanoprobe for 72 to 120 hours (Figure 4.11). It seemed that all nanoprobe doses above 200 μg/mL impaired cell proliferation for this particular cell line. The same tendency can also be seen from the proliferation study (Figure 4.18), as labeled cells

tended to proliferate less than unlabeled.

According to Filippov and colleagues, any cells incubated with the glycogen nanoprobe are likely to treat the added glycogen as their own (63). Thus, it seemed that Melmet 1 pGF1 cells did not tolerate this as well as the other two cell lines at elevated incubation times in monolayer *in vitro*. All cells were checked well by well at each time point to confirm the presence of live cells. The reduced RFUs detected for the cell lines at varying incubation times were thus not necessarily a result from visually observed cell death, but can likely be due to decreased cell proliferation. The magnitude of cytotoxic effects of Gd chelates is debated (113, 114), but can be a contributing factor to cell viability. This aspect was not studied further within this project.

When comparing the numbers obtained during resazurin experiments with the proliferation study, our findings suggest that the former is more sensitive. Although counting cells is a very direct way to monitor cell proliferation, the estimates are based on small extractions of cell solution from an in comparison large volume with cells. The measurements of fluorescence units in the resazurin assay is in contrast based on individual cells contribution to a total number in relative entities. In conclusion, adequate short-term cell viability after labeling with 200 μg/mL of the nanoprobe was found for all cell lines.

5.3 Cellular migration

Due to technical problems with the imaging equipment used to capture cellular wound healing in monolayer, data was only acquired on one of the three cell lines used throughout this project, namely Melmet 1 pGF1. As demonstrated in Figure 4.15, there was a tendency that labeled cells migrated more slowly than unlabeled cells, however this was not statistically significant. This is in line with other studies, showing no or minimal effect after cell labeling (21). Monolayer migration studies have previously demonstrated to be quite useful, as these to some extent mimic a real *in vivo* situation as described by Haudenschild and colleagues (115).

Preliminary migration data, which included all three cell lines (data not shown), demonstrated that the wound was closed for all samples after 60 hours. This is also in consistence with Liangs wound healing protocol (116). For Melmet 1 pGF1 on the other hand, the wound was

healed already 14 hours after start of the experiment. According to Nygaard and colleagues (117), the considered cell line is despite lower proliferation rate than Melmet 5, a highly invasive cell line due to expression of a genetic signature associated with an invasive phenotype (117). The same authors have found genetic signatures in Melmet 5 cells that are in accordance with a more aggressive proliferation pattern, but lack the invasiveness detected for Melmet 1 cells. This explains the rapid migration detected for Melmet 1 pGF1 cells.

5.4 MRI experiments

Gd has several unpaired electrons and is, when chelated, characterized as a paramagnetic contrast agent. Major magnetic moments are consequently produced through reduced T_1 relaxation constants in areas of contrast agent enhancement as illustrated in Figure 1.6 A. T_2 relaxation is also reduced, however, only to some extent and it is an accepted certainty that Gd is an established T_1 agent. Thus, it was of interest to study T_1 relaxation to demonstrate whether the nanoprobe had functionality in MRI, and consequently T_2 measurements were neglected. The motivation for measuring relaxation constants is that this is a more reliable marker for tissue properties compared to signal intensities based on MR images (118). A point of reference is homogenous image contents and high spatial resolution. This was attempted by providing evenly dispersed cells in phantoms and by using T_2-weighted images to select a superior axial slice to map, i.e. without air pockets.

A search for more suitable materials for T_1 MRI phantoms in addition to or as a supplement to agar seems to be the concern in several research articles (71, 73, 119, 120). According to Yoshimura and colleagues, our agar concentration at 2 % is within the range that mimics biological relaxation times (73). As stated by Hellerbach, this corresponds to a T_1 value at 2 214.27 (±23.93) ms, which they argue cannot be obtained using pure agar nor agarose phantoms (71). Our T_1 measurements of phantom I (Table 5, Chapter 4.9.1) was somewhat higher than the value recommended by Hellerbach. When linking these numbers to measured relaxation times for phantom IV and V, we can conclude that it might have been advantageous to achieve lower T_1 constants. This can in theory be accomplished by increasing the concentration of agar in the stock solution, as less water will result in shorter T_1 times. Nevertheless, we concluded that the T_1 value of phantom I was at an acceptable level to perform T_1 relaxation experiments with nanoprobe labeled cells (2 375 ± 66.99 ms). Tissue relaxation constants are, however, influenced by additional and intricate factors. As described

by Petrén-Mallmin and colleagues, the performance of the scanner and the choice of image acquisition sequence can result in varying relaxation constants, which were as far as possible kept constant during our experiments. Also, for most tissue types, T_1 constants increase with elevated temperatures (121). Consequently, if the temperature is altered by only one degree Celsius, relaxation times can be detected with an error at 1-3 % (122). The phantoms were therefore kept at room temperature for 30 minutes before scanning, in order to stabilize the temperature of the phantoms to room temperature (~20° C).

Control phantom IV and II displayed quite similar relaxation properties, with similar T_1 values as reported by Rooney and colleagues, measuring T_1 values in blood (2 587 ±283 ms) (123). Phantom III was used to demonstrate T_1 effects after adding the glycogen nanoprobe to agar. As the T_1 value of this phantom was measured to be 55 % lower than negative control phantoms with unlabeled cells, T_1 reductions could also be expected from labeled cells embedded into the phantoms. Our mean T_1 value for phantoms with unlabeled cells was 2 515.57 ms, i.e. a bit lower than phantom II, and higher than phantom I. This indicates that cells in phantoms slightly increase the T_1 values, with small variations between different cell concentrations (Figures 4.24-4.26).

During *in vitro* MRI scanning of the agar-casted cells described in Table 4, a significantly lower T_1 relaxation value was found for labeled cells down to a cell concentration at 750 cells/μL for Melmet 1 pGF1 (Figure 4.24) and 1 500 cells/μL for Melmet 5 pGF1 (Figure 4.25) and H1_DL2 (Figure 4.26). Because of the opposite effect detected for 250 cells/μL for Melmet 1 pGF1, any reduced T_1 values for lower cell concentrations cannot be ascribed to effects of the nanoprobe. The same was seen for Melmet 5 pGF1 and H1_DL2 at cell concentrations lower than 750 cells/μL. Each phantom was only scanned once, and it can be argued that variations in agar homogeneity, cell numbers or variations in the homogeneity of the magnetic field could be at least partly responsible for the varying T_1 times detected for the lower cell concentrations. Thus, by repeating the scans on additional phantoms with the same cell concentrations, the T_1 values for these phantoms would most likely have leveled out. This was not performed due to time limitations.

According to Terreno and colleagues (124), cells labeled with Gd through pinocytosis, can be detected in MRI phantoms containing ≥5 000 cells/μL. These cells were labeled with $0–5{\cdot}10^{10}$

Gd chelates per cell. Our findings suggests a more efficient cell labeling, as the T_1 effects were observed down to 1 500 cells/μL for all three cell lines investigated. It should be noted however, that we have not studied intracellular amounts of Gd. Terreno and colleagues explained their observed low sensitivity to quenching due to the presence of very high amounts of intracellular Gd. Another study previously performed in our research group on a T_2^* agent in MRI phantoms, showed efficient contrast agent detections down to cell concentrations at 250/μL, which was further validated by *in vivo* experiments (125), indicating a higher sensitivity than found for the glycogen nanoprobe. This is also in accordance with the literature on T_1 and T_2^* contrast agent sensitivity (126, 127).

When comparing the individual T_1 reductions between the different cell lines that we used, it is noted that Melmet 1 pGF1, which displayed the lowest fluorescence intensities when examined by microscopy, showed the highest T_1 changes by MRI. This is opposite to what we expected, as the labeling method was the same for both fluorescence microscopy and MRI. The reason for this variation remains uncertain, however plausible explanations can be altered temperature or pH of the phantom content (71).

A main goal was to obtain data to support the use of the nanoprobe as a tool to detect and possibly treat challenging malignancies, such as multiple brain metastases. As part of a «proof of principle», an *in vivo* pilot project was performed, where a mouse with subcutaneous tumors was scanned by MRI six weeks after injection of tumor cells. BLI was used to study tumor development and progression two and four weeks after subcutaneous injection of tumor cells, respectively. Central areas of necrosis were not observed within the tumors by BLI. However, the histology contradicts with this, as angiogenesis and areas of necrosis were found within the tumors. Thus, uptake of the nanoprobe should have occured to a larger extent in the tumor as well as intestines and muscle tissues as seen in Figure 4.28 for the animal scanned after injection of Omniscan. As T_1 is reduced as a consequence of the use of Gd, T_1 weighted images appear brighter in tissues with contrast enhancement. Therefore, the pixel intensity measurements of tumor tissue demonstrated in Figure 4.29 should to some extent predict effects of Gd, however not as accurately as relaxation mapping of T_1, similar to what was done for *in vitro* MRI. The use of Omniscan resulted in a larger increase in signal intensity after contrast agent administration, than when using the glycogen nanoprobe.

The low T_1 changes induced by the nanoprobe is likely due to lower amounts of Gd in the

concentrations prepared of the nanoprobe, compared to Omniscan. We used the molecular weight of the lanthanide Gd, 157.25 g/mol to calculate the amount of nanoprobe needed to match Omniscan. The active contrast enhancement agent in Omniscan is gadodiamide, which has a molecular weight at 591.672 g/mol (128), i.e. higher amounts of the nanoprobe are needed to achieve corresponding T_1 contrast enhancement. Thus similar contrast enhancement as for Omniscan could likely be achieved by using approximately four times the concentrations of the nanoprobe. We did not have time to pursue these experiments.

As the nanoprobe dose administered to the animals was based on the amounts of Omniscan normally used in the clinic, it was of no concern whether the dose of Gd would be lethal to the animals (LD_{50} = 6-20 mmol/kg). On the other hand, the amount of glycogen administered intravenously was evaluated. According to Glaumann and colleagues research, glycogen injected by this administration route is lethal above 128 mg per 100 g rat (99). The animal studied by MRI during this experiment was given 7.85 mg per 100 g weight, which is far below this threshold. This indicates that the glycogen nanoprobe is safe for *in vivo* use, further underpinned by Filippovs *in vivo* observations of Gds temporal distribution in mice (63). Further, it has been argued that biodegradable probes are preferable (98), of which the considered nanoprobe is an example of. In general it is advised against the use of non-biodegradable nanomaterials, as the accumulations of these materials seen in the liver or spleen might result in toxic effects (94). However, we did not study possible long-term side effects in the tumor-bearing nod/scid mice after injecting the nanoprobe. This matter was not addressed by Filippov either (63), and should therefore be studied in further experiments.

Compared to our results on cellular internalization *in vitro*, the internalization of nanoprobe in tumor tissue (into the tumor cells as well as into the tumor matrix) is more complex in an *in vivo* setting. As glycogen is relatively inactive to amylases, it can be expected that the nanoprobe should survive transportation in the blood stream, and not be directly eliminated as its molecular weight is above renal threshold (63). The nanoprobe thus takes advantage of accumulation in cancerous tissue as the associated blood vessels often are dilated, leaky, defective, have an irregular shape and have wide fenestra due to poorly aligned endothelial cells, a manifestation of the EPR effect (129). Because perivascular cells, basement membrane and smooth muscle layer often is absent, it is subsequently possible that the nanoprobe can internalize into cells once located within the tumor vasculature, or it might diffuse from vasculature and endure in the extravascular extracellular space for several

minutes to hours, as effective drainage is absent. However, cellular internalization *in vivo* is further complicated due to the presence of a higher interstitial fluid pressure inside tumors (130). Thus, the efficient cellular uptake demonstrated for *in vitro* experiments is not directly comparable to an *in vivo* situation.

Normally, Gd-based agents are used as extracellular contrast enhancers, and do not cross cell membranes (122). Recently, it has been reported on the development of Gd nanomaterials for intracellular use (90, 113, 127, 131, 132). If successful, such as reported by Di Corato and colleagues, this can give Gd-based nanomaterials potential as a cellular label for tracking by MRI (132). Unfortunately we were only able to obtain very preliminary data on *in vivo* use of the glycogen nanoprobe. Seen in light with the findings from *in vitro* MRI studies, it is doubtful that we can obtain a very sensitive visualization of single cells by high resolution MRI. The dose of the nanoprobe should still be optimized and studied further, as the cells to a small degree were affected by the labeling, which indicates non-toxic effects. Thus, it should to a higher extent be possible to follow the biodistribution of the nanoprobe and potential therapeutic agents *in vivo*.

5.5 Concluding remarks

Based on the preceding, fundamental *in vitro* data on the use of the novel glycogen nanoprobe is reported in this thesis. Through fluorescence microscopy, a high cellular internalization efficacy was demonstrated with an optimal labeling period at 24 hours. A dose at 200 μg/mL was chosen for verification experiments of the two contrast agents encompassed in the nanoprobe, in which MRI phantoms with labeled cells were scanned.

The viability experiment based on cellular metabolism did in general demonstrate minor changes between labeled and unlabeled cells, which is promising in that the nanoprobe can be used *in vivo*. The experiments on nanoprobe clearance were promising with respect to the EPR effect proposed to occur after administering the nanoprobe into nod/scid mice *in vivo*, as any injected material should be eliminated when its intended use is performed. The results from 3D cell cultures also contributed to promising results with respect to *in vivo* experiments as a next step.

The *in vitro* MRI experiments revealed a lower sensitivity of contrast agent detection than

microscopy experiments. Nevertheless, labeled cell concentrations down to 1 500/μL was detected by T_1 mapping. When the nanoprobe was injected into nod/scid mice, a weak but existing effect of the T_1 agent was observed. Further work should thus be done to optimize the *in vivo* doses due to the good findings reported on *in vitro* cell viability and cellular contrast agent uptake.

Although we only performed experiments on metastatic melanoma cell lines, our experiments showed differences in cellular morphology and general behavior. This suggests that the nanoprobe can be tested for yet other cell lines derived from other tumor tissues. The novel glycogen nanoprobe can thus be concluded as effective for *in vitro* use on metastatic melanoma cell lines, and shows great promise to be studied further as a theranostic unit.

5.6 Future perspectives

Several of the experiments should be repeated or supplemented to delineate in detail the effects of labeling with the glycogen nanoprobe. The fact that data on only one cell line was acquired during the migration assay, is a potential drawback as this experiment was used to predict altered cellular migration as a consequence of labeling with the nanoprobe. We are currently planning to repeat this experiment including all three cell lines. This can can be important for the usability of the nanoprobe, as *in vitro* monolayer wound healing assays to some extent mimics a real *in vivo* situation. Further, additional MRI phantoms with labeled cells should be prepared using the same method and scanned to obtain more robust data on this experiment.

We are currently testing further organelle markers to determine the subcellular localization of the nanoprobe. The results were not ready to be inclded in this thesis. Markers tested were ER, Golgi apparatus, lysosomes, plasma membrane and endosomes.

The nanoprobe should also be tested on other cancer cell lines *in vitro* besides metastatic melanoma to study whether the results are similar. We are also planning to test the nanoprobe on healthy endothelial cells for comparison.

The doses of glycogen nanoprobe for *in vivo* use should be optimized to match the effects of Omniscan due to the promising data obtained during *in vitro* experiments. Also, of all current

nano-sized materials in biomedical research, units with theranostic potential have been proposed to be of higher value, such as described by Wang and colleagues for instance (78). After optimizing the nanoprobe doses for *in vivo* use, it should be implemented in other animal tumor models besides subcutaneous ones to better study its detection of for instance brain tumors. If these studies are successful, it is further possible to attach fludeoxyglucose (FDG) to the nanoprobe (a glucose analogue) for nuclear medicine approaches, and also pharmaceuticals for theranostic use.

References

1. Fenouille N, Tichet M, Dufies M, Pottier A, Mogha A, Soo JK, et al. The epithelial-mesenchymal transition (EMT) regulatory factor SLUG (SNAI2) is a downstream target of SPARC and AKT in promoting melanoma cell invasion. PloS one. 2012;7(7):e40378. PubMed PMID: 22911700. Pubmed Central PMCID: 3401237.

2. GLOBOCAN 2012 v1.0, Cancer Incidence and Mortality Worldwide: IARC CancerBase [Internet]. 2013. Available from: http://globocan.iarc.fr.

3. Erdmann F, Lortet-Tieulent J, Schuz J, Zeeb H, Greinert R, Breitbart EW, et al. International trends in the incidence of malignant melanoma 1953-2008--are recent generations at higher or lower risk? International journal of cancer Journal international du cancer. 2013 Jan 15;132(2):385-400. PubMed PMID: 22532371.

4. Dunki-Jacobs EM, Callender GG, McMasters KM. Current management of melanoma. Current problems in surgery. 2013 Aug;50(8):351-82. PubMed PMID: 23849560.

5. Aladowicz E, Ferro L, Vitali GC, Venditti E, Fornasari L, Lanfrancone L. Molecular networks in melanoma invasion and metastasis. Future oncology. 2013 May;9(5):713-26. PubMed PMID: 23647299.

6. Tryggvadottir L, Gislum M, Hakulinen T, Klint A, Engholm G, Storm HH, et al. Trends in the survival of patients diagnosed with malignant melanoma of the skin in the Nordic countries 1964-2003 followed up to the end of 2006. Acta oncologica. 2010 Jun;49(5):665-72. PubMed PMID: 20491525.

7. Jemal A, Bray F, Center MM, Ferlay J, Ward E, Forman D. Global cancer statistics. CA: a cancer journal for clinicians. 2011 Mar-Apr;61(2):69-90. PubMed PMID: 21296855.

8. Norway CRo. Cancer Registry of Norway. Cancer in Norway 2009 - Cancer incidence, mortality, survival and prevalence in Norway. . Cancer Registry of Norway. 2011.

9. Ershler WB. The Influence of an Aging Immune System on Cancer Incidence and Progression. Journal of Gerontology: BIOLOGICAL SCIENCES 1993, Vol 48, No 1B3-B7. 1993;48(1):B2-B7.

10. Finkel T, Serrano M, Blasco MA. The common biology of cancer and ageing. Nature. 2007 Aug 16;448(7155):767-74. PubMed PMID: 17700693.

11. DeLuca AM, Srinivas A, Alani RM. BRAF kinase in melanoma development and progression. Expert reviews in molecular medicine. 2008;10:e6. PubMed PMID: 18279546.

12. Guerry Dt, Synnestvedt M, Elder DE, Schultz D. Lessons from tumor progression: the invasive radial growth phase of melanoma is common, incapable of metastasis, and

indolent. The Journal of investigative dermatology. 1993 Mar;100(3):342S-5S. PubMed PMID: 8440920.

13. Clark WH, Jr., Elder DE, Guerry Dt, Braitman LE, Trock BJ, Schultz D, et al. Model predicting survival in stage I melanoma based on tumor progression. Journal of the National Cancer Institute. 1989 Dec 20;81(24):1893-904. PubMed PMID: 2593166.

14. Shtivelman E, Flaherty KT, Fisher DE. A Melanoma Molecular Disease Model. PLoS ONE 6(3): e18257 doi:101371/journalpone0018257. 2011;6(3).

15. Schramm SJ, Campain AE, Scolyer RA, Yang YH, Mann GJ. Review and cross-validation of gene expression signatures and melanoma prognosis. The Journal of investigative dermatology. 2012 Feb;132(2):274-83. PubMed PMID: 21956122.

16. Lahortiga I, Cox L. Somersault 1824 2014. Available from: http://www.somersault1824.com/.

17. Research AAfC. The Ubiquitin-Proteasome System Meets Angiogenesis. Molecular Cancer Therapeutics. 2012;11(3):538-48. Epub February 21.

18. Breslow A. Thickness, cross-sectional areas and depth of invasion in the prognosis of cutaneous melanoma. Annals of surgery. 1970 Nov;172(5):902-8. PubMed PMID: 5477666. Pubmed Central PMCID: 1397358.

19. Davies MA, Liu P, McIntyre S, Kim KB, Papadopoulos N, Hwu WJ, et al. Prognostic factors for survival in melanoma patients with brain metastases. Cancer. 2011 Apr 15;117(8):1687-96. PubMed PMID: 20960525.

20. Fife KM, Colman MH, Stevens GN, Firth IC, Moon D, Shannon KF, et al. Determinants of outcome in melanoma patients with cerebral metastases. Journal of clinical oncology : official journal of the American Society of Clinical Oncology. 2004 Apr 1;22(7):1293-300. PubMed PMID: 15051777.

21. Sundstrøm T, Daphu I, Wendelbo I, Hodneland E, Lundervold A, Immervoll H, et al. Automated tracking of nanoparticle-labeled melanoma cells improves the predictive power of a brain metastasis model. Cancer research. 2013 Apr 15;73(8):2445-56. PubMed PMID: 23423977.

22. Flanigan JC, Jilaveanu LB, Chiang VL, Kluger HM. Advances in therapy for melanoma brain metastases. Clinics in dermatology. 2013 May-Jun;31(3):264-81. PubMed PMID: 23608446.

23. Miller D, Zappala V, El Hindy N, Livingstone E, Schadendorf D, Sure U, et al. Intracerebral metastases of malignant melanoma and their recurrences-A clinical analysis. Clinical neurology and neurosurgery. 2013 Apr 30. PubMed PMID: 23643143.

24. Daphu I, Sundstrom T, Horn S, Huszthy PC, Niclou SP, Sakariassen PO, et al. In vivo animal models for studying brain metastasis: value and limitations. Clinical & experimental metastasis. 2013 Jun;30(5):695-710. PubMed PMID: 23322381.

25. Geiger TR, Peeper DS. Metastasis mechanisms. Biochimica et biophysica acta. 2009 Dec;1796(2):293-308. PubMed PMID: 19683560.

26. Dome B, Paku S, Somlai B, Timar J. Vascularization of cutaneous melanoma involves vessel co-option and has clinical significance. The Journal of pathology. 2002 Jul;197(3):355-62. PubMed PMID: 12115882.

27. Carbonell WS, Ansorge O, Sibson N, Muschel R. The vascular basement membrane as "soil" in brain metastasis. PloS one. 2009;4(6):e5857. PubMed PMID: 19516901. Pubmed Central PMCID: 2689678.

28. Eichler AF, Chung E, Kodack DP, Loeffler JS, Fukumura D, Jain RK. The biology of brain metastases-translation to new therapies. Nature reviews Clinical oncology. 2011 Jun;8(6):344-56. PubMed PMID: 21487419. Pubmed Central PMCID: 3259742.

29. Pomyje J, Zivny JH, Stopka T, Simak J, Vankova H, Necas E. Angiopoietin-1, angiopoietin-2 and Tie-2 in tumour and non-tumour tissues during growth of experimental melanoma. Melanoma Res. 2001 Dec;11(6):639-43. PubMed PMID: 11725211.

30. Li G, Satyamoorthy K, Meier F, Berking C, Bogenrieder T, Herlyn M. Function and regulation of melanoma-stromal fibroblast interactions: when seeds meet soil. Oncogene. 2003 May 19;22(20):3162-71. PubMed PMID: 12789292.

31. Brezillon S, Radwanska A, Zeltz C, Malkowski A, Ploton D, Bobichon H, et al. Lumican core protein inhibits melanoma cell migration via alterations of focal adhesion complexes. Cancer letters. 2009 Sep 28;283(1):92-100. PubMed PMID: 19394140.

32. Schmidt A, Hall MN. Signaling to the actin cytoskeleton. Annual review of cell and developmental biology. 1998;14:305-38. PubMed PMID: 9891786.

33. Damsky WE, Rosenbaum LE, Bosenberg M. Decoding melanoma metastasis. Cancers. 2010;3(1):126-63. PubMed PMID: 24212610.

34. Wilhelm I, Molnar J, Fazakas C, Hasko J, Krizbai IA. Role of the blood-brain barrier in the formation of brain metastases. International journal of molecular sciences. 2013;14(1):1383-411. PubMed PMID: 23344048. Pubmed Central PMCID: 3565326.

35. Oskarsson T, Batlle E, Massague J. Metastatic Stem Cells: Sources, Niches, and Vital Pathways. Cell stem cell. 2014 Mar 6;14(3):306-21. PubMed PMID: 24607405.

36. Rahmathulla G, Toms SA, Weil RJ. The molecular biology of brain metastasis. Journal of oncology. 2012;2012:723541. PubMed PMID: 22481931. Pubmed Central PMCID: 3317231.

37. Valiente M, Obenauf AC, Jin X, Chen Q, Zhang XH, Lee DJ, et al. Serpins promote cancer cell survival and vascular co-option in brain metastasis. Cell. 2014 Feb 27;156(5):1002-16. PubMed PMID: 24581498.

38. Schafer MK, Altevogt P. L1CAM malfunction in the nervous system and human carcinomas. Cellular and molecular life sciences : CMLS. 2010 Jul;67(14):2425-37. PubMed PMID: 20237819.

39. Tsuchida A, Okajima T, Furukawa K, Ando T, Ishida H, Yoshida A, et al. Synthesis of disialyl Lewis a (Le(a)) structure in colon cancer cell lines by a sialyltransferase, ST6GalNAc VI, responsible for the synthesis of alpha-series gangliosides. The Journal of biological chemistry. 2003 Jun 20;278(25):22787-94. PubMed PMID: 12668675.

40. Bos PD, Zhang XH, Nadal C, Shu W, Gomis RR, Nguyen DX, et al. Genes that mediate breast cancer metastasis to the brain. Nature. 2009 Jun 18;459(7249):1005-9. PubMed PMID: 19421193. Pubmed Central PMCID: 2698953.

41. Fidler IJ. The pathogenesis of cancer metastasis: the 'seed and soil' hypothesis revisited. Nature reviews Cancer. 2003 Jun;3(6):453-8. PubMed PMID: 12778135.

42. Zbytek B, Carlson JA, Granese J, Ross J, Mihm MC, Jr., Slominski A. Current concepts of metastasis in melanoma. Expert review of dermatology. 2008 Oct;3(5):569-85. PubMed PMID: 19649148. Pubmed Central PMCID: 2601641.

43. Kimlin LC, Casagrande G, Virador VM. In vitro three-dimensional (3D) models in cancer research: an update. Molecular carcinogenesis. 2013 Mar;52(3):167-82. PubMed PMID: 22162252.

44. Infanger DW, Lynch ME, Fischbach C. Engineered culture models for studies of tumor-microenvironment interactions. Annual review of biomedical engineering. 2013;15:29-53. PubMed PMID: 23642249.

45. Wang F, Weaver VM, Petersen OW, Larabell CA, Dedhar S, Briand P, et al. Reciprocal interactions between beta1-integrin and epidermal growth factor receptor in three-dimensional basement membrane breast cultures: a different perspective in epithelial biology. Proceedings of the National Academy of Sciences of the United States of America. 1998 Dec 8;95(25):14821-6. PubMed PMID: 9843973. Pubmed Central PMCID: 24533.

46. Rhodes NP, Srivastava JK, Smith RF, Longinotti C. Metabolic and histological analysis of mesenchymal stem cells grown in 3-D hyaluronan-based scaffolds. Journal of materials science Materials in medicine. 2004 Apr;15(4):391-5. PubMed PMID: 15332605.

47. Kenny PA, Lee GY, Myers CA, Neve RM, Semeiks JR, Spellman PT, et al. The morphologies of breast cancer cell lines in three-dimensional assays correlate with their profiles of gene expression. Molecular oncology. 2007 Jun;1(1):84-96. PubMed PMID: 18516279. Pubmed Central PMCID: 2391005.

48. Baker BM, Chen CS. Deconstructing the third dimension: how 3D culture microenvironments alter cellular cues. J Cell Sci. 2012 Jul 1;125(Pt 13):3015-24. PubMed PMID: 22797912. Pubmed Central PMCID: 3434846.

49. Kawaguchi N, Machida M, Hatta K, Nakanishi T, Takagaki Y. Cell shape and cardiosphere differentiation: a revelation by proteomic profiling. Biochemistry

research international. 2013;2013:730874. PubMed PMID: 24073335. Pubmed Central PMCID: 3773893.

50. Morton CL, Houghton PJ. Establishment of human tumor xenografts in immunodeficient mice. Nature protocols. 2007;2(2):247-50. PubMed PMID: 17406581.

51. Bosma MJ, Carroll AM. The SCID mouse mutant: definition, characterization, and potential uses. Annual review of immunology. 1991;9:323-50. PubMed PMID: 1910681.

52. Wang J, Daphu I, Pedersen PH, Miletic H, Hovland R, Mork S, et al. A novel brain metastases model developed in immunodeficient rats closely mimics the growth of metastatic brain tumours in patients. Neuropathology and applied neurobiology. 2011 Feb;37(2):189-205. PubMed PMID: 20819169.

53. Pugsley EV-AaMK. An Overview of Colorimetric Assay Methods Used to Assess Survival or Proliferation of Mammalian Cells. Proc West Pharmacol Soc 54: 10-14. 2011 June 2 2011;54:10-4.

54. Anoopkumar-Dukie S, Carey JB, Conere T, O'Sullivan E, van Pelt FN, Allshire A. Resazurin assay of radiation response in cultured cells. The British journal of radiology. 2005 Oct;78(934):945-7. PubMed PMID: 16177019.

55. John O'Brien IW, Terry Orton and Francois Pognan. Investigation of the Alamar Blue (resazurin) fluorescent dye for the assessment of mammalian cell cytotoxicity. Eur J Biochem. 2000 (267):6.

56. Al-Nasiry S, Geusens N, Hanssens M, Luyten C, Pijnenborg R. The use of Alamar Blue assay for quantitative analysis of viability, migration and invasion of choriocarcinoma cells. Human reproduction. 2007 May;22(5):1304-9. PubMed PMID: 17307808.

57. Hai-xia Zhang G-hD, Jun-tian Zhang. Assay of mitochondrial functions by resazurin in vitro. Acta Pharmacologica Sinica Chinese Pharmacological Society. 2004 March 25 2004.

58. R.J. Gonzalez JBT. Evaluation of hepatic subcellular fractions for Alamar blue and MTT reductase activity. Toxicology in Vitro 15. 2001 (15):3.

59. Hayat MA. Cancer Imaging: Instrumentation and Applications. 30 Corporate Drive, Suite 400, Burlington, MA, USA. 84 Theobald´s Road, London, UK.: Elsevier Academic Press; 2008. 733 p.

60. Society AC. The History of Cancer [Information]. American Cancer Society; 2014. Available from: http://www.cancer.org/cancer/cancerbasics/thehistoryofcancer/index?sitearea.

61. (editor) LM. Timeline: Milestones in Cancer Treatment. cure. 2008 October 2 2008. Epub October 2.

62. Barreto JA, O'Malley W, Kubeil M, Graham B, Stephan H, Spiccia L. Nanomaterials: applications in cancer imaging and therapy. Adv Mater. 2011 Mar 25;23(12):H18-40. PubMed PMID: 21433100.

63. Filippov SK, Sedlacek O, Bogomolova A, Vetrik M, Jirak D, Kovar J, et al. Glycogen as a biodegradable construction nanomaterial for in vivo use. Macromolecular bioscience. 2012 Dec;12(12):1731-8. PubMed PMID: 23169686.

64. Ishikawa-Ankerhold HC, Ankerhold R, Drummen GP. Advanced fluorescence microscopy techniques--FRAP, FLIP, FLAP, FRET and FLIM. Molecules. 2012;17(4):4047-132. PubMed PMID: 22469598.

65. Zanella F, Lorens JB, Link W. High content screening: seeing is believing. Trends in biotechnology. 2010 May;28(5):237-45. PubMed PMID: 20346526.

66. Nwaneshiudu A, Kuschal C, Sakamoto FH, Anderson RR, Schwarzenberger K, Young RC. Introduction to confocal microscopy. The Journal of investigative dermatology. 2012 Dec;132(12):e3. PubMed PMID: 23187113.

67. Giuliano KA. High-Content Screening: A New Approach to Easing Key Bottlenecks in the Drug Discovery Process. Journal of Biomolecular Screening. 1997;2(4):249-59.

68. Currie S, Hoggard N, Craven IJ, Hadjivassiliou M, Wilkinson ID. Understanding MRI: basic MR physics for physicians. Postgraduate medical journal. 2013 Apr;89(1050):209-23. PubMed PMID: 23223777.

69. Pooley RA. AAPM/RSNA Physics Tutorial for Residents - Fundamental Physics of MR Imaging. RadioGraphics. 2005;25:1087-99. Epub April 25 2005.

70. Bjørnerud A. The Physics of Magnetic Resonance Imaging. FYS-KJM 4740. Department of Physics, University of Oslo: University of Oslo; 2006. p. 129.

71. Hellerbach A, Schuster V, Jansen A, Sommer J. MRI phantoms - are there alternatives to agar? PloS one. 2013;8(8):e70343. PubMed PMID: 23940563. Pubmed Central PMCID: 3734012.

72. Kraft KA, Fatouros PP, Clarke GD, Kishore PR. An MRI phantom material for quantitative relaxometry. Magnetic resonance in medicine : official journal of the Society of Magnetic Resonance in Medicine / Society of Magnetic Resonance in Medicine. 1987 Dec;5(6):555-62. PubMed PMID: 3437816.

73. Yoshimura K, Kato H, Kuroda M, Yoshida A, Hanamoto K, Tanaka A, et al. Development of a tissue-equivalent MRI phantom using carrageenan gel. Magnetic resonance in medicine : official journal of the Society of Magnetic Resonance in Medicine / Society of Magnetic Resonance in Medicine. 2003 Nov;50(5):1011-7. PubMed PMID: 14587012.

74. Lee DE, Koo H, Sun IC, Ryu JH, Kim K, Kwon IC. Multifunctional nanoparticles for multimodal imaging and theragnosis. Chemical Society reviews. 2012 Apr 7;41(7):2656-72. PubMed PMID: 22189429.

75. Moghimi SM, Hunter AC, Murray JC. Nanomedicine: current status and future prospects. FASEB journal : official publication of the Federation of American Societies for Experimental Biology. 2005 Mar;19(3):311-30. PubMed PMID: 15746175.

76. Riehemann K, Schneider SW, Luger TA, Godin B, Ferrari M, Fuchs H. Nanomedicine--challenge and perspectives. Angewandte Chemie. 2009;48(5):872-97. PubMed PMID: 19142939.

77. Chen Y-C, Huang X-C, Luo Y-L, Chang Y-C, Hsieh Y-Z, Hsu H-Y. Non-metallic nanomaterials in cancer theranostics: a review of silica- and carbon-based drug delivery systems. Science and Technology of Advanced Materials. 2013;14(4):044407.

78. Wang M, Thanou M. Targeting nanoparticles to cancer. Pharmacological research : the official journal of the Italian Pharmacological Society. 2010 Aug;62(2):90-9. PubMed PMID: 20380880.

79. Zhou Z, Lu ZR. Gadolinium-based contrast agents for magnetic resonance cancer imaging. Wiley interdisciplinary reviews Nanomedicine and nanobiotechnology. 2013 Jan-Feb;5(1):1-18. PubMed PMID: 23047730. Pubmed Central PMCID: 3552562.

80. Hagberg GE, Scheffler K. Effect of r(1) and r(2) relaxivity of gadolinium-based contrast agents on the T(1)-weighted MR signal at increasing magnetic field strengths. Contrast media & molecular imaging. 2013 Nov-Dec;8(6):456-65. PubMed PMID: 24375901.

81. Czerney P. Dyomics - Colours for Life. Fluorescent Dyes for Bioanalytical and Hightech Applications 7th ed2011. p. 84.

82. Prasmickaite L, Skrbo N, Hoifodt HK, Suo Z, Engebraten O, Gullestad HP, et al. Human malignant melanoma harbours a large fraction of highly clonogenic cells that do not express markers associated with cancer stem cells. Pigment cell & melanoma research. 2010 Jun;23(3):449-51. PubMed PMID: 20236249.

83. Miller L. Quantifying Color Intensity [Protocol]. Dalton Cardiovascular Research Center; 2007 [updated June 21 2011; cited 2007]. Available from: https://support.dalton.missouri.edu/index.php/wiki/Public:Quantifying_Color_Intensity/.

84. Schindelin J, Arganda-Carreras I, Frise E, Kaynig V, Longair M, Pietzsch T, et al. Fiji: an open-source platform for biological-image analysis. Nature Methods. 2012;9(7):676-82.

85. Campos S, Davey P, Hird A, Pressnail B, Bilbao J, Aviv RI, et al. Brain metastasis from an unknown primary, or primary brain tumour? A diagnostic dilemma. CURRENT ONCOLOGY. 2009;16(1):5.

86. Sergey K. Filippov OS, Anna Bogomolova, Miroslav Vetrik, Daniel Jirak, Jan Kovar, Jan Kucka, Sara Bals, Stuart Turner, Petr Stepanek, Martin Hruby. Glycogen as Biodegradable Construction Nanomaterial for in vivo Use. 2012.

87. Healy ME, Hesselink JR, Press GA, Middleton MS. Increased detection of intracranial metastases with intravenous Gd-DTPA. Radiology. 1987 Dec;165(3):619-24. PubMed PMID: 3317496.

88. Thorsen F, Fite B, Mahakian LM, Seo JW, Qin S, Harrison V, et al. Multimodal imaging enables early detection and characterization of changes in tumor permeability of brain metastases. Journal of controlled release : official journal of the Controlled Release Society. 2013 Oct 29;172(3):812-22. PubMed PMID: 24161382.

89. Rana SVS. Biotechniques: Theory and Practice. Shivaji Road, Meerut-250 002, India: Rakesh K. Rastogi, Rastogi Publications; 2006.

90. Rima W, Sancey L, Aloy MT, Armandy E, Alcantara GB, Epicier T, et al. Internalization pathways into cancer cells of gadolinium-based radiosensitizing nanoparticles. Biomaterials. 2013 Jan;34(1):181-95. PubMed PMID: 23046756.

91. Xu P, Gullotti E, Tong L, Highley CB, Hasan DRET, Cheng J-X, et al. Intracellular Drug Delivery by Poly(lactic-co-glycolic acid) Nanoparticles, Revisited. Molecular Pharmaceutics. 2008 November 11, 2008;6(1):190-201. Epub November 11, 2008.

92. Swanson JA, Watts C. Macropinocytosis. Trends in cell biology. 1995 Nov;5(11):424-8. PubMed PMID: 14732047.

93. Kelf TA, Sreenivasan VK, Sun J, Kim EJ, Goldys EM, Zvyagin AV. Non-specific cellular uptake of surface-functionalized quantum dots. Nanotechnology. 2010 Jul 16;21(28):285105. PubMed PMID: 20585157.

94. Naahidi S, Jafari M, Edalat F, Raymond K, Khademhosseini A, Chen P. Biocompatibility of engineered nanoparticles for drug delivery. Journal of controlled release : official journal of the Controlled Release Society. 2013 Mar 10;166(2):182-94. PubMed PMID: 23262199.

95. Zhang S, Li J, Lykotrafitis G, Bao G, Suresh S. Size-Dependent Endocytosis of Nanoparticles. Adv Mater. 2009;21:419-24. PubMed PMID: 19606281. Pubmed Central PMCID: 2709876.

96. Barua S, Rege K. Cancer-cell-phenotype-dependent differential intracellular trafficking of unconjugated quantum dots. Small. 2009 Mar;5(3):370-6. PubMed PMID: 19089841.

97. Meng H, Yang S, Li Z, Xia T, Chen J, Ji Z, et al. Aspect ratio determines the quantity of mesoporous silica nanoparticle uptake by a small GTPase-dependent macropinocytosis mechanism. ACS nano. 2011 Jun 28;5(6):4434-47. PubMed PMID: 21563770. Pubmed Central PMCID: 3125420.

98. Yoo HS, Park TG. Biodegradable polymeric micelles composed of doxorubicin conjugated PLGA-PEG block copolymer. Journal of controlled release : official journal of the Controlled Release Society. 2001 Jan 29;70(1-2):63-70. PubMed PMID: 11166408.

99. Glaumann H, Fredzell J, Jubner A, Ericsson JLE. Uptake and degradation of glycogen by kuppfer cells. Experimental and molecular pathology. 1979 December 19 1978;31:70-80.

100. Rejman J, Oberle V, Zuhorn IS, Hoekstra D. Size-dependent internalization of particles via the pathways of clathrin- and caveolae-mediated endocytosis. The Biochemical journal. 2004 Jan 1;377(Pt 1):159-69. PubMed PMID: 14505488. Pubmed Central PMCID: 1223843.

101. Katona I, Weis J, Hanisch F. Glycogenosome accumulation in the arrector pili muscle in Pompe disease. Orphanet journal of rare diseases. 2014;9(1):17. PubMed PMID: 24495340. Pubmed Central PMCID: 3922310.

102. Mathews, Holde v. Locations of major metabolic pathways within a eukaryotic cell. In: cell.gif, editor. Principles of Biochemistry: The Benjamin/Cummings Publishing Co Inc.

103. Bruce Alberts AJ, Julian Lewis, Keith Roberts, Peter Walter. Molecular Biology of the Cell. USA: Garland Science; 2008. 1550 p.

104. Weihua Z, Lin Q, Ramoth AJ, Fan D, Fidler IJ. Formation of solid tumors by a single multinucleated cancer cell. Cancer. 2011 Sep 1;117(17):4092-9. PubMed PMID: 21365635. Pubmed Central PMCID: 3136613.

105. Wilhelm C, Gazeau F, Roger J, Pons JN, Bacri J-C. Interaction of Anionic Superparamagnetic Nanoparticles with Cells: Kinetic Analyses of Membrane Adsorption and Subsequent Internalization. Langmuir. 2002 Received March 13, 2002. In Final Form: August 8, 2002;18:8148-55. Epub 8148.

106. Ambrozek-Latecka JZM, Kawiak J, Hoser DWG. Monitoring cell proliferation in vitro with different cellular fluorescent dyes. FOLIA HISTOCHEMICA ET CYTOBIOLOGICA. 2013;51(3):193-200.

107. Pampaloni F, Reynaud EG, Stelzer EH. The third dimension bridges the gap between cell culture and live tissue. Nature reviews Molecular cell biology. 2007 Oct;8(10):839-45. PubMed PMID: 17684528.

108. Bilgin CC, Kim S, Leung E, Chang H, Parvin B. Integrated profiling of three dimensional cell culture models and 3D microscopy. Bioinformatics. 2013 Dec 1;29(23):3087-93. PubMed PMID: 24045773. Pubmed Central PMCID: 3834800.

109. Sutherland R, Carlsson J, al. RDe. Spheroids in Cancer Research. Cancer research. 1981;41:2980-4.

110. Liu J, Wang L, Ma L, Xu J, Liu C, Zhang J, et al. Significantly increased expression of OCT4 and ABCG2 in spheroid body-forming cells of the human gastric cancer MKN-45 cell line. Oncology letters. 2013 Oct;6(4):891-6. PubMed PMID: 24137432. Pubmed Central PMCID: 3796425.

111. Frank L. Meyskens JSPT, Moon TE. Quantitation of the Number of Cells within Tumor Colonies in Semisolid Medium and Their Growth as Oblate Spheroids. Cancer research. 1984;44:271-7.

112. Hirschhaeuser F, Menne H, Dittfeld C, West J, Mueller-Klieser W, Kunz-Schughart LA. Multicellular tumor spheroids: an underestimated tool is catching up again. Journal of biotechnology. 2010 Jul 1;148(1):3-15. PubMed PMID: 20097238.

113. Paunesku T, Ke T, Dharmakumar R, Mascheri N, Wu A, Lai B, et al. Gadolinium-conjugated TiO2-DNA oligonucleotide nanoconjugates show prolonged intracellular retention period and T1-weighted contrast enhancement in magnetic resonance images. Nanomedicine : nanotechnology, biology, and medicine. 2008 Sep;4(3):201-7. PubMed PMID: 18567541. Pubmed Central PMCID: 2663023.

114. Cacheris WP, Quay SC, Rocklage SM. The relationship between thermodynamics and the tocicity of gadolinium complexes. Magnetic Resonance Imaging. 1990;8:467-81.

115. Haudenschild CC, Schwartz SM. Endothelial regeneration. II. Restitution of endothelial continuity. Laboratory investigation; a journal of technical methods and pathology. 1979 November;41(5):407-18. PubMed PMID: 502473.

116. Liang CC, Park AY, Guan JL. In vitro scratch assay: a convenient and inexpensive method for analysis of cell migration in vitro. Nature protocols. 2007;2(2):329-33. PubMed PMID: 17406593.

117. Nygaard V, Clancy LPKVT, Hovig E. Melanoma brain colonization involves the emergence of a brain-adaptive phenotype. Oncoscience. 2014;1(1):82-94. Epub January 10, 2014.

118. Wright PJ, Mougin OE, Totman JJ, Peters AM, Brookes MJ, Coxon R, et al. Water proton T1 measurements in brain tissue at 7, 3, and 1.5 T using IR-EPI, IR-TSE, and MPRAGE: results and optimization. Magma. 2008 Mar;21(1-2):121-30. PubMed PMID: 18259791.

119. Yuan Y, Wyatt C, Maccarini P, Stauffer P, Craciunescu O, Macfall J, et al. A heterogeneous human tissue mimicking phantom for RF heating and MRI thermal monitoring verification. Physics in medicine and biology. 2012 Apr 7;57(7):2021-37. PubMed PMID: 22430012. Pubmed Central PMCID: 3728669.

120. Christoffersson JO, Olsson LE, Sjoberg S. Nickel-doped agarose gel phantoms in MR imaging. Acta radiologica. 1991 Sep;32(5):426-31. PubMed PMID: 1911001.

121. Marianne Petrén-Mallmin AE, Wolfgang Rauschning, Anders Hemmingsson. The effect of temperature on MR relaxation times and signal intensities for human tissues. Magma. 1993 September 1993;1(3-4):176-84. Epub December 1993.

122. Tofts P. Quantitative MRI of the brain: Measuring changes caused by disease. Tofts P, editor. West Sussex, England: John Wiley & Sons Ltd; 2003 December 2004. 634 p.

123. Rooney WD, Johnson G, Li X, Cohen ER, Kim SG, Ugurbil K, et al. Magnetic field and tissue dependencies of human brain longitudinal 1H2O relaxation in vivo. Magnetic resonance in medicine : official journal of the Society of Magnetic Resonance in Medicine / Society of Magnetic Resonance in Medicine. 2007 Feb;57(2):308-18. PubMed PMID: 17260370.

124. Terreno E, Geninatti Crich S, Belfiore S, Biancone L, Cabella C, Esposito G, et al. Effect of the intracellular localization of a Gd-based imaging probe on the relaxation enhancement of water protons. Magnetic resonance in medicine : official journal of the Society of Magnetic Resonance in Medicine / Society of Magnetic Resonance in Medicine. 2006 Mar;55(3):491-7. PubMed PMID: 16450336.

125. Wendelboe IH. In vitro effects of nanoparticle contrast agents on cellular functions and relaxometry [Experimental cell biology]. Bergen: University of Bergen; 2009.

126. Kanwar RK, Chaudhary R, Tsuzuki T, Kanwar JR. Emerging engineered magnetic nanoparticulate probes for targeted MRI of atherosclerotic plaque macrophages. Nanomedicine (Lond). 2012 May;7(5):735-49. PubMed PMID: 22630154.

127. Cao CY, Shen YY, Wang JD, Li L, Liang GL. Controlled intracellular self-assembly of gadolinium nanoparticles as smart molecular MR contrast agents. Scientific reports. 2013;3:1024. PubMed PMID: 23289066. Pubmed Central PMCID: 3535584.

128. Felleskatalogen. Omniscan Felleskatalogen.no: Felleskatalogen; [updated July 2 2013]. Available from: http://www.felleskatalogen.no/medisin/omniscan-ge-healthcare-562413.

129. Greish K. Enhanced permeability and retention of macromolecular drugs in solid tumors: a royal gate for targeted anticancer nanomedicines. Journal of drug targeting. 2007 Aug-Sep;15(7-8):457-64. PubMed PMID: 17671892.

130. Nichols JW, Bae YH. EPR: Evidence and Fallacy. Journal of controlled release : official journal of the Controlled Release Society. 2014 Apr 29. PubMed PMID: 24794900.

131. Wang ZJ, Boddington S, Wendland M, Meier R, Corot C, Daldrup-Link H. MR imaging of ovarian tumors using folate-receptor-targeted contrast agents. Pediatric radiology. 2008 May;38(5):529-37. PubMed PMID: 18357444. Pubmed Central PMCID: 2745549.

132. Di Corato R, Gazeau F, Le Visage C, Fayol D, Levitz P, Lux F, et al. High-resolution cellular MRI: gadolinium and iron oxide nanoparticles for in-depth dual-cell imaging of engineered tissue constructs. ACS nano. 2013 Sep 24;7(9):7500-12. PubMed PMID: 23924160.